Conception and performance of IViST: A novel platform for real-time In Vivo Source Tracking in brachytherapy

Thèse

Haydee Maria Linares Rosales

Doctorat en physique
Philosophiæ doctor (Ph. D.)

Québec, Canada

Conception and performance of IViST: A novel platform for real-time In Vivo Source Tracking in brachytherapy

Thèse

Haydee Maria Linares Rosales

Sous la direction de:

Luc Beaulieu, directeur de recherche
Sam Beddar, codirecteur de recherche

Résumé

La curiethérapie à haut débit de dose (HDR pour High Dose Rate) est une modalité de traitement du cancer qui délivre au volume cible la dose prescrite avec un débit de dose élevé. Malgré les distributions de doses hautements conformes obtenues avec cette modalité de traitement, le traitement lui-même n'est pas exempt d'erreurs. En raison des forts gradients de dose, typique de la curiethérapie, de petites erreurs dans le positionnement de la source peuvent entraîner des conséquences néfastes pour les patients. L'utilisation systématique de systèmes de vérification en temps réel est le seul moyen de savoir quelles doses ont été réellement données à la tumeur et aux organes à risque. Cette thèse présente les démarches effectuées pour créer et valider un système de dosimétrie à scintillateurs plastiques multipoints (mPSD pour Multipoint Plastic Scintillation Detector) capable d'effectuer avec précision des mesures in vivo en curiethérapie HDR.

Un prototype a été optimisé, caractérisé et testé dans des conditions typiques de la curiethérapie HDR. Une analyse exhaustive a été réalisée pour obtenir un modèle optimisé du détecteur, capable de maximiser la collection de lumière de scintillation produite par l'interaction des photons ionisants. Il a été constaté que le scintillateur de longueur d'onde plus courte devrait toujours être placé plus près du photodétecteur, alors que le scintillateur émettant dans la longueur d'onde la plus élevée doit être en position distale. Si la configuration, comme mentionnée précédemment, n'est pas utilisée, des effets d'excitation et d'auto-absorption entre les scintillateurs peuvent se produire, et en conséquence, la transmission de la lumière à travers la fibre collectrice n'est pas optimale. Le détecteur a été rendu étanche à la lumière. Son noyau de 1 mm de diamètre permet son utilisation dans la majorité des applicateurs utilisés pour le parcours de la source en curiethérapie HDR avec l'^{192}Ir. Pour la meilleure configuration du détecteur multipoints (3 mm de BCF10, 6 mm de BCF12, 7 mm BCF60), une optimisation numérique a été effectuée pour sélectionner les composants optiques (miroir dichroïque, filtre et tube photomultiplicateur (PMT pour Photomultiplier Tube)) qui correspondent le mieux au profil d'émission recherché. Ceci permet la déconvolution du signal en utilisant une approche multispectrale, en extrayant la dose de chaque élément tout en tenant compte de l'effet de tige Cerenkov. Le système de luminescence optimisé a été installé dans une boîte protectrice pour assurer la stabilité des composantes optiques lors de la manipulation. Les performances dosimétriques du système IViST (In Vivo Source Tracking) ont été évaluées en curiethérapie

HDR, sur une plage clinique réaliste allant jusqu'à 10 cm de distance entre la source et les capteurs du mPSD. IViST peut simultanément mesurer la dose, trianguler la position et mesurer le temps d'arrêt de la source. En effectuant 100 000 mesures/s, IViST échantillonne suffisamment de données pour effectuer rapidement des tâches QA / QC clés, telles que l'identification d'un mauvais temps d'arrêt individuel ou des tubes de transfert interchangés. En utilisant 3 capteurs colinéaires et des informations planifiées pour une géométrie d'implant provenant des fichiers DICOM RT, la plateforme peut également trianguler la position de la source en temp réel avec une précision de positionnement de 1 mm jusqu'à 6 cm de la source. Le détecteur ne présentait aucune dépendance angulaire. Un essai clinique est actuellement en cours avec ce système.

Abstract

High Dose Rate (HDR) brachytherapy is a cancer treatment modality that delivers to the target volume high doses in short amount of time in a few fractions. Despite the highly conformal dose distributions achieved with this treatment modality, the treatment itself is not free from errors. Because of the high dose gradient characteristics of the brachytherapy techniques, small errors in the source positioning can result in harmful consequences for patients. The routine use of a real-time verification system is the only way to know what dose was actually delivered to the tumor and organs at risk. This thesis presents the investigation done to obtain a Multi-point Plastic Scintillation Detector (mPSD) system capable of accurately performing in vivo dosimetry measurements in HDR brachytherapy.

A first system's prototype was optimized, characterized, and tested under typical HDR brachytherapy conditions. An exhaustive analysis was carried out to obtain an optimized mPSD design that maximizes the scintillation light collection produced by the interaction of ionizing photons. We found that the shorter wavelength scintillator should always be placed closer to the photodetector and the longer wavelength scintillator in the distal position for the best overall light-yield collection. If the latter configuration is not used, inter-scintillator excitation and self-absorption effects can occur, and as a consequence, the light transmission through the collecting fiber is not optimal. The detector was made light-tight to avoid environmental light, and its 1 mm diameter core allows their usage in most applicator channel used in ^{192}Ir HDR brachytherapy. For the best mPSD design (3 mm of BCF10, 6 mm of BCF12, 7 mm BCF60), a numerical optimization was done to select the optical components (dichroic mirror, filter and Photomultiplier Tube (PMT)) that best match the light emission profile. It allows for signal deconvolution using a multispectral approach, extracting the dose to each element while taking into account the Cerenkov stem effect. The optimized luminescence system was enclosed into a custom-made box to preserve the optical chain stability and easy manipulation. The In Vivo Source Tracking (IViST) system's dosimetric performance has been evaluated in HDR brachytherapy, covering a range of 10 cm of source movement around the mPSD's sensors. IViST can simultaneously measure dose, triangulate source position, and measure dwell time. By making 100 000 measurements/s, IViST samples enough data to quickly perform key QA/QC tasks such as identifying wrong individual dwell time or interchanged transfer tubes. By using 3 co-linear sensors and planned information for an implant

geometry (from DICOM RT), the platform can also triangulate source position in real-time with 1 mm positional accuracy up to 6 cm from the source. The detector further exhibited no angular dependence. A clinical trial is presently on-going using the IViST system.

Contents

List of Tables

List of Figures

List of abbreviations

ANN	Artificial Neural Network
AUC	Area Under the Curve
BT	Brachytherapy
CPE	Charged Particle Equilibrium
DTW	Dynamic Time Warping
EBRT	External Beam Radiotherapy
GUI	Graphical User Interface
HDR	High Dose Rate
IMBT	Intensity Modulated Brachytherapy
IMRT	Intensity Modulated Radiation Therapy
ISD	Inorganic Scintillator Detector
IVD	In Vivo Dosimetry
IViST	In Vivo Source Tracking
LDR	Low Dose Rate
MC	Monte Carlo
ML	Machine Learning
MOSFET	Metal Oxide Semiconductor Field Effect Transistor

mPSD Multi-point Plastic Scintillation Detector

OAR Organ at risk

OSL Optically Stimulated Luminescence

PMMA Poly(methyl methacrylate)

PMT Photomultiplier Tube

PSD Plastic Scintillation Detector

QA Quality Assurance

ROC Receiver Operating Characteristic

SBR Signal to Background Ratio

SNR Signal to Noise Ratio

TLD Thermoluminescent Dosimeter

TPS Treatment Planning System

VMAT Volumetric Modulated Arc Therapy

To my mom and family
To the memory of aunt Mercedes

Acknowledgments

During my childhood, people used to ask me: *What do you want to be when you grow up?* Back in those days, I was innocent enough to reply: *I want to be a scientist, one of those who invent things and help people.* Perhaps it might sound naive but the fundamental truth until today is that I have always wanted to do science for people's benefit. Being part of a doctoral program gave me the opportunity that I always wanted. However, being recognized as a doctor of science entails great professional and personal challenges, challenges that never scared me in the past, and that I will continue to face while pursuing my dreams. When I look back and think, I can visualize five years of hard work passing by in a couple of minutes. I also see people around me without whom I could not have overcome each of those challenges. I would like to take this opportunity to thank in a very brief manner the support of every person, friend, co-worker and family, without whom I could not have found the scintillating light at the end of the tunnel.

Luc, thank you very much for the huge opportunity you gave me. I feel extremely honoured to have been part of your group. Thanks for being such a great supervisor. I had high expectations for a Ph.D. and most of them were met thanks to you. Thanks for giving me the freedom to do research while having you as a real backup. Most importantly, thanks for opening the doors of your house and family. I also have special gratitude for Professor Louis Archambault. In Louis, I always found wise advice, constructive criticism and a different point of view. Louis, I am infinitely thankful for all the time that you kindly spent in support of my project. Furthermore, I want to acknowledge the support of my co-supervisor Sam Beddar. Thank you, Sam, for always pushing me to improve the quality of communication skills in science.

When I left my home five years ago, I did it with the desire to integrate myself into a new society and learn as much as I could. I think I succeeded, but not only because of my strong will. I succeeded thanks to the welcoming people I found in my path. Thank you to all the physicists from CHU de Québec for letting me be part of your trainees. Special thanks for Sylviane, Audrey and Nicolas. Thanks also to the GRPM students I met during this period. Along this journey, I had the opportunity to meet people with whom I enjoyed every single conversation. Thank you, Andrea, Daniel Maneval, Daline, Emily C., Angélika, Charles

Joachim and François. I also found good friendship in Madison and Nadia. Thank you both for all the time we spent together.

I further want to acknowledge the support of my new Cuban family. Without them, all these years would not have been the same. In Québec city, I found a new home. This new home is particularly cold most of the time. However, with my Cuban friends, I can feel warm again. With those people, I can feel the warm temperatures that I missed those days of August 2015, where no one but me was wearing a jacket. Thanks Eileen, Estalin, Lester, Ania, Los Bocourts, Los Yaris, Los Anet. *Muchas gracias a todos.* Thanks also to my exceptional friend Maria de Jesus, who has always been there for me.

Mom, if you ask me to write this thesis again, I can easily do it even with my eyes closed. However, it is difficult to write how much I love you and appreciate all you have done for me. The person I am today is because of you. I also want to thank all my family members from the deepest place of my heart. This Ph.D. is dedicated to you, and all the beloved people we lost in these past five years. Dad, Saykel and aunt Mercedes, I'm sure wherever you are now, you feel proud and happy. Ale, my soulmate, thanks for all you do every day for me. None of this would be the same without you.

Ultimately, I allow myself to finish these acknowledgements with a phrase by Isaac Newton that has always inspired me: *"... If I have seen further, it is by standing on the shoulders of Giants"*. Thanks to all of you for being there and thank you God for being by my side.

Haydee M. Linares Rosales

Avant-propos

The thesis presented includes six scientific articles published or submitted to scientific journals with peer review processes. This foreword provides information about each of the publications: the status of the publication, the changes between the version integrated into the thesis and the published version, as well as the role of each author.

Chapter 2 : Optimization of a multipoint plastic scintillator dosimeter for high dose rate brachytherapy

Haydee M. Linares Rosales[1,2], Patricia Duguay-Drouin[1,2], Louis Archambault[1,2], Sam Beddar[3], Luc Beaulieu[1,2]

[1] *Département de physique, de génie physique et d'optique et Centre de recherche sur le cancer, Université Laval, Québec, Canada.*

[2] *Département de radio-oncologie et Axe Oncologie du CRCHU de Québec, CHU de Québec - Université Laval, QC, Canada.*

[3] *Department of Radiation Physics, The University of Texas MD Anderson Cancer Center, Houston, TX 77003, United States.*

Publication status : The article was published in the journal Medical Physics (Volume 46, Number 5) on May 2019. No changes were made to the content of the article when it was inserted into the thesis.

Contribution : My author status in the article is primary. I established the research plan and the measurement protocol and carried out all the measurements. I analyzed all the collected results and wrote the entire article. The other co-authors reviewed the plans, participated in the analysis of the results, revised and edited the article.

Chapter 3 : Dosimetric performance of a multi-point plastic scintillator dosimeter as a tool for real-time source tracking in high dose rate ^{192}Ir brachytherapy

Haydee M. Linares Rosales[1,2], Louis Archambault[1,2], Sam Beddar[3,4], Luc Beaulieu[1,2]

[1]*Département de physique, de génie physique et d'optique et Centre de recherche sur le cancer, Université Laval, Québec, Canada.*
[2]*Département de radio-oncologie et Axe Oncologie du CRCHU de Québec, CHU de Québec - Université Laval, QC, Canada.*
[3]*Department of Radiation Physics, The University of Texas MD Anderson Cancer Center, Houston, TX 77003, United States.*

Publication status : The article was published in the journal Medical Physics on May 2020 (pre-print version available). No changes were made to the content of the article when it was inserted into the thesis.

Contribution : My author status in the article is primary. I established the research plan and the measurement protocol and carried out all the measurements. I analyzed all the collected results and wrote the entire article. The other co-authors reviewed the plans, participated in the analysis of the results, revised and edited the article.

Chapter 4 : 3D source tracking and error detection in HDR using independent scintillator dosimetry systems

Haydee M. Linares Rosales[1,2], Jacob Graversen Johansen[3], Gustavo Kertzscher[3], Kari Tanderup [3], Luc Beaulieu[1,2], Sam Beddar[4].

[1]*Département de physique, de génie physique et d'optique et Centre de recherche sur le cancer, Université Laval, Québec, Canada.*

[2]*Département de radio-oncologie et Axe Oncologie du CRCHU de Québec, CHU de Québec - Université Laval, QC, Canada.*

[3]*Aarhus University Hospital, Department of oncology, Aarhus C, Denmark.*

[4]*Department of Radiation Physics, The University of Texas MD Anderson Cancer Center, Houston, TX 77003, United States.*

Publication status : The article was submitted for publication in the journal Medical Physics on June 2020. No changes were made to the content of the article when it was inserted into the thesis.

Contribution : My author status in the article is primary. I established the research plan and the measurement protocol and carried out all the measurements. I analyzed all the collected results and wrote the entire article. The other co-authors reviewed the plans, participated in

the analysis of the results, revised and edited the article.

Chapter 5 : On the use of machine learning methods for mPSD calibration in HDR brachytherapy

Haydee M. Linares Rosales[1,2], Gabriel Couture[1,2], Louis Archambault[1,2], Sam Beddar[3,4], Luc Beaulieu[1,2]

[1] *Département de physique, de génie physique et d'optique et Centre de recherche sur le cancer, Université Laval, Québec, Canada.*

[2] *Département de radio-oncologie et Axe Oncologie du CRCHU de Québec, CHU de Québec - Université Laval, QC, Canada.*

[3] *Department of Radiation Physics, The University of Texas MD Anderson Cancer Center, Houston,TX, United States.*

[4] *The University of Texas MD Anderson UTHealth Graduate School of Biomedical Sciences, Houston, TX, United States.*

Publication status : The article was submitted for publication in the journal Medical Physics on April 2020. No changes were made to the content of the article when it was inserted into the thesis.

Contribution : My author status in the article is primary. I established the research plan and the measurement protocol and carried out all the measurements. I analyzed all the collected results and wrote the entire article. The other co-authors reviewed the plans, participated in the analysis of the results, revised and edited the article.

Chapter 6 : From conception to clinical trial: IViST - the first multi-sensor-based platform for real-time In Vivo dosimetry and Source Tracking in HDR brachytherapy

Haydee M. Linares Rosales[1,2], Audrey Cantin[2], Sylviane Aubin[2], Sam Beddar[3,4], Luc Beaulieu[1,2]

[1] *Département de physique, de génie physique et d'optique et Centre de recherche sur le cancer, Université Laval, Québec, Canada.*

[2] *Département de radio-oncologie et Axe Oncologie du CRCHU de Québec, CHU de Québec - Université Laval, QC, Canada.*

[3] *Department of Radiation Physics, The University of Texas MD Anderson Cancer Center, Houston,TX, United States.*

[4] *The University of Texas MD Anderson UTHealth Graduate School of Biomedical Sciences, Houston, TX, United States.*

Publication status : The article was submitted for publication in the journal Physica Medica on June 2020. No changes were made to the content of the article when it was inserted into the thesis.

Contribution : My author status in the article is primary. I established the research plan and the measurement protocol and carried out all the measurements. I analyzed all the collected results and wrote the entire article. The other co-authors reviewed the plans, participated in the analysis of the results, revised and edited the article.

Annexe A : Monte Carlo dosimetric characterization of a new high dose rate ^{169}Yb brachytherapy source and experimental validation using a multipoint plastic scintillator detector

Gabriel Famulari[1], Haydee M. Linares Rosales[2,3], Justine Dupere[4], David C. Medich[4], Luc Beaulieu[2,3], Shirin A. Enger[1,5,6]

[1] *Medical Physics Unit, McGill University, Montreal, QC, Canada.*

[2] *Département de physique, de génie physique et d'optique et Centre de recherche sur le cancer, Université Laval, QC, Canada.*

[3] *Département de radio-oncologie et Axe Oncologie du CRCHU de Québec, CHU de Québec-Université Laval, QC, Canada.*

[4] *Department of Physics, Worcester Polytechnic Institute, Worcester, MA, United States.*

[5] *Department of Oncology, McGill University, Montreal, QC, Canada.*

[6] *Research Institute of the McGill University Health Centre, Montreal, QC, Canada.*

Publication status : The article was accepted for publication in the journal Medical Physics on May 2020. No changes were made to the content of the article when it was inserted into the thesis.

Contribution : Gabriel Famulari and I contributed equally to this work. My author status in the article is primary. We both established the research plan carried out all the measurements. Gabriel Famulari performed the Monte Carlo simulations and I defined the measurement protocol and analyzed the collected results. Gabriel Famulari and I wrote the entire article. The other co-authors reviewed the plans, participated in the analysis of the results, revised and edited the article.

Introduction

The treatment of cancer continues to rest largely on three major modalities: surgery, radiotherapy and systemic therapies, including chemotherapy. Radiotherapy is currently an essential component in the management of cancer patients, either alone or in combination with surgery or chemotherapy, both for cure and for palliation [1]. The main goal of this treatment modality is the delivery of high radiation doses into the tumour region, causing the least possible damage in the surrounding areas composed by healthy tissues. Thus, a high level of precision and accuracy is mandatory when dealing with this kind of cancer treatments, especially in those regions located near radiosensitive organs or tissues (such as the testes, ovaries, intestines). Techniques like Intensity Modulated Radiation Therapy (IMRT) or Volumetric Modulated Arc Therapy (VMAT) produce highly conformal dose distributions and are non-invasive [2,3]. However, those techniques are susceptible to patient localization and setup errors because of the high dose gradients at the periphery of the target volume [3,4]. Brachytherapy takes advantage of the fact that the sources are connected directly/near to the target volume and they move with the target when the target itself is moving: there is a minimal in-patient variation during treatment [5].

In brachytherapy, radioactive sources are placed at a short distance from the target. The target receives a sufficiently high dose while the inverse square law ensures that even in the proximity, the dose to the surrounding healthy tissue (i.e., the organ at risk) is reduced considerably [5]. High dose gradients fields (20% or more per millimeter for the first few centimeters from the source) are characteristics of brachytherapy. Because of the aforementioned, brachytherapy allows for the delivery of a large dose of radiation in a reduced number of treatment visits (fraction). For example, in a typical HDR prostate treatment, a single fraction of 15 Gy is delivered in a few minutes to complement External Beam Radiotherapy (EBRT).

Despite the short distances involved in brachytherapy, the technique itself is not error-free, which can be caused by humans (e.g., incorrect medical indication, source strength input, patient identification, catheter length measurements, or applicator reconstruction) or by failures in the treatment system (e.g., mechanical events) [5]. Even small errors in the source positioning can result in harmful consequences for patients [6]. Systematic implementation of precise quality control and quality assurance protocols help to improve treatment quality, and

routine use of real-time verification systems and In Vivo Dosimetry IVD is the only way to know what dose was actually delivered to the tumour and organs at risk [7]. In some jurisdiction (e.g., France, the Netherlands), IVD has become mandatory either once or during each fraction. The clinical implementation of IVD requires a robust dosimetry system, i.e small detectors with high SNR, minimally intrusive to the patient, fast and reliable, which provides real-time dose readout [8]. A review by Tanderup *et al.* [7] highlighted the main aspects of various detectors that could be used as in vivo dosimeters in brachytherapy. On the other hand several works have focused on the source-tracking capacity of different detectors in HDR brachytherapy [9–14]. Some studies used an array of dosimeters placed on the patient's skin, and others a flat-panel detector. The use of Plastic Scintillation Detector (PSD), has several advantages that have been recently highlighted in the literature, a key one being their real-time response [15–30]. The combination of multiple scintillation sensors (*i.e.* single optical fiber mPSD) would allow simultaneous determination of the absorbed dose, dwell time and source position at different locations in a volume, thereby improving treatment quality [30–33]. Although PSDs are affected by the stem effect and temperature variations [26, 34], several investigations have developed methods to correct both of these dependencies in the detector response [16, 17, 20, 27, 32, 35–37].

Besides the aforementioned, brachytherapy clinics do not generally verify the delivered treatment's doses in real-time. The available real-time systems present small signal-to-noise ratios, limited time resolution, large measurements uncertainties and can detect only errors in the order of 20% or more [38]. The current thesis presents the development and performance evaluation of a novel multi-sensor-based dosimetry platform for plan monitoring that for the first time would be able to measure dose, source position, and dwell-time in real-time during brachytherapy treatments.

The first chapter presents a concise and focused literature review and theoretical notions on the two major themes of the thesis: IVD in brachytherapy and plastic scintillators detectors. Chapter 1 also presents the research project main goals and the subject of each of the subsequent chapters. Chapter 2 presents the experimental study carried out to obtain an optimal mPSD configuration, to determine the proper configuration of the scintillation light detection system and to evaluate the performance in terms of sensitivity and accuracy of the entire system in HDR brachytherapy. Chapter 3 presents the dosimetric performance of the optimized and characterized mPSD system in the context of IVD for HDR brachytherapy. Key parameters like the angular response of the dosimeter, the relative contribution of positioning and measurement uncertainties to the total uncertainty chain, the capacity of the system to measure individual dwell times and to track the source position in real-time were subject of Chapter 3. Chapter 4 presents a method to perform 3D source position reconstruction by combining IVD measurements from two independent detector systems. Using an mPSD system in combination with an inorganic scintillator detector system, we established a

methodology that allows for absolute source position reporting in 3D space, as well as needle shift corrections, source positioning tracking and source positioning error detection in real-time. Chapter number 5, presents the feasibility of using machine learning ML algorithms for mPSD calibration in HDR brachytherapy. The performance of the different algorithms was evaluated using different sample sizes and distances to the source for the mPSD system calibration. Finally, chapter 6 presents the platform named In Vivo Source Tracking IViST , a novel multi-sensor-based dosimetry platform developed in the context of this Ph.D. project, that allows for real-time plan monitoring in HDR brachytherapy.

Chapter 1

Theoretical basis and Ph.D. project

1.1 Errors in HDR bachytherapy and the need for in vivo dosimetry

HDR brachytherapy treatments are characterized by high dose gradients fields, few fractions, highly conformal dose distributions, with steep dose gradients often in close proximity to Organ at risk (OAR)s [38]. Errors during brachytherapy result in discrepancies between the planned and delivered treatments. The errors may occur when source positions and/or dwell times deviate from those in the treatment plan and result in erroneous dose rate distributions in the target and OARs. The treatment's associated errors have different origins, which could be human errors or malfunctioning of the equipment (*i.e.* mechanical errors). Examples of human errors include incorrectly specified source strength, erroneously connected source transfer guide tubes and gross applicator reconstruction errors. The mechanical events are related to the HDR control unit, the computer, the source cable, the catheter, and the applicators. Errors have been reported in dwell time programming by programming the source steps incorrectly. Additionally, defective afterloader stepping motor, flaws in the control software, sources remaining in the safe, in the patient, or along the transfer tubes were also reported. Existing channels of information regarding errors during radiotherapy include dedicated databases and published reports [39–43]. However, since radiotherapy clinics are not necessarily subject to policies that require public reporting in case of detected treatment errors, it is likely that a substantial portion of occurred incidences are left unknown to the radiotherapy community. Brachytherapy escapes the purview of record and verify systems as they are not usually integrated with EBRT existing systems, hence it is possible that errors remain unnoticed during the entire multifraction treatment course [44], or if detected they are typically only identified post-treatment.

Strict Quality Assurance (QA) programs have to be ensured by the radiation oncologists, medical physicists, and technical staff in general to avoid the occurrence of errors during the

treatment delivery [45]. In vivo dosimetry is the most direct measurement of the delivered dose in brachytherapy treatments. The initial/historical motivation for IVD in brachytherapy was to asses dose to organs at risk OAR by direct measurements, specially in situations where 3D image based brachytherapy may fail. Such cases include low-energy photon-emitting sources, regions close to the skin (breast brachytherapy) and in heterogeneous media, leading to significant dose calculation uncertainties [5, 7]. Even in regions where the TG-43 U1 [46] dose calculations are sufficiently accurate, there may be discrepancies between image-based calculated and delivered doses because the anatomy and position of applicators can change between imaging and dose delivery times [5]. At the same time, the inverse square dependence of the dose rate dictates strong dose gradients, that is, 20% or more per millimeter for the first few centimeters from the source. As such, a positioning error of 1–2 mm could lead to an in vivo measurement with deviations beyond the expected range solely based on a positioning error, due to an insufficiently accurate estimation of the sensor-to-source distance or to an actual displacement occurring between the detector placement and the treatment delivery. An exact knowledge of the source-to-dosimeter distance has to be ensured, in order to certainly attribute the differences measured to a treatment error and not only to a bad estimation of this parameter [38]. However, measuring a magnitude different than the expected, does not necessarily mean there is an error in the treatment delivery. For a clinical condition in which the detector position is ensured and free from errors, while the distance to the source increases, the measurement uncertainty increases as well, and becomes the main contributor to the uncertainty budget [8]. Thus minimal detectable deviations has to be set based on a prior characterization of the measurement tool. The use of a single action threshold value does not accurately represent the breadth of configurations that have to be measured by a dosimeter during a full treatment delivery [7]. The adoption of the statistical discrepancy criterion, with a prior knowledge of the plan, all known uncertainties are taken into account and applied as the delivery proceeds in combination with time-resolved IVD could improve the sensitivity and specificity of the measurement tool, and reduce the false alarms ratios [38, 44, 47].

1.2 Radiation detectors for in vivo dosimetry

Despite several studies [10,14,48–53] focusing on developing methods for real-time monitoring, there is limited availability of commercial systems that allow the implementation of such a technique. IVD in brachytherapy typically seek to combine the attributes of dosimetric precision, high spatial resolution, and easy/fast interpretation of results, with more pragmatic goals such as real-time output and ease of integration into workflow [5, 7, 38, 54, 55]. Table 1.1 shows the main characteristics of different detectors that have been used for brachytherapy-IVD purposes [7, 55]. The use of each detector in table 1.1 is rated as advantageous (++ symbol), good (+ symbol) or inconvenient (− symbol) based on its intrinsic properties and

performance.

Table 1.1 – Characteristics of detectors and dosimetry systems of importance for precise routine IVD in brachytherapy. Items are rated according to: advantageous (++), good (+), and inconvenient (−) [7, 55, 56].

	TLD	Diode	MOSFET	OSL/RL	PSD
Material	LiF	Si	Si/SiO_2	Al_2O_3:C	PS/PVT
Density (g/cm^3)	2.64	2.33	2.33/2.65	3.95	1.06/1.03
Size	+	+/−	+/++	++	++
Sensitivity	+	++	+	++	+/++
Energy dependence	+	−	−	−	++
Angular dependence	++	−	+	++	++
Dynamic Range	++	++	+	++	++
Use*	+	++	++	−/+	+/++
Commercial Availability	++	++	++	−	+
Online dosimetry	−	++	+	++	++

Use: This field includes the tasks related to calibration procedures, QA, stability, robustness, system's size and easy of operation.*

***PS**: Polystyrene, **PVT**: Polyvinyltoluene*

The **Thermoluminescent Dosimeter (TLD)** is a widely used detector in HDR ^{192}Ir brachytherapy [7,57–61]. Its usage is attractive since no cables are needed, and is a well-studied system. This kind of detectors can be easily shaped and therefore inserted into catheters and regions of interest [59, 60]. For TLDs material, one of the most used is the lithium fluoride (LiF) in a rod shape. TLDs requires special preparation (annealing, individual calibration, careful handling, fading correction) and do not provide a direct reading during the treatment. Because of this limitations, those detectors are considered as a second choice compared to other dosimetry systems capable of providing reading in real-time [7].

The use of **diodes** detectors is well-known in EBRT, and less often used for in vivo brachytherapy. Diodes provide an immediate readout, high sensitivity and reasonably small size. The available commercial systems have a reasonable price. Unfortunately, they are also known for undesirable dosimetric characteristics, including directional, energy and temperature dependencies, as well as changes in their sensitivity due to radiation damage [7, 55]. The study performed by Seymour et al. [51] using diodes for a rectum case reported a mean difference between the calculated and measured dose of 11% ranging from -31 to +90 %, while the study in bladder reported a mean difference of 4 %, with variations between -27 to +26 %. Although the study done by Seymour et al. [51] evidenced the diode capacity to measure doses and detect positioning errors in real-time, the results were subjected to the inherent detector angular and dose rate dependencies.

Metal Oxide Semiconductor Field Effect Transistor (MOSFET)s dosimeters are commercially available detectors. Notably, in HDR brachytherapy MOSFETs have been widely

used and characterized [57, 62–65], because of the advantages they provide for IVD purposes. The detectors' small size allows their insertion into catheters and the arrangement into an array (multiple MOSFET sensors). MOSFETs provide real-time measurements [7]. Like in diodes, their composition (Z_{eff}) makes them highly dependent on radiation quality. Additionally, they have a rather limited lifetime. The detector suffers degradation from radiation exposure [7, 66]. Lambert et al. [57] reported a MOSFET response dependence with the dose rate and source distance. Besides, this detector suffers from angular dependencies [67, 68]. A variation of 10% per angle of incidence should be expected in the detector's response. This effect is attributed to the design of the detector and its epoxy covering, which is no uniform [57]. However, the MOSFET readings were shown to be stable within the experimental uncertainty over the entire temperature range tested by Lambert et al. [57].

Optically Stimulated Luminescence (OSL) dosimeters present advantages over TLDs, justifying their actual replacement as a personal dosimeter in the industry and public health framework. OSL detectors provide instantaneous reading (online stimulation), faster processing, and the ability to store their reading without much degradation of the optical signal (a permanent record) [7, 54]. Additionally, carbon-doped aluminum oxide (Al_2O_3:C) crystal (radioluminescent crystal) can be also used to operate in a radioluminescence, RL, mode. RL detectors are online detectors. The response of OSL detectors is independent of energy for MeV photons beams, electrons and protons [54] and dose rate independent for a source of ^{192}Ir [69]. Andersen et al. [47] studied a detector prototype composed of Al_2O_3:C crystal coupled with the optical fiber [7, 47]. The system proposed in [47] can perform automatic online IVD directly into the tumour region by using small detector probes that fit into applicators such as standard needless or catheters, being linear to the dose rate and had a reproducibility of 1.3 %. Even though the sensitive detecting material of these detectors (Al_2O_3:C) is not water-equivalent, they have good potential for IVD in brachytherapy due to their ability to provide feedback in real-time [7].

Nevertheless, those dosimeters present some disadvantages compared to plastic scintillator dosimeters, mainly associated with the water equivalence. Different approaches have been explored to use PSD as an in vivo dosimeter in brachytherapy. Lambert et al. in 2006 [18] developed an in vivo system that was clinically tested in a patient's study [18, 25]. At that time, the authors did not report any temperature dependence for their in vivo measurement performed inside the urethra nor experiencing any stem effect when using these PSDs. However, the temperature dependence and their impact on the measurement accuracy depend on the type of PSD [26]. Later in 2007 [57], a comparison of a diamond detector, MOSFET, TLD, and PSD highlighted the benefit of using PSDs for measurements of doses up to 100 mm distance; a 3 % agreement with TG-43 U1 [70]. Also, the findings in [57] demonstrated that the scintillator dosimeter turned out to be the most accurate from the detectors tested and presented the most favourable characteristics for HDR brachytherapy. Therriault-Proulx

et al. [22, 23] developed and validated the use of PSDs during real-time measurements with ^{192}Ir HDR source. A clinically realistic ^{192}Ir HDR brachytherapy treatment plan was simulated in a customized water phantom that allowed the reproduction of the catheter position similar to a plan that was created in the clinical Treatment Planning System (TPS). The ratio of measured dose to planned dose was found below 1.2 in all cases, which is a significant deviation, especially at short distances from the source. The importance of removing stem effects for IVD using PSD in HDR brachytherapy treatments was assessed and found to be required for accurate dose measurements in this energy range. [25]. Taking into account the importance of PSDs for this Ph.D. project, the following section details this kind of detector's characteristics.

1.3 Plastic Scintillator Detectors

1.3.1 Luminescence

After the absorption of radiation, some materials retain part of the absorbed energy in metastable states. The subsequent release of energy in the ultraviolet, visible or infrared light range is called luminescence. Depending on the time delay between the stimulation and light emission, luminescence can be classified as *fluorescence*, *phosphorescence* and *delayed fluorescence*.

Fluorescence is the prompt emission of visible radiation following the medium excitation. It corresponds (for organic scintillators) to a radiative transition from S_1 level to S_0 level, following absorption, which occurs with a time delay of between 10^{-10} and 10^{-8} s. The intensity of the fluorescence emission decays exponentially with time t according to $I = I_0 exp(-t/\tau)$, being I_0 the intensity at $t = 0$, I the intensity at time t, and τ is the fluorescence decay time [71–73]. Under suitable conditions, phosphorescence and delayed fluorescence can be observed. Phosphorescence was initially called slow fluorescence and is associated with emission at a longer wavelength than fluorescence, but with a characteristic time that is generally much slower ($\sim 10^{-4}$ s or longer). Delayed fluorescence results in the same emission spectrum as prompt fluorescence. It decays non-exponentially with a longer period (i.e. longer emission time following excitation). The difference between phosphorescence and delayed fluorescence is associated with the existence of a metastable level M bellow S_1. According to certain conditions, transitions to ground state S_0 may occur (β process) inducing phosphorescence, or if the molecule acquires over time thermal activation energy, it will return to upper state S_1 (α process) leading to delayed emission [72].

1.3.2 Basic properties and dosimetric characteristics

Plastic scintillators are light-emitting elements, while plastic scintillating fibers are light-emitting elements to which a cladding, usually Poly(methyl methacrylate) (PMMA) was added to improve the light propagation and the use of a different base material [74]. The cladding allows for total internal reflection since the refractive index of the core is chosen to be larger than the index of the cladding. The cladding is also useful to protect the core from abrasion or accumulation of foreign material that would compromise the efficiency of the light pipe effect. Furthermore, the optical fiber is surrounded by a jacket to shield light and to protect the fiber from ambient contaminants. Plastic scintillators are composed of 97% of polyvinyltoluene (polystyrene in the case of plastic scintillating fibers) to which an organic fluor (remaining 3 %), the scintillating materials, is added. These fluors are composed of aromatic chain with strong carbon double bonds. This is called a two component systems [25]. To obtain emission of the green or orange light, a third component called a wavelength shifter is added. Table 1.2 details some of the characteristics of polyvinyltoluene, polystyrene and water. As could be observed in table 1.2 there is a high similarity between the properties of polyvinyltoluene, polystyrene and water, being the reason why PSD are considered water-equivalent materials.

Plastic scintillators composed mainly of hydrocarbon molecules have interaction properties similar to those of water, and human tissues, especially in the Compton dominated energy range of the standard photon beams used in radiation therapy [75]. The parameters that govern Compton scattering, such as mass energy absorption coefficients, and those that govern the resulting secondary charged particles, such as mass-collision stopping powers and mass angular scattering powers, are the primary considerations with respect to the water equivalence of a material. Above 100 keV of energy, proper matching of the mass-energy absorption coefficient, mass-collision stopping powers and mass angular scattering powers, for the materials in table 1.2 has been evidenced [16,25,74]. In addition to the materials used, the density of the detector constituents also play an important role in radiation interactions. This is referred to as the polarization or density effect, which is negligible for PSD because the wall and the detector volume have the same density and have a similar atomic structure [74, 76]. Thus, polarization will be homogeneous and the radiation field unperturbed, preserving water equivalence.

Table 1.2 – Physical Properties of the Polyvinyltoluene, Polystyrene, and Water [56].

Parameter	**Polyvinyltoluene**	**Polystyrene**	**Water**
Density (g/cm^3)	1.03	1.06	1.000
Ratio of the number of e^- in the compound to the molecular weight $< Z/A >$	0.5414	0.5377	0.5551
Electron density ($10^{23}e^-/g$)	3.272	3.238	3.433
Composition (weight %)	H: 8.47 C: 92.26	C: 91.53 H: 11.19	H: 7.74 O: 88.81

Energy independence of PSD was initially studied and validated by Beddar et al. in 1992 [16, 17], applying the Burlin cavity theory for two limiting cases: (1) zero wall thickness (i.e., no polystyrene wall) and (2) a wall sufficiently thick to provide Charged Particle Equilibrium (CPE). The wall thickness likely to be used in practice is on the order of 2 mm or less, much smaller than needed for establishing CPE. Therefore, the energy dependence for a typical PSD should adhere closely to that of the zero wall thickness scenario. In addition, the light emitted by plastic scintillators is directly proportional to the energy deposited by electrons with energies higher than approximately 125 keV. Thus, plastic scintillators are energy independent at the energies found in clinical electron and photon beams [77]. In the case of heavy charged particles, such as protons, the threshold energy for a linear response is much higher [16,17,75]. The energy independence in electrons and photons allows for instance, the use of a PSD in an MV range, that was pre-calibrated in known conditions at different beam quality (e.g. under ^{60}Co irradiations). The PSD causes small perturbations over the radiation fluence relative to the reference medium. Since the PSDs are water-equivalent and energy independent detectors, they should accurately measure dose for different quality photon beams and different energy electron beams without correction factors.

In EBRT, PSDs have a linear response with the dose and dose rate under photons and electrons irradiations. Some fluctuations in their response could be observed as a result of radiation damage. Exposure of a PSD to ionizing radiation can result in (1) damage to the detector or associated optical conduits that result in transmission loss and (2) damage to the scintillating molecules embedded in the bulk material rendering them temporarily or permanently incapable of producing light via scintillation. As a consequence, a reduction in scintillation efficiency and a darkening of the plastic scintillator and optical fibers is observed. Compared with other solid-state detectors like diodes or MOSFET, PSDs are relatively resistant [16, 75]. Previous studies [16, 78–80] demonstrated that the exact radiation damage characteristics depend on the design of the PSD, in particular, the materials used to construct it and the usage pattern. The implementation of IVD in brachytherapy demands for a reproducible dosimeter. Thus, as long as the PSD suffer no damages in their pathway through the catheter (no bending losses in the optical fiber, the scintillator coupling to the optical fiber is intact, etc.) and the light

detection system kept its stability, the detector's response is reproducible enough to meet the IVD requirements.

PSD possesses a high spatial resolution, which is superior to a PinPoint ionization chamber. This spatial resolution enables accurate dose measurements in regions characterized by high dose gradients. The angular dependence of a scintillation detector is determined by its physical construction. The major contributor is the ratio of the scintillator length to the diameter. The study performed by Archambault et al. [81] found no angular dependence on the plastic scintillator response when irradiated under EBRT, reporting a maximum deviation of 0.6 %. In case of brachytherapy modality, Lambert et al. [18] found that for diameter ratios bellow 5:1 (5 mm long, 1mm diameter) the angular dependence can be kept below ± 1.5 %. PSD presents highly stable measurements in short-term periods. Variations in the response are often largely attributable to photodetector noise [82] as well as stochastic variations in the number of photons produced by the scintillator for a given dose [74].

Temperature dependence of PSD is a factor that, for years, was considered negligible. In 2012 Beddar et *al.* [34] reported some temperature dependences observed during in vivo measurements, where variations of 0.6 %/°C relative to room temperature were observed for BCF60 scintillating fibers. An exhaustive analysis was done by Wooton et al. [26], demonstrating that the temperature dependence is conditioned to the type of scintillator. The temperature dependence of BCF60 PSDs is on the order of 1% within a few degrees of room temperature and on the order of 10% at human body temperature. The effect of temperature on BCF10 and BCF12 PSDs is much smaller [83], but would still contribute a systematic error in measured dose at non calibration temperatures if uncorrected. The findings in [84] associated the temperature effect to a basic (molecular) property of the material, being equivalent to thermal quenching. Clearly the effect of temperature must be accounted for in current PSDs and minimized in future PSDs if possible [26,84]. In 2015 Therriault-Proulx et al. [27] proposed a method allowing for temperature dependence correction requiring no prior knowledge of the temperature value. The proposed method is a spectral-based correction mechanism to adjust for temperature variations when using a PSD, based on the mathematical formalism proposed by [32], but separating the scintillation spectrum into two sub-components: one that depends on the influencing factor (temperature) and one that is independent of it (i.e. the reference spectrum). As a result, they found a good agreement for a ^{60}Co and MV photons beam.

1.3.3 Stem effect: Cerenkov light

As part of the light collected with a PSD, the stem effect is always present. It can have two origins. The first is the direct excitation of the polymer chain, or fluorescence, from the plastic optical fiber guides, and the second is the Cerenkov light production. Therriault-Proulx et al. [85] evaluated the nature of the stem effect light produced within an optical fiber, over the

clinical photon beam energy range. The fluorescence component produced in the optical fiber was found to be present over the entire range of clinically relevant irradiation energies. It is however orders of magnitude lower than that of Cerenkov light [75, 85].

Cerenkov light production inside PSD and their removal from the total signal, have been widely discussed. Cerenkov radiation occurs when a particle's velocity exceeds the speed of light in a given medium, being dependent on the fiber material, irradiation geometry [15, 19], and independent on temperature changes [26]. Cerenkov's intensity curve is directly proportional to $1/\lambda^3$. The intensity of Cerenkov light emitted in the optical guide is up to 2 orders of magnitude per mm lower than the intensity of the scintillation light produced by the scintillator. However, the length of the light guides within the radiation field is usually much longer than the scintillation probes-several centimeters versus a few millimeters at most for the scintillators [75]. Thus, Cerenkov signal can account for a large fraction of the light detected at the same time as the scintillation signal, a situation that is not desirable for accurate dosimetry.

The need for Cerenkov removal in brachytherapy is dependent on the type of brachytherapy source and the measurement geometry. Low Dose Rate (LDR) brachytherapy sources like ^{125}I or ^{103}Pd do not have energies high enough to produce Cerenkov radiation in a plastic optical fiber. In case of ^{192}Ir in HDR brachytherapy, the photon emission mean energy is 380 keV. For such radioisotope, Therriault-Proulx et al. [22, 23] showed that when the source is within 10 mm of the optical fiber and at distances larger than 25 mm from the scintillator, Cerenkov removal is necessary. Their in-water study demonstrated that an error in the order of 25% could be expected if stem signal removal is not performed. They also showed that in those conditions where the source is closer to the scintillator and farthest the optical fiber, the stem effect could be negligible [23]. The following paragraphs expose some of the techniques implemented to remove the Cerenkov signal from measurements.

Two-fiber subtraction was the first method introduced to allow for Cerenkov signal removal. This method was proposed by Beddar et al. [16, 17]. An experiment was performed in which a device made of two parallel adjacent optical fibers was irradiated, where only one optical fiber was coupled to a scintillator. Then, the total visible light produced is a superposition of two components, scintillation light and Cerenkov light. Having an optical fiber coupled to a scintillator, allowed quantifying the amount of Cerenkov produced by the clear optical guide, and its removal by subtraction from the total signal. This method is accurate in most situations, especially where large field irradiations ensure having the same particle fluence striking the fiber. In situations where steep dose gradient conditions are present, the method fails, leading to inaccuracies, because Cerenkov light can be generated with different intensities in the adjacent optical fibers.

Basic spectral filtering is an optical filtering proposed by de Boer et al. [35], where the fact of

the Cerenkov emission predominance near the blue-UV region was used as a removal technique. They implemented the scintillation light filtering employing a photodetector sensitive only to the scintillator's light emitted far from Cerenkov. This method resulted efficient in the removal of only 50 % of Cerenkov signal. Complete Cerenkov removal was unsuccessful since Cerenkov is emitted in all the visible light wavelength range [75].

The ***temporal filtering*** or *timing* method uses the principle of separating the optical signal detected, taking into account the decay time of the scintillator and Cerenkov. The method was proposed by Clift et al. [37] where a scintillator with a long decay was used on a single fiber. As the Cerenkov light production is correlated to the beam pulses and possesses decay time faster than the employed scintillator (264 ns), a signal separation was achieved because the Cerenkov stem signal decayed-out leaving only the scintillation signal. Clift et al. [37] demonstrated the ability to remove 99.9% of the stem effect while sacrificing 44% of the scintillation signal, resulting in a good alternative in dealing with Cerenkov light.

Chromatic removal technique considers the signal coming from the PSD as a function of the length of irradiated optical fiber, being a linear superposition of the scintillator and the Cerenkov light. The method was proposed by Fontbonne et al. [36]. They considered the difference in emitted light wavelength between Cerenkov and scintillator light, as well as the narrower range of emission wavelength for the scintillating fiber. The discrimination was performed using 2 optical filters that separate the signal into two wavelength bands, blue and green. According to Fontbonne et *al.*,

$$\begin{pmatrix} G_1 & B_1 \\ G_2 & B_2 \end{pmatrix} \times \begin{pmatrix} k_G \\ k_B \end{pmatrix} = \begin{pmatrix} D_1 \\ D_2 \end{pmatrix} \tag{1.1}$$

where G_X and B_X correspond to measurements in the green and blue wavelength regions, respectively k are calibration coefficients, D_X are the expected doses for measurement conditions $X = 1$ and $X = 2$, with the expectation that $D_1 = D_2$ [36, 74]. Once the calibration is done, the measured dose is determined: $D = k_G \cdot G + k_B \cdot B$, where G and B correspond to measurements in the green and blue wavelength regions. While blue and green spectral bands have been used in the early prototypes, the method is not limited to these two specific spectral bands. This approach eliminates the need for a second fiber or a complex timing circuit to achieve accurate dose measurements (output, depth dose curves, and profiles) of both photon and electron beams [36, 74, 75]. It also enables dose measurements in high-gradient regions such as the penumbra. A potential limitation of this approach is related to the calibration conditions chosen to extract the calibration coefficients k. In fact, as long as the two calibration conditions bound the measurement conditions, the technique is expected to achieve a high level of accuracy.

Air-core fibers are based on the principle that electrons do not produce Cerenkov light in

the air due to the refractive index near to 1. Light transmission through an air core, requires a highly reflective surface inside the air core. This can be achieved with a multilayered dielectric coating, a microstructured layer or a metal surface with a low attenuation coefficient [74]. Based on the previous explanation, Lambert et al. [20] developed a Cerenkov-free PSD by coupling a plastic scintillator to an air core light guide made from a hollow silica tube coated inside with a thin layer of silver. They showed that no Cerenkov or fluorescence was produced in the air core light guide, and the detector provided accurate depth dose measurements in external beam therapy. However, this method uses non-water equivalent materials that perturb the particle fluence and the delivered dose distribution. Additionally, these fibers are very rigid and also exhibit light attenuation properties that are up to 10 times higher than those of plastic core fibers, so only a few centimeters of air-core fibers can be used before they must be connected to regular optical guides. Because of the rigidity, their use for in vivo application tends to be avoided [75].

Multi hyperspectral filtering is a general technique applied to those cases where more signals need to be decoupled. The chromatic technique, even if efficient, is just applicable to two components signal. Based on that, Archambault et al. [32] proposed a generalized formalism that takes into account the signal produced by N sources, measured in L wavelength bands. Therriault-Proulx et al. [31] applied such a formalism to identify the signal coming from the mPSD, evidencing that the multi/hyperspectral method can extract scintillation signals in the presence of multiple stem effect contaminants (Cerenkov and fluorescence combined). Also, they showed that this method allows for multiple scintillators to be attached to a single light guide or multipoint PSDs (mPSDs), and disentangle the temperature dependence of scintillation light, allowing both temperature and dose measurements in vivo [31, 74].

1.4 Ph.D. Project

1.4.1 Scientific problem

The need for in vivo dosimetry in HDR brachytherapy has been evidenced in the literature. Despite the efforts made for the development and implementation of IVD in the clinical workflow [10, 14, 48–53, 86, 87], presently, brachytherapy clinics do not verify their treatments in real-time. The available commercial systems that provide real-time measurements have small signal-to-noise ratios, limited time resolution, large measurement uncertainties and can detect only large errors. On the other hand, the laboratory systems can be cumbersome to operate and did not go through regulatory approval. Furthermore, the constraints specific to this treatment modality, demand additional characteristics on the detector's side (dosimetric precision, high spatial resolution, real-time output), reducing the number of viable options. The benefits and limitations of PSDs in a single or multi-point configuration have been well docu-

mented [15–17,19–21,25–28,34,75]. However, until the beginning of the current Ph.D. project in 2015, no optimization effort, in particular for the use of mPSDs as in vivo dosimeter, was done. The main goal of the present Ph.D. project is to built the first mPSD system capable of accurately performing in vivo dosimetry measurements in HDR brachytherapy.

1.4.2 Specific objectives and system specifications

The development of a mPSD for in vivo dosimetry applications in HDR brachytherapy is the general objective of the doctoral project presented in this thesis. As this objective remains a global statement, several sub-objectives have been determined based on the work to be carried out to fulfill the main objective.

1. Design, build, optimize and characterize the response of a mPSD.
2. Design and optimize the mPSD's light detection system.
3. Perform a complete dosimetric characterization and assessment of the mPSD's system performance under HDR brachytherapy conditions.
4. Quantify the advantages and limitations of the use of different methods for mPSD's calibration.
5. Develop and test an algorithm for real-time source tracking and dwell time measurements in HDR brachytherapy:
    a) Dose measurement agreement with TG-43 U1 [46] within 10 %.
    b) Source position determination with 3 mm positional accuracy.
    c) Dwell time assessment with 1s measurement accuracy.
6. The quantification of the system's error detection level for common clinical scenarios.
7. Translation of the developed mPSD's system in the clinical setting for a technology clinical trial.

1.4.3 Project's impact and contribution

The stages of this project lead to the design of a complete preclinical prototype, comprising both the "detector" portion and the software component of signal analysis and visualization presented to the user. It meets existing clinical needs for which no solution is yet available. The system is currently used in a clinical protocol.

Chapter 2

Optimization of a multipoint plastic scintillator dosimeter for high dose rate brachytherapy

Haydee M. Linares Rosales[1,2], Patricia Duguay-Drouin[1,2], Louis Archambault[1,2], Sam Beddar[3], Luc Beaulieu[1,2]

[1]Département de physique, de génie physique et d'optique et Centre de recherche sur le cancer, Université Laval, Québec, Canada.

[2]Département de radio-oncologie et Axe Oncologie du CRCHU de Québec, CHU de Québec - Université Laval, QC, Canada.

[3]Department of Radiation Physics, The University of Texas MD Anderson Cancer Center, Houston, TX 77003, United States.

2.1 Résumé

Objectif: Cette étude est dédiée à l'optimisation et à la caractérisation de la réponse d'un détecteur multipoints à scintillateurs plastiques (mPSD) pour une application à la dosimétrie in vivo en curiethérapie HDR.

Méthodes: Une analyse exhaustive a été réalisée afin de concevoir un système mPSD qui maximise la collecte de lumière de scintillation produite par l'interaction des photons ionisants. Plus de 20 prototypes de détecteurs mPSD ont été construits et testés afin de déterminer l'ordre approprié des scintillateurs par rapport au photodétecteur (distal, central ou proximal), ainsi que leur longueur en fonction de la lumière de scintillation émise. Les éléments de détection disponibles sont les scintillateurs BCF-60, BCF-12 et BCF-10 (Saint Gobain Crystals, Hiram, OH, USA), séparés les uns des autres par des segments de fibres optiques claires Eska GH-4001 (Mitsubishi Rayon Co., Ltd ., Tokyo, Japon). La contribution de chaque scintillateur au spectre total a été déterminée par des irradiations dans la gamme des basses énergies (<120 keV). Pour le meilleur prototype de mPSD, une optimisation numérique a été effectuée afin de sélectionner les composants optiques (miroirs dichroïques, filtres et tubes photomultiplicateurs (PMT)) qui correspondent le mieux au profil d'émission lumineuse. Les calculs ont été effectués en tenant compte du spectre de scintillation et du rendement lumineux mesurés, de la transmission et de l'atténuation des composants optiques rapportées par le fabricant et de la réponse du PMT, telle que caractérisée expérimentalement. Le système dosimétrique optimisé pour être utilisé pour la mesure de dose en curiethérapie HDR. Le système est contrôlé indépendamment de la source ^{192}Ir via LabVIEW et lu simultanément à l'aide d'une carte NI-DAQ. Les mesures de dose en fonction de la distance de la source ont été effectuées selon les recommandations du TG-43U1. Les performances du système ont été quantifiées en termes de rapport signal sur bruit (SNR) et de rapport signal à bruit de fonds (SBR).

Résultats: Pour une meilleure collecte lumineuse globale, il a été déterminé que le BCF-60 devrait être placé en position distale, le BCF-12 au centre et le BCF-10 en position proximale par rapport au photodétecteur. Cette configuration a permis d'optimiser la transmission de la lumière à travers la fibre collectrice et d'éviter les effets d'excitation et d'auto-absorption entre les scintillateurs. La longueur optimale du scintillateur trouvée était de 3 mm, 6 mm et 7 mm pour BCF-10, BCF-12 et BCF-60, respectivement. L'optimisation de la collecte de lumnière des trois scintillateurs (forme spectrale finale) permet l'utilisation efficace de la déconvolution du signal en utilisant une approche multispectrale, en extrayant la dose de chaque élément tout en tenant compte de l'effet de tige Cerenkov. Les différences entre les mesures mPSD et TG-43U1 restent inférieures à 5% dans la plage de 0,5 cm à 6,5 cm de la source. Le système dosimétrique peut différencier correctement le signal de scintillation de du bruit de fonds pour une large gamme de conditions de débit de dose : le SNR s'est avéré supérieur à 5 pour des débits de dose supérieurs à 22 mGy/s tandis que le SBR minimum mesuré était de 1,8 à 6

mGy/s.

Conclusion: Un mPSD a été construit et optimisé pour la dosimétrie de curiethérapie HDR sur la base de la réponse spectrale dans différentes conditions. Il est suffisamment sensible pour permettre plusieurs mesures simultanées sur une plage de distances cliniquement utile, jusqu'à 6,5 cm de la source. Cette étude constitue une référence pour de futures applications nécessitant des mesures de dose en temps réel pour une large gamme de positions de source et de conditions de débit de dose.

2.2 Abstract

Purpose: This study is devoted to optimizing and characterizing the response of a multi-point plastic scintillator detector (mPSD) for application to in vivo dosimetry in HDR brachytherapy.

Methods: An exhaustive analysis was carried out in order to obtain an optimized mPSD design that maximizes the scintillation light collection produced by the interaction of ionizing photons. More than 20 prototypes of mPSD were built and tested in order to determine the appropriate order of scintillators relative to the photodetector (distal, center or proximal), as well as their length as a function of the scintillation light emitted. The available detecting elements are the BCF-60, BCF-12 and BCF-10 scintillators (Saint Gobain Crystals, Hiram, OH, USA), separated from each other by segments of Eska GH-4001 clear optical fibers (Mitsubishi Rayon Co., Ltd., Tokyo, Japan). The contribution of each scintillator to the total spectrum was determined by irradiations in the low energy range (< 120 keV). For the best mPSD design, a numerical optimization was done in order to select the optical components (dichroic mirrors, filters and photomultipliers tubes (PMTs)) that best match the light emission profile. Calculations were performed taking into account the measured scintillation spectrum and light yield, the manufacturer-reported transmission and attenuation of the optical components, and the experimentally characterized PMT noise. The optimized dosimetric system was used for HDR brachytherapy measurements. The system was independently controlled from the ^{192}Ir source via LabVIEW and read simultaneously using an NI-DAQ board. Dose measurements as a function of distance from the source were carried out according to TG-43U1 recommendations. The system performance was quantified in terms of signal to noise ratio (SNR) and signal to background ratio (SBR).

Results: For best overall light-yield emission, it was determined that BCF-60 should be placed at the distal position, BCF-12 in the center and BCF-10 at the proximal position with respect to the photodetector. This configuration allowed for optimized light transmission through the collecting fiber and avoided inter-scintillator excitation and self-absorption effects. The optimal scintillator length found was of 3 mm, 6 mm, and 7 mm for BCF-10, BCF- 12 and

BCF-60, respectively. The optimized luminescence system allowed for signal deconvolution using a multispectral approach, extracting the dose to each element while taking into account the Cerenkov stem effect. Differences between the mPSD measurements and TG-43U1 remain below 5% in the range of 0.5 cm to 6.5 cm from the source. The dosimetric system can properly differentiate the scintillation signal from the background for a wide range of dose rate conditions: the SNR was found to be above 5 for dose rates above 22 mGy/s while the minimum SBR measured was 1.8 at 6 mGy/s.

Conclusion: Based on the spectral response at different conditions, an mPSD was constructed and optimized for HDR brachytherapy dosimetry. It is sensitive enough to allow multiple simultaneous measurements over a clinically useful distance range, up to 6.5 cm from the source. This study constitutes a baseline for future applications enabling real time dose measurements and source position reporting over a wide range of dose rate conditions.

2.3 Introduction

In brachytherapy, radioactive sources are placed at a short distance from the target. The high dose gradients near brachytherapy sources (10% or more per millimeter for the first few centimeters from the source) provide a level of protection to healthy tissues surrounding the target. Despite the short distances involved in this modality, brachytherapy is not free from errors, which can be caused by humans (e.g., incorrect medical indication, source strength, patient identification, catheter, or applicator) or by failures in the treatment system (e.g., mechanical events) [5]. Even small errors in the source positioning can result in harmful consequences for patients. Systematic implementation of precise quality control and quality assurance protocols help to improve treatment quality, and routine use of real-time verification systems and in vivo dosimetry are even more helpful in determining whether there are deviations from the prescribed dose during treatment delivery. Performing these tasks requires a precise and accurate detector whose presence does not perturb the particle fluence and the physics interactions. Tanderup et al. [7] reviewed different detectors for potential use for in vivo brachytherapy dosimetry. The selection of the appropriate dosimetric system is a compromise between different requirements and constraints of the detector as well as the application sought.

Plastic scintillator detectors (PSDs) show promise for obtaining accurate real-time radiotherapy dose measurements. Previous studies have demonstrated that PSDs can accurately measure dose in external beam radiotherapy and that they have high spatial resolution, linearity with dose, energy independence in the megavolt energy range, and water equivalence [15–17, 19–21, 25–28]. In addition, some authors have found PSDs to be feasible for use in brachytherapy applications [18, 22–24, 29]. Despite the aforementioned advantages, PSD

response is affected by the stem effect and temperature dependence. Temperature dependence was long considered to be negligible, but recent studies showed that, depending on the type of scintillator, changes on the order of 0.6% per degree Celsius should be expected [26, 34]. Moreover, a non-negligible fraction of the light collected by PSDs consists of the stem effect which can be caused by two phenomena. The first phenomenon is direct excitation of the polymer chain, or fluorescence, from the plastic optical fiber guides, and the second is Cerenkov light production. Therriault-Proulx et al. [85] found that fluorescence yield is order of magnitude less intense than Cerenkov light. The intensity of Cerenkov light emitted in the optical fiber guide is up to 2 orders of magnitude lower per millimeter than the intensity of the scintillation light produced by the scintillator. However, the optical fiber guides within the radiation field are usually much longer than the scintillation probes, several centimeters versus a few millimeters at most for the scintillators [75]. Whether Cerenkov light requires removal in brachytherapy applications depends on the radioactive source used and the measurement geometry. In HDR brachytherapy with an ^{192}Ir source, Cerenkov radiation can cause large errors in dose reporting if it is not taken into account [22, 23]. The production and removal of Cerenkov light in PSDs are widely discussed topics [16, 17, 20, 32, 35–37, 75]. In this study, the stem effect is accounted for.

Most studies that have characterized PSDs have been conducted using an optical fiber connected to a single point of measurement as the sensitive volume. Multiple scintillation sensors attached to a single optical chain have been used, but their application is limited to measurements made within 3 cm of an HDR brachytherapy source [31–33]. New multipoint PSDs (mPSDs) could assess the dose at multiple points simultaneously, thereby improving treatment quality and accuracy. The multi-hyperspectral filtering method proposed by Archambault et al. [32] led to the conception of an mPSD in which each scintillator has an independent signal. Such an arrangement would allow simultaneous determination of the absorbed dose at different locations in a volume [9, 31, 33].

The purpose of this study was to evaluate the performance of an mPSD in terms of sensitivity and accuracy, resulting in a thorough optimization of the optical chain, with applications to in vivo HDR brachytherapy in mind. To achieve this goal, three steps were followed. First, an experimental study was carried out to look for an optimal mPSD configuration. As the second step, we performed numerical optimizations to determine the proper configuration of the scintillation light detection system. In a third, and final stage, we evaluated the performance of the entire system in HDR brachytherapy.

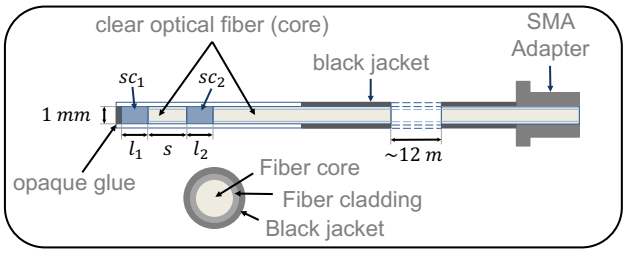

Figure 2.1 – Design schematic of an mPSD. sc_1 and sc_2 indicate scintillators 1 and 2, respectively; l_1 and l_2 denote the scintillator lengths. s is the separation between the scintillators, 1 cm of clear optical fiber. Figure not to scale. SMA, subminiature version A.

2.4 Materials and Methods

2.4.1 Optical chain

The optical chain in the proposed system has components that (1) generate scintillation light in the mPSD, (2) detect the scintillation light, and (3) analyze the signal.

The scintillating fibers used in this study were the plastic scintillators BCF-10, BCF-12, and BCF-60 from Saint Gobain Crystals (Hiram, OH, USA). Figure 2.1 shows the design schematic of a typical mPSD. The scintillators were separated from each other by 1 cm of clear optical fiber (Eska GH-4001, Mitsubishi Rayon Co., Ltd., Tokyo, Japan). The same type of fiber was also used to conduct the scintillating light to the photodetector surface. (Here, "clear" refers to a fiber in which no scintillation light is produced.) The aim of this study is to optimize a 3-point mPSD configuration. A single investigation with a 2-point mPSD was carried out, which is described in the following sections. All optical interfaces (scintillators and clear optical fibers) were polished using a SpecPro automated optical fiber polisher (Krell Technologies, Neptune City, NJ, USA) with successive grain sizes of 30 μm, 9 μm, 3 μm, and 0.3 μm. The detectors were constructed using a previously described coupling technique [88].To ensure the reproducibility of the polishing and coupling techniques, we verified that the light collection across multiple detector samples does not vary more than 5 %. Each 1-mm-diameter detector prototype was made light-tight using a black polyether block amide jacket from Vention Medical (Salem, NH, USA). The scintillating tip was sealed with a mixture of epoxy and black acrylic paint.

The scintillation light signal was guided to the photodetector surface by a clear optical fiber, which was attached to the photodetector with a subminiature version A connector (11040A, Thorslab, Newton, NJ, USA). Two types of photodetector were used: (1) an Ocean Optics QE65Pro spectrometer (Dunedin, FL, USA) and (2) a set of photomultipliers tubes (PMTs) coupled to dichroic mirrors and filters from Hamamatsu (Bridgewater, NJ, USA) [89]. When the PMTs were used as the photodetector, the signal was read by a data acquisition board (NI

USB-6289 M Series Multifunction I/O Device, National Instruments, Austin, TX, USA), and LabVIEW software version 15.0f2 (National Instruments) was used during the signal analysis stage [90].

2.4.2 Experimental determination of the optimal mPSD configuration

The purpose of this step was to identify the best configuration of scintillators in an mPSD. Interchangeable radiosensitive tips containing the scintillators were coupled to a clear optical fiber, which conveyed the light signal to the photodetector. We built and tested more than 20 mPSD prototypes using various combinations of scintillator positions and lengths to determine (1) the optimal position for each scintillator within the fiber and (2) the optimal length of each scintillator.

To evaluate the effect of scintillator position on the recorded signal, (A) the lengths of the scintillators inside the radiosensitive tips were kept identical (3 mm of BCF-10, 6 mm of BCF-12, 7 mm of BCF-60), and (B) the positions of the scintillators inside the fiber were altered. Each scintillator was placed in a distal, central, or proximal position relative to the photodetector surface. To determine the optimal scintillator length in terms of the scintillation light produced and spatial resolution, each scintillator was varied in length from 3 mm to 14 mm. The hyperspectral approach [32] dictated a balanced signal contribution from each scintillator to the overall light collection, while the spatial resolution of the dose required detection elements that were as small as possible.

For each possible combination of scintillator number, position, and length, the total emission spectrum was obtained from simultaneous irradiation of all the scintillators in the fiber. Then, in order to obtain their individual contributions to the total emission spectrum, each scintillator was individually irradiated. Lead blocks were used to shield the neighboring scintillators from the incoming radiation.

The spectral distributions were obtained with the spectrometer cooled to -20 °C and the integration time set to 40 s. Background signals acquired prior to exposures were subtracted from the scintillation light signals.

The analysis in this section was performed under a fixed irradiation condition with an X-ray therapy system. A tube voltage of 120 kV (maximum photon energy of 120 keV) was selected to avoid Cerenkov light production. Several measurements were carried out in the low-energy range using an Xstrahl 200 (Xstrahl Ltd., Camberley, UK). Continuous beam irradiations with a tube current of 10 mA were performed according to the specifications shown in Table 2.1.

Table 2.1 – Main irradiation parameters when using a *Xstrahl 200* x-ray therapy system.

Energy (kV)	HVL_1 (mm)	Added filtration (mm)	Field size (cm)
120	5.0 Al	0.5 Al+0.10 Cu	10*

HVL = Half-Value Layer
* *diameter to circular shape*

2.4.3 Determination of the optimal scintillation light detection system.

In the second step, we sought the appropriate optical components for the light detection system used during measurements. Having a complete spectral characterization led us to perform a numerical analysis to determine the optical chain that would allow optimal scintillation light collection.

In our experimental set-up, scintillation light was read by an assembly of PMTs, which were coupled to a set of dichroic mirrors and filters that deconvolved the collected light into spectral bands. PMTs were chosen as the photodetectors because they have a high signal-to-noise-ratio (SNR) and readout speed that overcomes many of the sensitivity issues of charge-coupled device-based systems. Generally, PMTs more accurately measure low light signals and have a faster response, making them more suitable for the demands of in vivo dosimetry applications [24, 28, 91]. Henceforth, an assembly composed of a dichroic mirror, filter, and PMT will be referred to as a "channel". From an optimization perspective, the signal produced in each channel was calculated, taking into account the measured scintillation spectrum and light yield, the manufacturer-reported transmission and attenuation of the optical components, and the experimentally characterized PMT noise. The experimental spectral characterization obtained for the mPSD constituted the main input. That spectral information was then used to construct the optical system and simulate its response when interacting with a radiation beam. No particle transport through Monte Carlo simulations was performed. A large set of possible component combinations (brute force) was explored to find the configuration that provided the best SNR. For the calculations, we used the characteristics of filters and dichroic mirrors from Hamamatsu series A10033 and A10034, respectively. For the PMTs, the models used corresponded to Hamamatsu series H10722. The numerical optimization took into account the fact that the number of channels depended on the number of scintillator points N composing the mPSD and equaled $N + 1$. This procedure allowed us to optimize light transmission and to minimize the contribution of elements generating spurious light (as will be shown in Figure 2.7).

2.4.4 Performance of the mPSD system in HDR brachytherapy

With the optimized system, we next evaluated the performance of a 3-point mPSD in HDR brachytherapy. A Flexitron HDR afterloader (Elekta, Stockholm, Sweden) was used with an ^{192}Ir source. The cylindrical ^{192}Ir source pellet was 0.6 mm in diameter and 3.5 mm in length and was housed inside a stainless steel capsule 0.86 mm in diameter and 4.6 mm in length. The source air kerma strength was 32226 U. The HDR brachytherapy unit was remotely controlled and able to move the source to the desired position in a water tank by means of a 30 cm needle set from Best Medical International (Springfield, VA, USA). The mPSD dimensions allowed it to be inserted into an additional catheter for use during real-time dose verification.

To be consistent with the TG-43U1 formalism [46], measurements were performed with the source and detector isotropically covered by at least 20 cm of water. To ensure the accuracy and reproducibility of the source-to-detector distance, all the catheters were inserted in a custom-made poly(methyl methacrylate) phantom (Figure 2.2a), which was in turn placed inside a 40 $\times$ 40 $\times$ 40-cm^3 water tank. As shown in Figure 2.2,the phantom was composed of 2 catheter insertion templates of 12 $\times$ 12 cm^2, separated by 20 cm. This phantom allowed for source-to-detector parallel displacement. Figure 2.2b shows the experimental set-up used during measurements. 10 catheters were inserted in the template phantom at distances ranging from 0.5 cm to 7.0 cm away from the mPSD catheter. Three dwell positions per catheter were planned. Following the axis convention shown in figure 2.2a, the source z locations were chosen relative to the effective center of each scintillator volume.

The dosimetric system was initially calibrated under the same conditions used to perform the measurements, following the TG-43U1 [46] and hyperspectral [32] formalisms. The luminescence dosimetry system was controlled using LabVIEW software. A gain input voltage of 1 V was assigned to each PMT, producing a channel output of 2×10^6. The linear relationship between the input voltage and the gain was assessed for voltage between 0.5 V and 1.1 V. For each measurement channel, 70000 samples per second were acquired. Dose values were recorded in real time by the mPSD. All measurements were repeated at least 5 times, and the measurement set-up was completely unmounted between each measurement. Statistical variations in the readings were determined by setting a source dwell time of 60 s per dwell position.

The sensitivity of the dosimetry system was evaluated using the SNR and the signal-to-background ratio SBR associated with each scintillator during HDR brachytherapy measurements. Figure 2.3 is a representation of a typical signal pulse, showing the magnitudes that were used in SNR and SBR determination: μ_s, the mean signal; μ_b, the mean background signal; σ_s the signal standard deviation; and σ_b the background standard deviation.

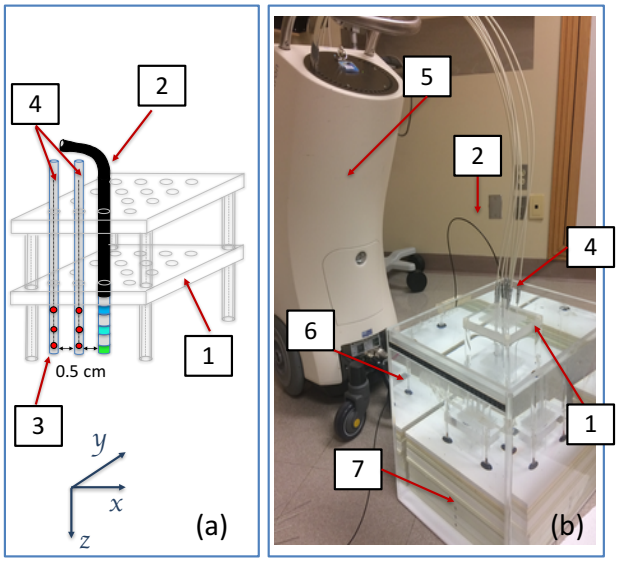

Figure 2.2 – (a) Schematic of the poly(methyl methacrylate) (PMMA) phantom constructed for HDR brachytherapy measurements with an mPSD. The catheter positioning allowed source displacement parallel to the mPSD. (b) Experimental set-up for HDR brachytherapy measurements. (1) PMMA phantom, (2) mPSD, (3) ^{192}Ir source, (4) 30-cm catheters, (5) Flexitron HDR afterloader unit, (6) 40 × 40 × 40-cm^3 water tank, (7) solid-water slabs.

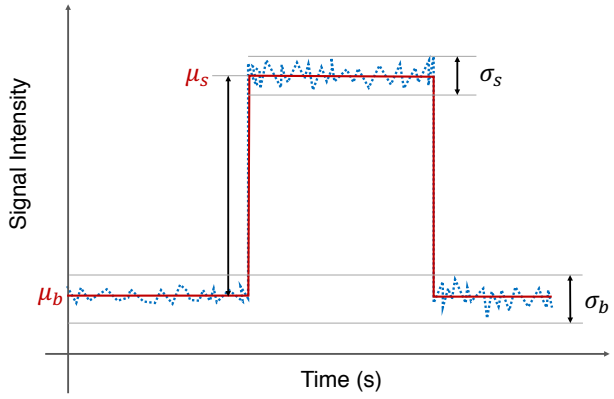

Figure 2.3 – Typical signal pulse used for signal-to-noise ratio and signal-to-background ratio calculations. The indicated values are: μ_s, mean signal value; μ_b, mean background value; σ_s, signal standard deviation; σ_b, background standard deviation and the difference between μ_s and μ_b.

$$SNR = \frac{\mu_s}{\sigma_s} \tag{2.1}$$

$$SBR = \frac{\mu_s}{\mu_b} \tag{2.2}$$

The SNR is a commonly used metric for characterizing the global performance of optoelectronic systems. In the case of PSD performance assessment, the noise term includes Cerenkov radiation. A few SNR studies using PMTs as the photodetector have been performed [91–93]. The scintillator SNR as function of dose rate was obtained using equation 2.1, where the numerator represents the mean signal for a determined irradiation in a fixed time, and the denominator is the standard deviation of the collected signal. SBR was determined according to equation 2.2 and is the ratio of the mean signal value and the mean background value for a fixed irradiation time.

2.4.5 Cerenkov radiation removal

In our study, multiple probes were read by a single clear collecting optical fiber; thus, we used the hyperspectral filtering technique proposed by Archambault et al. [32] as the stem effect removal method during HDR brachytherapy measurements. Equations 2.3, 2.4 and 2.5 represent the removal method for an mPSD configuration. Dose calculation in mPSDs is based on the assumption that the recorded signal results from the linear superposition of spectra; no self-absorption interactions among the scintillators composing the mPSD are considered [32]. The idea behind this formalism is that once the light emission of each component at different wavebands is known, the total signal recorded can be decoupled, and the signal fraction contributed by each scintillator can be determined.

$$m = Rx \tag{2.3}$$

$$\begin{pmatrix} d_{p1,1} & d_{p1,2} & d_{p1,3} & d_{p1,4} \\ d_{p2,1} & d_{p2,2} & d_{p2,3} & d_{p2,4} \\ d_{p3,1} & d_{p3,2} & d_{p3,3} & d_{p3,4} \end{pmatrix} = \begin{pmatrix} C_{p1,L_1} & C_{p1,L_2} & C_{p1,L_3} & C_{p1,L_4} \\ C_{p2,L_1} & C_{p2,L_2} & C_{p2,L_3} & C_{p2,L_4} \\ C_{p3,L_1} & C_{p3,L_2} & C_{p3,L_3} & C_{p3,L_4} \end{pmatrix} \times \begin{pmatrix} m_{L_1,1} & m_{L_1,2} & m_{L_1,3} & m_{L_1,4} \\ m_{L_2,1} & m_{L_2,2} & m_{L_2,3} & m_{L_2,4} \\ m_{L_3,1} & m_{L_3,2} & m_{L_3,3} & m_{L_3,4} \\ m_{L_4,1} & m_{L_4,2} & m_{L_4,3} & m_{L_4,4} \end{pmatrix} \tag{2.4}$$

$$d' = C \cdot m' \tag{2.5}$$

A raw measurement m with the mPSD system is a function of a given photon flux x (the number of photons emitted for a given emission source, either scintillating elements or any

other source of light) and the system response matrix R. In equation 2.3, m is a vector of L elements; R is $L \times N$ dimensions, and x is a vector of N elements. L represents different wavelength filters or channels. The number of measurement channels L should be equal to $N + 1$. The additional channel is included to take into account the stem effect, which should be removed from the measured signal [22].

Equation 2.4 is the mathematical equation for determination of the calibration coefficient. The dose $d_{i;k}$ received by the scintillator during irradiation is directly proportional to the number of scintillation photons in the absence of losses (quenching); for this reason, $d_{i,k} = a_i x_{i,k}$, a_i being a proportionality constant and $x_{i,k}$ the photon fluence in the scintillating material i during the measurement at position k. However, knowing the dose at a specific point requires a previous calibration to determine the matrix of calibration coefficient C for each scintillation point as well as each measurement channel. For such a calibration the dose (e.g., $d_{p1,p2,p3,p4}$) should be known at each point p. We calculated these dose values by using the TG-43U1 formalism [46]. To account for the finite size of each scintillator, TG-43U1 dose values were integrated over each scintillator's sensitive volume.

Once the matrix of calibration coefficients C is known, the dose d' at each point can be determined using equation 2.5, where m' represents the raw data acquired during measurements. The apostrophe in equation 2.5 is used to highlight that this is a new set of measurements, the goal of which is to determine the absorbed dose, not the calibration coefficient, which is already known at this stage.

2.5 Results and discussion

2.5.1 mPSD optimal configuration

Scintillator position within the fiber

A single investigation was performed with a 2-point mPSD configuration to determine the optimal order of scintillators in the mPSD. Each scintillator spectrum was measured independently. Figure 2.4 shows the individual spectra with intensities normalized to a 1-mm scintillator length. As shown in the figure, the scintillation intensity was strongest in the BCF-10 scintillator, whereas the BCF-60 scintillator had the weakest scintillation intensity.

In all the tested combinations, the scintillator's individual spectra evidenced no self-absorption or cross-excitation effects. The main differences observed related to the position occupied by each scintillator inside the fiber. Table 2.2 shows the measured signal proportion for different 2-point mPSD configurations. For each configuration, the proportion of the total signal coming from each independent scintillator was calculated by determining the area under the curve.

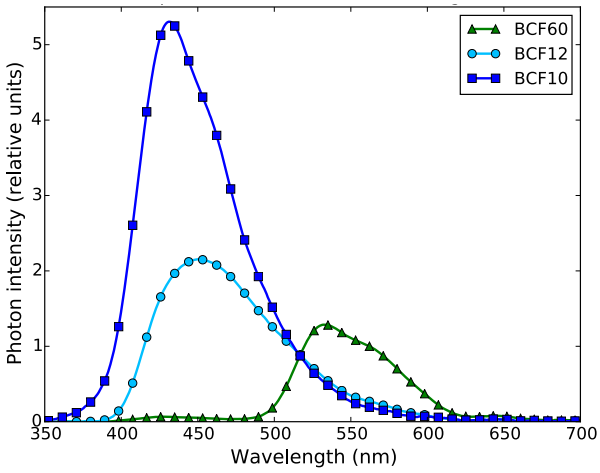

Figure 2.4 – Individual scintillator spectra normalized to a 1-mm-long scintillator.

Table 2.2 – Scintillator signal proportion (in %) for each combination of scintillators and positions inside the optical fiber.

		Proximal		
		BCF-10	BCF-12	BCF-60
Distal	BCF-10	-	8.6/91.4	17.6/82.4
	BCF-12	18.8/81.2	-	7.2/93.8
	BCF-60	37.4/62.6	8.8/91.2	-

The signal proportion was more balanced when a BCF-60 scintillator was placed in the distal position and coupled to a BCF-10 scintillator. At 530 nm, the BCF-60 signal represented 37% of the total signal when coupled to a BCF-10 scintillator but only 9% when coupled to a BCF-12 scintillator. Therefore, this combination of scintillators and positions is recommended for a 2-point mPSD.

The signal analysis demonstrated that the shorter wavelength scintillator should always be placed closer to the photodetector and the longer wavelength scintillator in the distal position. Because of the Stokes shift, the absorption spectrum always has a lower wavelength range than the emission spectrum. If the aforementioned configuration is not used, inter-scintillator excitation and self-absorption effects can take place, and as a consequence, the light transmission through the collecting fiber is not optimal. To exemplify this effect, 3-point mPSDs with 2 different configurations of scintillator positions inside the fiber were constructed. Their spectral distributions are shown in Figure 2.5. Figure 2.5a shows the spectra with the BCF-10 placed at the distal position, the BCF-60 in the center, and the BCF-12 in the proximal position. Almost all of the light produced by the BCF-10 scintillator was absorbed by the neighboring scintillators, whose photon intensities were higher than they were in the optimal configuration (Figure 2.5b). Hence, in the subsequent experiments, we used mPSDs in which the scintillators were placed inside the optical fiber in decreasing order of wavelength from distal to proximal

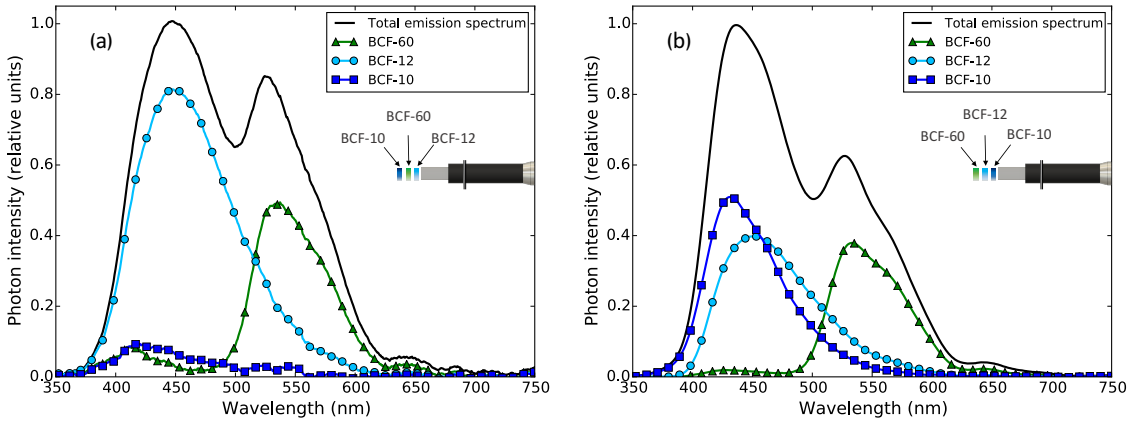

Figure 2.5 – (a) Stokes shift effect. (b) Spectral distributions obtained with all scintillators in the optimal positions.

positions.

In the case of a 3-point mPSD composed of 3 mm of BCF-60 at the distal position, BCF-12 in the center, and BCF-10 at the proximal position (mPSD prototype P1 in Figure 2.6), we observed no self-absorption or cross-excitation effects, but the scintillator's independent signals were not balanced at all. In such a case, the scintillation process is more efficient in BCF-10 than in the other scintillators, accounting for almost 71% of the total signal. The intensities of BCF-12 and BCF-60 were closer to one another, with 20% and 9% of the total signal, respectively.

Optimal scintillator length

The intensity of the measured scintillation light depends on the scintillator size, the coupling method, the fiber core size, and the fiber numerical aperture. To determine the optimal length of each scintillator, 9 different 3-point mPSD prototypes were constructed. Figure 2.6 shows the contributions of individual scintillator signals for each of the 3-point mPSDs and specifies the length of each scintillator in millimeters. As indicated by the shadowed region in Figure 2.6, detector configurations P6 to P9 provided the required balanced signals for optimal hyperspectral deconvolution. P9 was selected as the optimal detector because it also minimized variations in sensor length. In the P9 mPSD, the BCF-10 scintillator was 3 mm long, the BCF-12 scintillator was 6 mm long, and the BCF-60 scintillator was 7 mm long.

	Length (mm)					
	P1	P4	P6	P7	P8	P9
BCF10	3	11	4	1	3	3
BCF12	3	11	6	5	7	6
BCF60	3	10	13	14	11	7

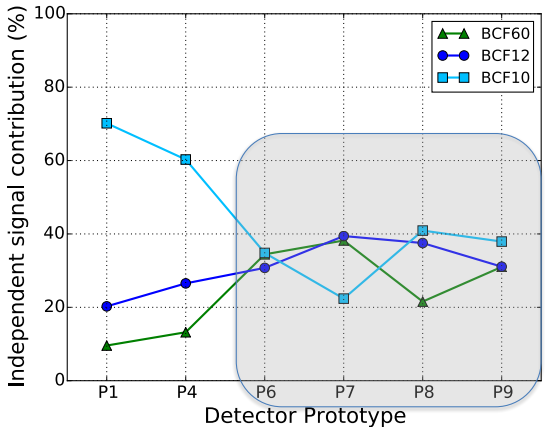

Figure 2.6 – Fraction of the total scintillation light produced by each scintillator as a function of its length. The shaded region indicates the combination of sensor lengths that result in balanced signals.

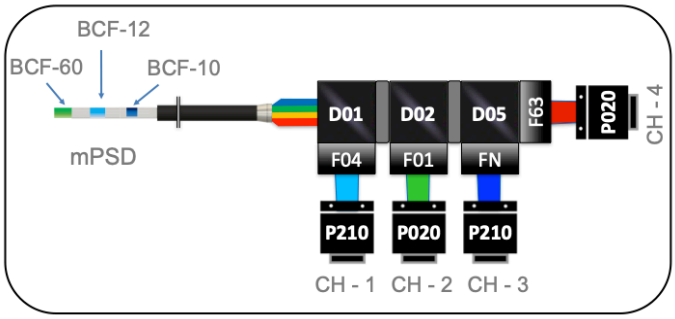

Figure 2.7 – Schematic of the light collection system obtained from calculations. All the components used were from Hamamatsu. D indicates dichroic mirrors from series A10034, F indicates filters from series A10033, and P210 and P020 refer to PMTs H10722 210 and 020, respectively. CH indicates the channel number. FN refers to a filter that transmits 100% of the incoming light to the photodetector in the wavelength range of 300 nm to 500 nm

.

2.5.2 Optimized scintillation light detection system

Following the determination of the optimal length, the numerical optimization allowed us to determine the best combination of components to be used for the measurements of the light collection system. Figure 2.7 shows a schematic of the appropriate arrangement of the components of the light collection system obtained from these calculations.

This assembly filtered the total emission spectrum from the mPSD to produce a filtered spec-

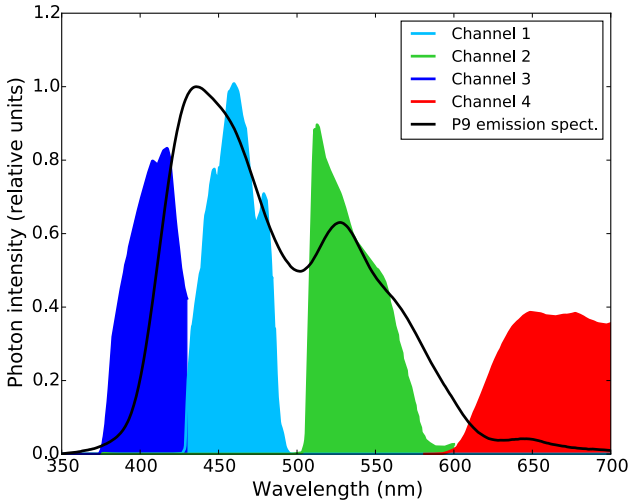

Figure 2.8 – Emission and filtered spectra produced by the P9 mPSD prototype used for absorbed dose determination. The filtered spectra for each channel were obtained by applying optical filtration to the light entering each PMT.The intensities in the emission and filtered spectra are normalized to their maximum intensity.

trum entering each PMT. The PMT's voltage output is then used to calculate the absorbed dose in the absence of Cerenkov radiation. Figure 2.8 shows each channel's filtered spectrum and the total emission spectrum of the scintillation light generated by the P9 mPSD.

The study done by Therriault-Proulx et al. [9] in HDR brachytherapy uses the same scintillating elements described in this work (BCF-10, BCF-12, and BCF-60; Saint-Gobain Crystals, Hiram, OH), but with different positions inside the optical assembly. In that work it was suggested to use the BCF-10 in the central position while BCF -12 at the proximal position with respect to the photodetector surface. Based on the signal analysis performed in this study, we propose an optimized mPSD design that maximizes the scintillation light collection, resulting in the configuration shown in Figure 2.7, which inverts the BCF-10 and BCF-12 positions.

2.5.3 Performance of the mPSD system in HDR brachytherapy

Absorbed dose as function of distance

Dose distributions in terms of distance to an HDR brachytherapy source were obtained, with the P9 mPSD calibrated at 1.5 cm from the ^{192}Ir source. This calibration distance represented a compromise between measurement uncertainties and positioning uncertainties. Andersen et al. [8] demonstrated that positioning uncertainty dominates in measurements close to the source, whereas measurement uncertainty dominates at long distances. In order to ensure that we had enough data in the response recording, a source dwell time of 60 s was used at each dwell position.

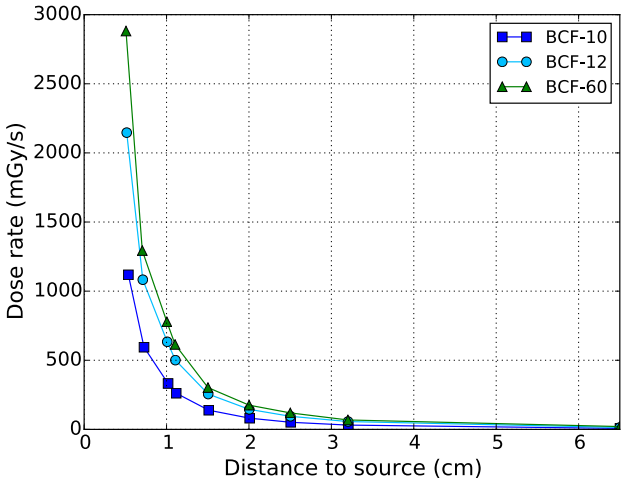

Figure 2.9 – Scintillator dose rates as a function of distance to the HDR brachytherapy source. The distances to the source are relative to each scintillator effective center.

Figure 2.9 shows dose rate readings for each scintillator, and Table 2.3 details the standard deviations for each distance to the brachytherapy source. For all 3 scintillators, the standard deviations were generally no greater than 5% of the mean dose reading, although this value, as expected, increased with distance from the source. At a distance of 6.5 cm, the standard deviation exceeded 10% for all scintillators. At that distance, the source radiation does not produce enough scintillation in the mPSD, so the recorded signal can be considered to be background. Nonetheless, the absolute standard deviation was small relative to the mean dose. TG-43U1 dose values were used as a reference; the last column in Table 2.3 presents the differences between the measured dose and the TG-43U1 dose values at each distance to the brachytherapy source. In general, the measured mPSD dose and the TG-43U1 dose agreed well at short distances to the source, but the difference increased as the source moved away from the mPSD.

Evaluation of scintillation signal and system sensitivity

Figure 2.10a shows the SNR in terms of dose rate for each scintillator in detector P9. According to the Rose criteria, proper recognition (detection) of an object strongly depends on SNR, only becoming possible when SNR exceeds 5; detection performance degrades as SNR approaches zero [94]. Thus, an SNR of 5 was the minimum sensitivity considered in this study. The BCF-10 and BCF-12 scintillators produced an SNR greater than 5 at all distances to the source. At dose rates below 22 mGy/s, the SNR produced by the BCF-60 scintillator fell below 5. These data suggest that, with regard to SNR, the dosimetric system characterized in this study is sensitive enough to measure dose rates above 22 mGy/s at distances to the source below 6.4 cm.

Table 2.3 – Standard deviation (SD) of 3-point mPSD measurements and deviation of the mean measured dose from the values predicted by TG-43U1. The distances to the source are relative to each scintillator effective center.

	Distance to source	**Dose per 1s reading**	**SD**		**Deviation from TG-43U1**	
	(cm)	(mGy)	(%)	(mGy)	(%)	(mGy)
BCF-10	0.5	1117.9	0.7	7.7	3.0	33.2
	0.7	594.4	0.7	4.2	1.1	6.5
	1.0	332.0	1.2	4.1	1.1	3.6
	1.1	261.6	1.6	4.2	3.7	9.7
	1.5	138.7	2.8	3.9	3.8	5.3
	2.0	80.9	4.2	3.4	5.5	4.5
	2.5	51.3	4.5	2.3	7.5	3.9
	3.2	31.0	4.1	1.3	7.3	2.3
	6.5	6.0	12.8	0.8	21.3	1.3
BCF-12	0.5	2146.6	0.5	10.3	1.1	23.2
	0.7	1082.6	0.7	7.2	0.8	9.1
	1.0	633.6	0.8	5.3	2.5	15.6
	1.1	500.9	0.8	3.9	2.2	11.1
	1.5	255.4	2.0	5.2	2.0	5.1
	2.0	144.8	4.2	6.1	2.2	3.2
	2.5	94.6	3.1	2.9	2.0	1.9
	3.2	56.6	3.2	1.8	2.3	1.3
	6.5	13.3	11.2	1.5	12.4	1.6
BCF-60	0.5	2881.6	0.4	11.3	2.3	66.9
	0.7	1293.6	0.7	8.5	0.6	7.2
	1.0	778.5	1.2	9.4	3.4	26.7
	1.1	614.3	1.2	7.1	4.3	26.3
	1.5	302.6	1.7	5.0	0.8	2.5
	2.0	175.2	6.5	11.4	1.0	1.8
	2.5	119.2	5.0	5.9	2.4	2.9
	3.2	68.1	6.8	4.6	1.7	1.2
	6.5	21.9	20.9	4.6	13.7	3.0

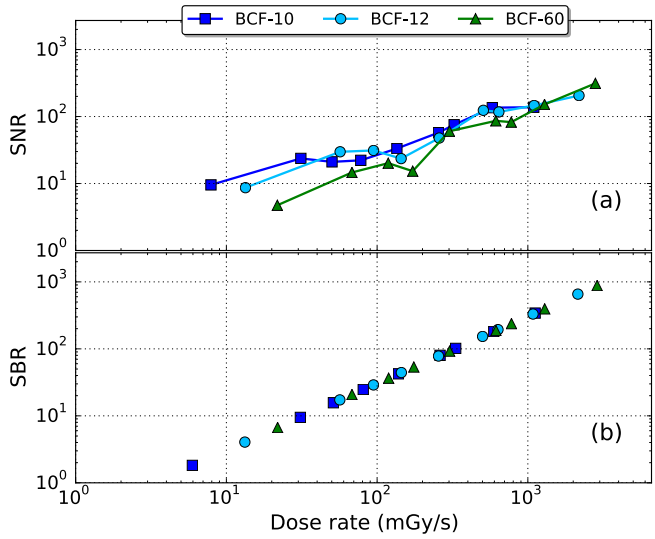

Figure 2.10 – Signal-to-noise ratio (SNR) and (b) signal-to-background ratio (SBR) as a function of dose rate for BCF-10, BCF-12, and BCF-60 scintillators in the P9 mPSD prototype. Shaded areas at the bottom of the graphs indicate the cutoff values for each parameter.

SNR analysis of PSD responses for various photodetectors was conducted by Boivin et al. [91] in the energy range of clinical interest. SNR values in a range of 100 to 1000 for dose rates between 0.1 mGy/s and 30 mGy/s were reported, being around 2 orders of magnitude greater than the results obtained in the low dose rate range of this study. The differences are easily explained by the differences in design. First, the study done by Boivin et al. [91] was conducted with a single point configuration detector that only had a single coupling interface, while the one reported in this study has 5 coupling interfaces intrinsicly decreasing the overall light collection in mPSD. Secondly, the scintillator size used in the study done by Boivin et al. [91] was 10 mm vs. a maximum size of 7 mm in the mPSD. Thirdly and most important, the system used here is subject to optical filtration of the light produced; Boivin et al. [91] used a system with no optical filtration, recording the signal of a PSD directly on a PMT module.

To evaluate how well the dosimetric system differentiated a signal pulse from the background signal, SBR values were calculated at each dose rate. Furthermore, several signal acquisitions were performed without irradiation resulting in a background signal value of $\mu_b \pm 0.16$ %. To properly differentiate signal from background, a minimum SBR of 2 is required. Figure 2.10b shows the SBR results obtained for each scintillator in the mPSD. The SBR for the BCF-10 scintillator fell below the SBR cutoff value for dose rates of around 6 mGy/s at 6.5 cm relative to the source, with an SBR of 1.8. The SBR is directly proportional to the photon fluence from scintillation, which is in turn proportional to the scintillator volume. According to the previously determined optimal mPSD design, the length of the BCF-10 scintillator was only 3 mm. The dose rate range could be extended by increasing the length of the scintillator, but at the cost of spatial or temporal resolution. As the background signal was almost constant in

the explored dose rate range, all the scintillators evidenced almost perfectly linear behavior.

The mPSD system studied by Therriault-Proulx et al. [9] is limited to HDR brachytherapy measurements within 3 cm from the source. The system proposed here is able to accurately perform dose measurements beyond 3 cm with a high collection efficiency.

2.6 Conclusions

In this study, we optimized an mPSD system that can be used clinically in HDR brachytherapy. We found that the scintillation light emission per millimeter of scintillator was more efficient in BCF-10 than in BCF-12 or BCF-60 scintillators. Furthermore, we experimentally determined the appropriate position of each scintillator inside the fiber: the scintillating element with the shorter wavelength should be placed closer to the photodetector, whereas the scintillator with the longer wavelength should be placed distally. In a 2-point mPSD, the most balanced signal was obtained with BCF-10 placed proximally and BCF-60 placed distally. We also evaluated a 3-point mPSD consisting of BCF-10, BCF-12, and BCF-60 scintillators. The best prototype used 3 mm of BCF-10, 6 mm of BCF-12, and 7 mm of BCF-60. Those dimensions were determined not only on the basis of light emission balance, but also with the aim of improving the detector's spatial resolution. Finally, an optimal light collection system was evaluated in HDR brachytherapy simulations. The evaluated mPSD produced minimal deviations in dose rate readings, and analysis of SNR and SBR showed that the detector provided accurate real-time dose measurements.

Acknowledgement

The present work was supported by the National Sciences and Engineering Research Council of Canada (NSERC) via the NSERC-Elekta Industrial Research Chair grant No. 484144-15 and by a Canadian Foundation for Innovation (CFI) JR Evans Leader Funds #35633. Haydee Maria Linares Rosales further acknowledges the support from Fonds de Recherche du Québec - Nature et Technologies (FRQ-NT) and by the CREATE Medical Physics Research Training Network grant of the Natural Sciences and Engineering Research Council of Canada (Grant # 432290). We also would like to thank Amy Ninetto from the Department of Scientific Publications of the University of Texas MD Anderson Cancer Center for editing our manuscript.

Chapter 3

Dosimetric performance of a multi-point plastic scintillator dosimeter as a tool for real-time source tracking in high dose rate ^{192}Ir brachytherapy

Haydee M. Linares Rosales[1,2], Louis Archambault[1,2], Sam Beddar[3,4], Luc Beaulieu[1,2]

[1]Département de physique, de génie physique et d'optique et Centre de recherche sur le cancer, Université Laval, Québec, Canada.

[2]Département de radio-oncologie et Axe Oncologie du CRCHU de Québec, CHU de Québec - Université Laval, QC, Canada.

[3]Department of Radiation Physics, The University of Texas MD Anderson Cancer Center, Houston, TX 77003, United States.

3.1 Résumé

Objectif: Cette étude vise à présenter les performances d'un détecteur multipoints à scintillateurs plastiques (mPSD) optimisé en tant qu'un outil pour les mesures de dose en temps réel, la triangulation de la position de la source et l'évaluation du temps d'arrêt en curiethérapie haut débit de dose (HDR).

Méthodes: Un système de capteur à trois points précédemment caractérisé a été utilisé pour les mesures de curiethérapie HDR. Le détecteur était composé de trois scintillateurs : BCF60, BCF12 et BCF10. La lumière de scintillation a été transmise à travers une fibre optique transparente de 1 mm de diamètre et lue par un assemblage compact de tubes photomultiplicateurs (PMT). Chaque composante a été optimisée numériquement pour permettre la déconvolution du signal en utilisant une approche multispectrale et en prenant soin de retirer la contribution de l'effet de tige Cerenkov pour extraire la dose de chaque scintillateur individuellement. Les PMT ont été lues simultanément à l'aide d'une carte d'acquisition de données à un taux de 100 kHz et contrôlées avec un logiciel basé sur Python. Une source de ^{192}Ir (Flexitron,Elekta-Brachy) a été contrôlée à distance (via un projecteur de source) et envoyée à diverses positions via un support en PMMA, assurant une précision de 0,1 mm. Des mesures de dose couvrant une plage de mouvement de la source par rapport au mPSD de 10 cm ont été effectuées conformément aux recommandations du TG-43 U1. Des mesures dans l'eau ont été effectuées afin de : (1) caractériser la réponse du système en terme de dépendance angulaire ; (2) obtenir la contribution relative des incertitudes de positionnement et de mesure à l'incertitude totale du système ; (3) évaluer la résolution temporelle du système ; et (4) suivre la position de la source en temps réel. Le principe de triangulation a été appliqué pour rapporter la position de la source dans l'espace tridimensionnel.

Résultats: Tel qu'attendu, l'incertitude de positionnement domine près de la source, tandis que l'incertitude de mesure est la contribution dominante à de plus grandes distances. Une incertitude de mesure maximale de 17 % a été observée pour le scintillateur BCF60 à 10 cm de la source. Sur la base de la chaîne d'incertitude, les meilleurs compromis entre les incertitudes de positionnement et de mesure ont été atteints pour des distances source-scintillateurs de 17,2 mm, 17,4 mm et 17,5 mm pour le BCF10, BCF12 et BCF60 respectivement. Ceci correspond donc aux distances optimales recommandées pour fins d'étalonnage. Le détecteur ne présentait aucune dépendance angulaire. Toutes les valeurs de dose se sont révélées être à moins de 2% de celle à 90°. Concernant les mesures visant la détermination de la position de la source, le système a fourni un emplacement avec un écart type inférieur à 1,7 mm à la valeur attendue. Les différences maximales observées entre les valeurs mesurées et attendues étaient respectivement de 1.82 mm et 1,80 mm dans les directions x et z. Les écarts entre les valeurs expérimentales et les valeurs de référence selon le TG-43 étaient inférieurs à 5% pour toutes les conditions de mesure explorées. En ce qui concerne la précision de la mesure

du temps d'arrêt, l'écart maximal observé était de 0,5 ±0,25 s et la moyenne pondérée (des trois scintillateurs) est inférieure à 0,33 ± 0,37 s pour toutes les distances couvertes dans cette étude.

Conclusion: Des mesures de curiethérapie HDR ont été effectuées avec un système mPSD optimisé. Les performances du système ont démontré qu'il pouvait être utilisé pour la mesure simultanée, en temps réel, de la dose, du temps d'arrêt et de la position de la source pendant la curiethérapie HDR.

3.2 Abstract

Purpose: This study aims to present the performance of a multi-point plastic scintillation detector (mPSD) as a tool for real-time dose measurements (covering three orders of magnitude in dose rate), source-position triangulation, and dwell time assessment in high dose rate (HDR) brachytherapy.

Methods: A previously characterized and optimized three-point sensor system was used for HDR brachytherapy measurements. The detector was composed of three scintillators: BCF60, BCF12, and BCF10. Scintillation light was transmitted through a single 1-mm-diameter clear optical fibre and read by a compact assembly of photomultiplier tubes (PMTs). Each component was numerically optimized to allow for signal deconvolution using a multispectral approach, taking care of the Cerenkov stem effect as well as extracting the dose from each scintillator. The PMTs were read simultaneously using a data acquisition board at a rate of 100 KHz and controlled with in-house software based on Python. An ^{192}Ir source (Flexitron, Elekta-Brachy) was remotely controlled and sent to various positions in a in-house PMMA holder, ensuring 0.1 mm positional accuracy. Dose measurements covering a range of 10 cm of source movement were carried out according to TG-43 U1 recommendations. Water measurements were performed in order to: (1) characterize the system's response in terms of angular dependence; (2) obtain the relative contribution of positioning and measurement uncertainties to the total system uncertainty; (3) assess the system's temporal resolution; and (4) track the source position in real time. The triangulation principle was applied to report the source position in three-dimensional space.

Results: As expected, the positioning uncertainty dominated close to the source, whereas the measurement uncertainty dominated at larger distances. A maximum measurement uncertainty of 17 % was observed for the BCF60 scintillator at 10 cm from the source. Based on the uncertainty chain, the best compromises between positioning and measurement uncertainties were reached at 17.2 mm, 17.4 mm, and 17.5 mm for the BCF10, BCF12, and BCF60 scintillators, respectively, which also corresponded to the recommended optimal distances to the source for calibration purposes. The detector further exhibited no angular dependence.

All dose values were found to be within 2% of the dose value at 90°. In the experiments performed for source-position determination, the system provided an average location with a standard deviation under 1.7 mm. The maximum observed differences between measured and expected values were 1.82 mm and 1.8 mm in the x- and z-directions, respectively. Deviations between the mPSD measurements and expected TG-43 values were below 5% in all the explored measurement conditions. With regard to dwell time measurement accuracy, the maximum deviation observed at all distances was 0.56 ± 0.25 s, with a weighted average of the three scintillators below 0.33 ±0.37 s at all distances covered in this study.

Conclusions: Real-time HDR brachytherapy measurements were performed with an optimized mPSD system. The performance of the system demonstrated that it could be used for simultaneous, in vivo, real-time reporting of dose, dwell time, and source position during HDR brachytherapy.

3.3 Introduction

High dose rate (HDR) brachytherapy is a radiation therapy procedure in which the high intensity stepping source dynamically moves along pre-determined trajectories through the implant, sequentially treating the target volume. As a result, high dose rates are instantaneously generated around the source with a gradient field of 20%/mm or more for the first centimeter. Owing to these high dose gradients, small uncertainties could result in significant dose variations. Thus, if small errors take place during the treatment and are not immediately detected, harmful consequences and secondary radiation effects may occur. If detected at all, these errors are typically only identified after treatment because of the limited availability of commercial real-time treatment-monitoring systems. Afterloader safety systems can identify dose delivery errors that originate from mechanical obstruction of the source and improper guide-tube connections. However, incorrectly specified source strengths or erroneous swap of treatment catheters can go unnoticed [40, 50].

Routine in vivo dosimetry can be a powerful tool to determine whether deviations from the treatment plan occur during treatment delivery. In vivo dosimetry provides direct information about the level of agreement between planned and measured doses in or near the tumor region. However, it requires a radiation detection system capable of measuring the cumulative dose or dose rate with good sensitivity, precision, and accuracy. Different types of detectors have been studied for in vivo dosimetry applications in brachytherapy [95–97]. A review by Tanderup *et al.* [7] highlighted the main aspects of various detectors that could be used as in vivo dosimeters in brachytherapy. One such detector, the plastic scintillation detector (PSD), has several advantages that have been recently highlighted in the literature, a key one being their real-time response [15–17, 19, 20, 26–28, 30, 75]. Although PSDs are affected by the stem effect

and temperature variations [26], several investigations have developed methods to correct both of these dependencies in the detector response [16, 17, 20, 27, 32, 35–37].

Most of the studies characterizing PSD response were conducted using an optical fibre connected to a single point of measurement as a sensitive volume. However, studies have also demonstrated the feasibility of using multiple scintillation detectors (mPSDs) attached to a single optical chain [31, 32]. A study done by Linares Rosales et *al.* [30] characterized the response of an mPSD system for application to HDR brachytherapy; the authors demonstrated that with proper optimization of the signal collection chain, this mPSD system is accurate within clinically relevant distances from the source. Additionally, previous work explored the source-tracking capacity of different detectors in HDR brachytherapy [9–14]. Some studies used an array of dosimeters placed on the patient's skin, and others a flat-panel detector. In a study of source-position tracking with a single-point detector in HDR brachytherapy, Johansen *et al.* [10] used the dose values from the treatment planning system to develop a method to determine average source shifts within catheters. They used a model based on TG43-U1 to minimize the chi-square between the measured dwell position and the expected one. Besides the aforementioned, brachytherapy clinics do not verify their treatments in real time. The available real time systems present small signal-to-noise ratios, limited time resolution, large measurements uncertainties and can detect only errors in the order of 20% or more [98]. The current study presents the dosimetric performance of a previously optimized and characterized mPSD system [30] in the context of in vivo dosimetry for HDR brachytherapy. Through in-water dose measurements, we: (1) evaluated the angular response of the dosimeter; (2) determined the relative contribution of positioning and measurement uncertainties to the total uncertainty chain; (3) assessed the capacity of the system to measure individual dwell times; and (4) tracked the source position in real time.

3.4 Materials and Methods

The system previously reported by Linares Rosales et *al.* [30] is here modified and tested for application to HDR brachytherapy. The first part of this paper is related to testing the improvement in performance owing to the modification. Then a source tracking and a dwell time study was conducted through in-water measurements with an HDR source of ^{192}Ir.

3.4.1 A mPSD system components

The scintillation light is generated in a three-point PSD and detected through photomultiplier tubes (PMTs) coupled to a set of dichroic mirrors and filters, resulting in a combination that allows for the deconvolution of scintillation light into different spectral bands. Figure 3.1

shows a schematic of the dosimetry system used in this study, which is similar to the system reported by Linares Rosales et *al.* [30]. The cross-hatched components in figure 3.1 represent the components that were also used in that system. The sensitive volumes on the 1 mm diameter mPSD are the BCF10, BCF12, and BCF60 scintillators from Saint Gobain Crystals (Hiram, Ohio, USA), with lengths of 3 mm, 6 mm, and 7 mm respectively. A clear optical fibre type *Eska GH-4001* from Mitsubishi Rayon Co., Ltd. (Tokyo, Japan) was used in guiding the light to the photodetector. Additionally, 1 cm of the clear optical fibre was used in between the scintillators. Most of the components in the light detection system are from Hamamatsu (Bridgewater, USA) [89]. Each assembly, composed of a dichroic mirror, filter, and PMT, is referred as a channel (CH). According to the hyperspectral filtering technique proposed by Archambault et al. [32], the number of channels to be used depends on the number of scintillator points N composing the mPSD, and equals $N + 1$. The additional channel is used to take into account the stem effect, which must be removed from the measured signal [22]. As shown in figure 3.1 the number of channels in the system equals 4 and were assembled as follows: (1) A10034-01, A10033-04, H10722-210; (2) A10034-02, A10033-01, H10722-020; (3) A10034-05, FN (Neutral filter with 100 % of light transmission), H10722-210; (4) A10034-05, A10033-71, H10722-020.

A few key changes were made to the system reported by Linares Rosales et *al.* [30] to improve its performance and obtain higher overall light-collection efficiency. First, a filter with a transmission spectrum in the range of 475 to 600 nm was added to the mPSD after the BCF60 scintillator because a measured residual angular effect came from cross-excitation of the BCF10 and BCF12 scintillators. This effect is characterized in Section 3.5.3. The chosen filter was the Lee filter #121 from PNTA (Seattle, WA, USA). The coupling technique used for detector construction was previously described by Ayotte et *al.* [88]. Second, a beam aligner block (BA; module A10760 from Hamamatsu, Bridgewater, NJ, USA) [89] was included at the entrance of the light-collection system, coupled to an Olympus infinity-corrected objective lens (OL; RMS40X from Thorlabs, Newton, NJ, USA). Note that the filter in CH-4 is also different from that initially recommended by Linares Rosales et *al.* [30]. Section 3.4.2 describes the experiments performed to evaluate the impact of these new components on the light-collection efficiency.

The detector was made light-tight to avoid environmental light contribution and physical damage. The mPSD's 1-mm inner diameter allowed its insertion into a 30-cm needle set from Best Medical International (Springfield, VA, USA), which was used during measurements. Furthermore, all the components were enclosed in a custom-made black box to exclude external light.

A data acquisition board (DAQ NI USB-6289 M Series Multifunction I/O Device from National Instruments, Austin, TX, USA) [90] read the signal produced in each channel at a rate of 100 kHz and sent it to a computer (Apple MacBook Pro, 2.9 GHz Intel Core i5). The light-

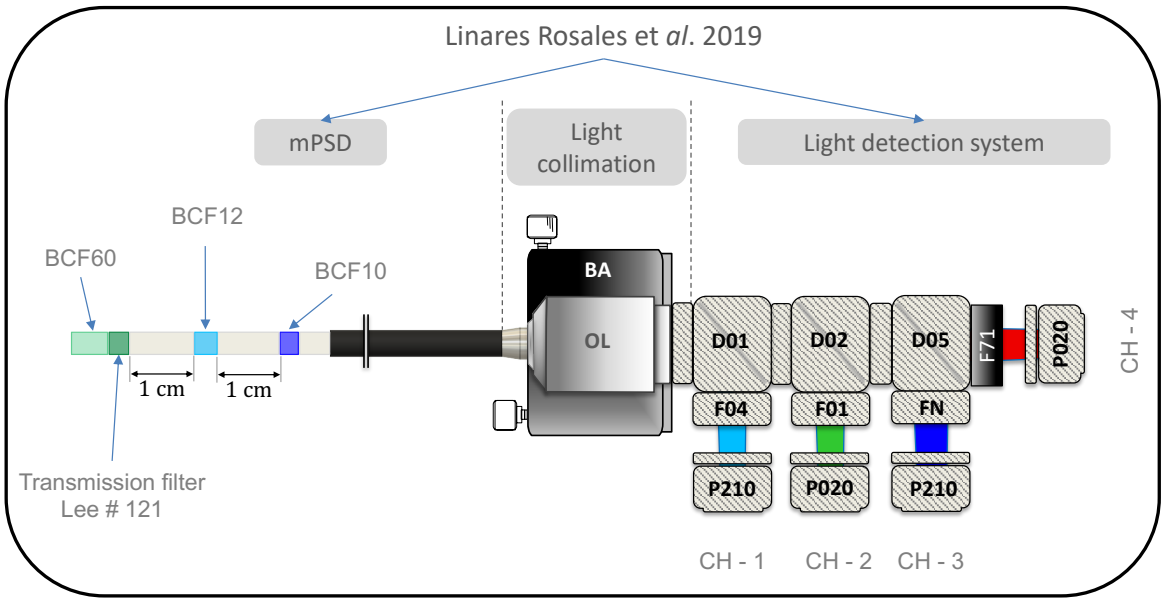

Figure 3.1 – Schematic of the dosimetry system used for HDR brachytherapy dose measurements. The cross-hatched components represent similarities with the system reported by Linares Rosales et *al.* [30]. A green transmission filter is now placed after the BCF60 PSD to avoid cross-excitation from the BCF10 and BCF12 PSDs. Most of the components used in the light detection system were from Hamamatsu. D indicates dichroic mirrors from series A10034, F indicates filters from series A10033, and P210 and P020 refer to PMTs H10722 210 and 020, respectively. CH indicates measurement channels. FN refers to a filter that transmits 100% of the incoming light to the photodetector in the wavelength range of 300 to 500 nm, with F71 being a new component. BA refers to an added beam aligner block A10760 from Hamamatsu, that includes an Olympus infinity-corrected objective lens (OL), model RMS40X from Thorlabs.

detection system was controlled independently from the irradiation unit with in-house software based on Python.

3.4.2 Performance of light collection apparatus

Figure 3.2 shows a schematic of the experimental set-up used to evaluate the effect of using the BA block and the A10033-71 filter. The shaded components in figure 3.2 highlight the changes introduced in the dosimetry system used in this study from that used by Linares Rosales et *al.* [30]. A white light source (model HL-2000 from Ocean Optics, Dunedin, USA) was fixed at one end of a clear optical fiber (Eska GH-4001 from Mitsubishi Rayon Co., Ltd., Tokyo, Japan), while the other end was connected to the system entrance interface. The connection between the fiber and the first channel was named the "entrance interface" to highlight that two types of components were used in that space: (a) a subminiature version SMA adaptor like that used by Linares Rosales [30] and (b) the BA block. As shown in Figure 3.2 , the light passes

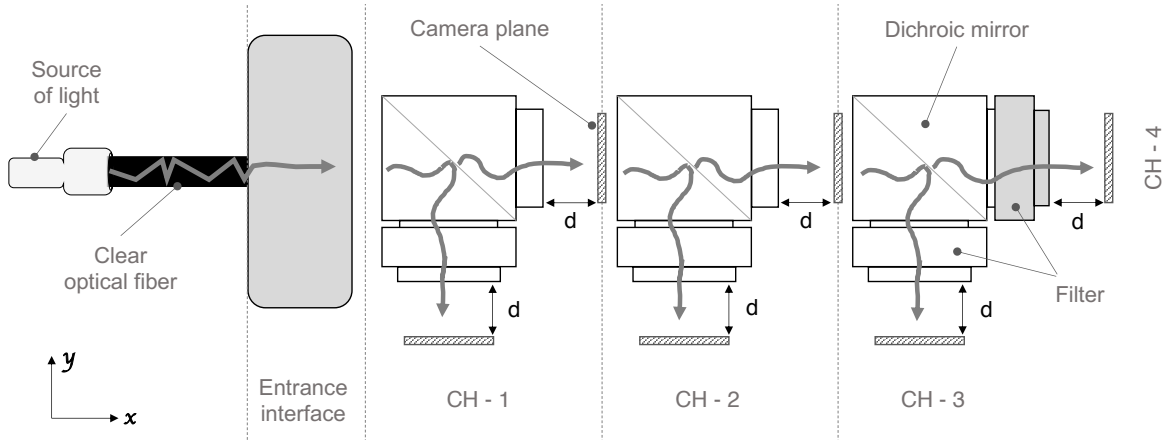

Figure 3.2 – Schematic of the experimental set-up used to evaluate the light-collection efficiency at each step. The shaded regions are the major component changes introduced in this dosimetry system. The entrance interface is the region where the connection between the fiber and the first channel takes place. The narrow cross-hatched horizontal and vertical rectangles represent the plane where the camera was positioned for measurements. CH are the same as in Figure 3.1.

through the entrance interface and strikes a dichroic mirror. Depending on the properties of the dichroic mirror, some of the incoming light is transmitted in the x-direction, while the reflected light goes in the y-direction, passing through a bandpass filter. The transmitted light then reaches a second and a third dichroic mirror, each with different reflection and transmission properties. The amount of light being transmitted or reflected was quantified in every interface. Thus, we were able to characterize both the light-collection efficiency at each plane (cross-hatched rectangles in figure 3.2) and the divergence of the scintillation light beam as a function of distance to each CH. For this analysis, we replaced the PMTs from the original system with a charge-coupled device camera (Alta U2000, Apogee, Roseville, CA, USA). Each channel's output was set at a fixed distance, d, of 80 cm from the camera. Ten images were acquired in two planes for each CH module, as shown in Figure 3.2, and the background signal was subtracted.

To characterize the scintillation light divergence, we used as criteria the full width at half maximum (FWHM) on the light intensity profile taken at various image planes as indicated by the horizontal and vertical cross-hatched narrow rectangles in figure 3.2. For each one of the images collected, a line profile in the center of the image was selected. Finally, the light-collection efficiency was evaluated by extracting the image's average pixel value in the profile's plateau. The system developed by Linares Rosales et al. [30] without any modifications was the reference system for the quantification of the signal-collection efficiency. Two tests were done to perform this quantification. In Test #1, we solely evaluated the effect of using the BA block at the entrance interface, without any further modification to the Linares Rosales system. Test #2 evaluated the impact of the A10033-71 filter on the light collected in CH-4.

The BA block was used in the entrance interface.

3.4.3 HDR brachytherapy irradiation unit

Dose measurements were carried out using a Flexitron HDR afterloader from Elekta (Elekta Brachy, Veenendaal, The Netherlands). The cylindrical ^{192}Ir source pellet was 0.6 mm in diameter and 3.5 mm in length and was housed inside a stainless steel capsule of 0.86 mm diameter and 4.6 mm length. The source air-kerma strength (Sk) was 43810 U. The HDR brachytherapy unit was remotely controlled and able to move the source to the desired position in a water tank by means of a 30-cm needle set from Best Medical International (Springfield, VA, USA). The mPSD was inserted into an additional catheter for dose measurements.

3.4.4 System calibration, dose measurements and Cerenkov removal

Dose values were recorded in real time by the mPSD under full TG-43 U1 conditions [46]. The treatment catheters, as well as the catheter devoted to the mPSD, were inserted in a custom-made poly(methyl methacrylate) holder composed of two catheter insertion templates of 12 x 12 cm^2, separated by 20 cm [9, 30]. This holder was placed inside a 40 x 40 x 40 cm^3 water tank to mimic TG43 U1 conditions for a high energy source (i.e. 20 cm of water past the last measurement position [99]), allowing for source-to-detector parallel displacement with 0.1-mm positioning accuracy. As the water tank only ensures 20 cm of water at the center,we added to the tank faces 10 cm of water-equivalent plastic slabs model Plastic Water Standard (CIRS, Virginia, USA). All measurements were repeated at least five times, and the set-up was completely disassembled and reassembled between measurements. The mathematical formalism proposed by Archambault et al. [32] was used to remove the stem signal. The calibration matrix and dose values were calculated according to the formulation published by Linares-Rosales et *al.* [30] for a 3-points mPSD configuration. Calculations were done with a coordinate system, where the radial direction to the source was represented as x and the longitudinal direction as z. Calibrations and measurements were carried out under the same experimental conditions. During the calibration process, measurements were performed with the ^{192}Ir source dwelling inside the catheters with a 1-mm step, and the detector positioned at a known x-distance from the measurement catheter. Thus, the source dwell position, where the maximal signal was produced, was related to each sensor $z = 0$ coordinate. Therefore, the relationship between the produced signal and the TG-43 dose was derived, being the calibration matrix independent of detector positioning errors. The absorbed dose deviations for the mPSD were evaluated using the dose predicted by the TG-43 U1 formalism [46] as the reference. Dose values provided by the scintillators were integrated over the scintillator volume to account for their finite size.

3.4.5 Relative contribution of the positioning and the measurement uncertainties

The proper selection of calibration conditions is important for measurements of detector response and performance: agreement with the TG-43 U1 expected dose, angular dependence, and signal-to-noise ratio. The selection of the calibration distance was a compromise between measurement and positioning uncertainties. Andersen *et al.* in 2009 [8] showed that positioning uncertainty dominates in measurements made close to the source, whereas measurement uncertainty dominates at large distances. We performed an uncertainty analysis similar to the one described by Andersen et *al.* [8] to select the most effective calibration distance for the mPSD.

Dose as a function of distance to the source as predicted by TG-43 U1 for each scintillator constituted the reference dose. The uncertainty associated with the reference dose was obtained by calculating the dose gradient per millimeter. This uncertainty is represented as U_{TPS}. Dose measurements were associated with a standard uncertainty called U_M. We estimated U_M by taking 10 different measurements, each one with a dwell time of 30 s per source position. The signal collected is averaged over a 1 s interval. Thus, at each explored source dwell position, U_M was determined using a sample of 300 measurements. Knowing the relative contribution of the positioning uncertainty U_{TPS} and the measurement uncertainty U_M , we were able to estimate the combined uncertainty U_C associated with each scintillator as a function of the source-to-detector distance. The point where the combined overall uncertainty was the smallest is called in this paper the "sweet spot" and was the distance chosen for each independent scintillator's calibration.

3.4.6 Angular dependence

We next explored the variation in the mPSD's response as a function of variation in the angle to the HDR brachytherapy source. Because the shape of the scintillators used was cylindrical, no axial angle dependence was expected, but longitudinal angle dependence was possible.

Precise detector positioning is key when evaluating a detector's angular response. In this work, the scintillation detector was precisely positioned by using a in-house template, as shown in Figure 3.3. It consisted of a solid-water slab of $30 \times 30 \times 1\ cm^3$, model Plastic Water Standard (CIRS, Virginia, USA). The source catheter lay in a groove in the template slab. The groove on the water slab was done using the Fadal 88 (Vendor, City, Country) Computer Numerically Controlled (CNC) machine. The piece manufacturing was done with a precision of 0.04 mm. The groove radius was 4 cm, allowing for a 270° source-rotation angle around the mPSD. The source was sent to each specific position using a flexible catheter (LumenCare Azure 5F (Nucletron, Veenendaal, The Netherlands). Twelve source dwell positions were planned, with

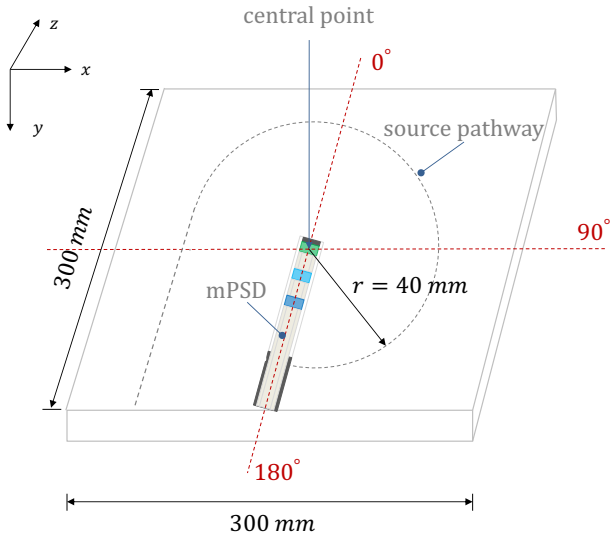

Figure 3.3 – Schematic representation of the template used for mPSD angular dependence analysis.

a dwell time of 20 s each. The slab was submerged in a 40 × 40 × 40 cm^3 water tank. To confirm the source position, we performed initial irradiations with an EBT3 film. The angular dependence study was conducted by placing the sensor at the center of the template (see figure 3.3). Repeated irradiations were performed keeping all other variables fixed. To evaluate the effect of adding a green filter to the BCF60 scintillator (see Figure 3.6) , two mPSDs were used: (1) an mPSD assembly with a green filter coupled to BCF60, as shown in Figure 3.1; and (2) an mPSD assembly with no filter but with the exact same physical characteristics. Each measurement was acquired five times, and the set-up was completely unmounted between measurements. In addition, the same procedure was repeated on three different days.

3.4.7 ^{192}Ir source tracking

We then evaluated the mPSD system's ability to report the position of the source in three-dimensional space. This study was done with a calibrated mPSD system under full TG-43 U1 conditions [46]. For each dwell position, the dose measured by the mPSD's sensors was independently extracted according to the hyperspectral formalism published for a 3 points mPSD [30,32]. The mean dose value as well as its standard deviation were calculated based on the dose recorded during the dwell. The direct relationship between the dose and the distance to the ^{192}Ir source was used to build the dose-to-distance response function ($r_i = f(dose)$) for each scintillator i. In the same manner, the standard deviation of the mean dose was transformed into an uncertainty in the distance σ_{r_i}. Thus, for a given dwell position, the collected signal is transformed into $r_i \pm \sigma_{r_i}$.

Since: (1) the mPSD orientation is defined by the catheter (here it is a straight path) and (2) the distance between each individual scintillator is known, then the radial distance r_i between each scintillator and the source can be determined and the source position relative to the mPSD calculated. By combining all of the above, we applied the triangulation principle to estimate the (x_j, z_j) source coordinates in the plane. As the mPSD is composed of 3 scintillators, 3 pairs j of source coordinates were determined for each dwell position. The overall source position in space $(\overline{x}, \overline{z})$ was determined through a weighted average calculation, as shown in equations 3.1 and 3.2. In equations 3.1 and 3.2 σ_j refers to the combined standard deviation of the uncertainties in the distance σ_{r_i}.

$$\overline{x} = \frac{\sum_{j=1}^{3} \frac{x_j}{\sigma_j^2}}{\sum_{j=1}^{3} \frac{1}{\sigma_j^2}} \tag{3.1}$$

$$\overline{z} = \frac{\sum_{j=1}^{3} \frac{z_j}{\sigma_j^2}}{\sum_{j=1}^{3} \frac{1}{\sigma_j^2}} \tag{3.2}$$

In a cylindrical coordinate system, only (r,z) are extracted with the mPSD and there is a degenerescence in ϕ. It means that in a 3D space, it is not possible to distinguish the x and the y coordinates of the source (assuming a coordinate system where x and y represent the radial direction, and z the depth). For a given dwell position, the distances provided by the mPSD lead to a circle around it (a position along the catheter (z) combined with a distance radially away from the mPSD (xy). Thus, for simplicity, in this paper, the x or y coordinate is not independently accounted for. Note however, that in brachytherapy, this degenerescence is severely constrained since the source can only travel inside applicator channels (catheters, needles and so on) and those channels must be reconstructed before treatment planning.

Real-time measurements were performed with the source and detector isotropically covered by at least 20 cm of water to ensure a full scatter condition, as required by the TG-43 U1 formalism [46]. The custom-made poly(methyl methacrylate) holder was used for catheters positioning. Figure 3.4 is a schematic representation of the plans created to track the source position. Nine needles were used to send the source to the desired position. The numbers at the top of Figure 3.4 are the catheter numbers, while those at the bottom indicate the distance from the source to the mPSD.

Two irradiation plans were created to test the ability of the system to track the source position.In Plan 1, the source dwelled only inside Catheter 1, with a 1-mm step between each

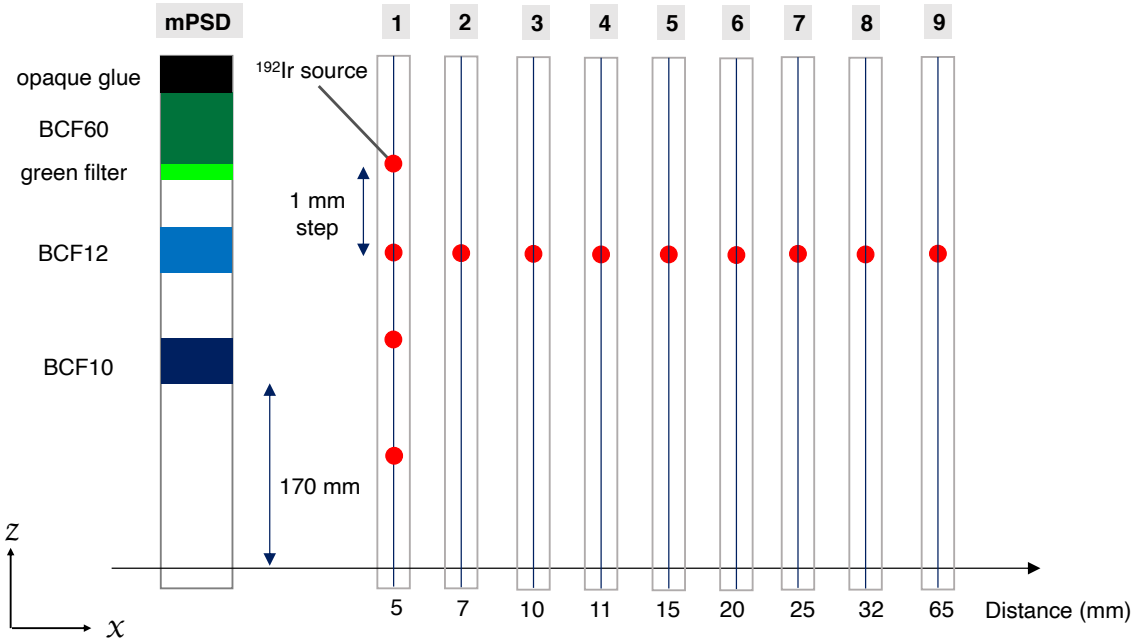

Figure 3.4 – Schematic of the nine catheters and source positions used for source positioning tracking with the mPSD.

dwell position. In total, the plan had 101 dwell positions with a dwell time of 10 s each. In Plan 2, the HDR source dwelled inside Catheters 1 through 9, but only once per catheter. As in Plan 1, a dwell time of 10 s per source position was planned. Our reasoning for plan 2 to only consist of one dwell per catheter vs. plan 1, was to explore the source tracking accuracy while the source moved along each axis independently. With Plan 1 and 2, we covered up to 10 cm range of source movement in a 3D space, which according to the scintillators' location, allowed for a 0.5-6 cm measurement range with BCF10, 0.5-5.7 cm with BCF12 and 0.5-7.5 with BCF60. Both Plans 1 and 2 were delivered seven times each.

3.4.8 Planned vs. mPSD's measured dwell time

We further evaluated the ability of the real-time mPSD measurements to extract dwell times under various irradiation conditions. Seven irradiation plans were created, and all the parameters of the plan were fixed except the dwell time. In all cases, the source dwelled inside Catheter 1 (Plan 1, Figure 3.4) with a 1-mm step between each position. The dwell times used were 1, 2, 3, 4, 5, 10, and 20 s.

The sequence of planned dwell positions associated with the planned dwell times produced a step-like dose curve for each scintillator in the mPSD. The dwell times were extracted from measurements by detecting the edges of the dose's pulse. For the signal pulse produced

Table 3.1 – Results of the analysis of the beam aligner (BA) block's effect on the dosimetry system. μ_s refers to the mean signal obtained in the profile's plateau, and σ its associated standard deviation. μ_s values are normalized to the image μ_s obtained at the entrance interface's output.

	Normalized signal intensity ($\mu_s \pm \sigma$)			**FWHM (mm)**	
Location	**Ref. System**	**Test #1**	**Gain**	**Ref. System**	**Test #1**
Entrance interface	0.510 ± 0.11	0.88 ± 0.08	1.73	4.81	4
CH - 1 x	0.421 ± 0.09	0.760 ± 0.10	1.79	4.81	4
CH - 1 y	0.118 ± 0.19	0.180 ± 0.01	1.53	4.46	4.1
CH - 2 x	0.092 ±0.15	0.300 ± 0.12	3.26	4.65	4.1
CH - 2 y	0.020 ± 0.18	0.084 ± 0.14	4.19	4.27	4
CH - 3	0.002 ± 0.12	0.010 ± 0.12	4.60	4.21	4
CH - 4	0.040 ± 0.14	0.068 ± 0.13	1.70	4.23	4.21

FWHM: Full width at half-maximum, CH: Channel

at a planned dwell position (dp), dwell times were extracted from measurements using the following parameters [30]: (a) mean signal (μ_s); (b) mean background signal (μ_b); (c) signal standard deviation (σ_s); and (d) background standard deviation (σ_b). To properly differentiate the signal from the background, a minimum *Signal to background ratio (SBR)* of two was considered. Thus, an active dwell position was considered when $\mu_s \pm \sigma_s \geq 2\mu_b \pm \sigma_b$. To distinguish the signal from one dwell position dp_N from that of the subsequent one dp_{N+1}, we considered as a discriminator the relationship $(\mu_{s,dp_N} \pm \sigma_{s,dp_N}) \neq (\mu_{s,dp_{N+1}} \pm \sigma_{s,dp_{N+1}})$. Once the dwell position dp_N from the whole collected signal was isolated, the measured elapsed time was quantified. Discrepancies in dwell time measurements were evaluated using the planned dwell times as references.

3.5 Results

3.5.1 Improved light collection efficiency

Table 3.1 summarizes the results obtained from our experiment investigating the impact of the BA block on the efficiency of signal collection. The first column in Table 3.1 shows the location where the images were acquired according to the schematic shown in Figure 3.2. Columns 2 and 3 show the mean signal intensity (μ_s) obtained in the profile's plateau region as well as its associated standard deviation σ. The μ_s values were normalized to the image μ_s value obtained at the fiber's output. Column 4 shows the gain factor at each interface. Columns 5 and 6 show the profile's FWHM obtained for the reference system and Test # 1, respectively. The results from Test # 2 are not shown in Table 3.1 because changing the filter in CH-4 only influenced the light collected in that channel.

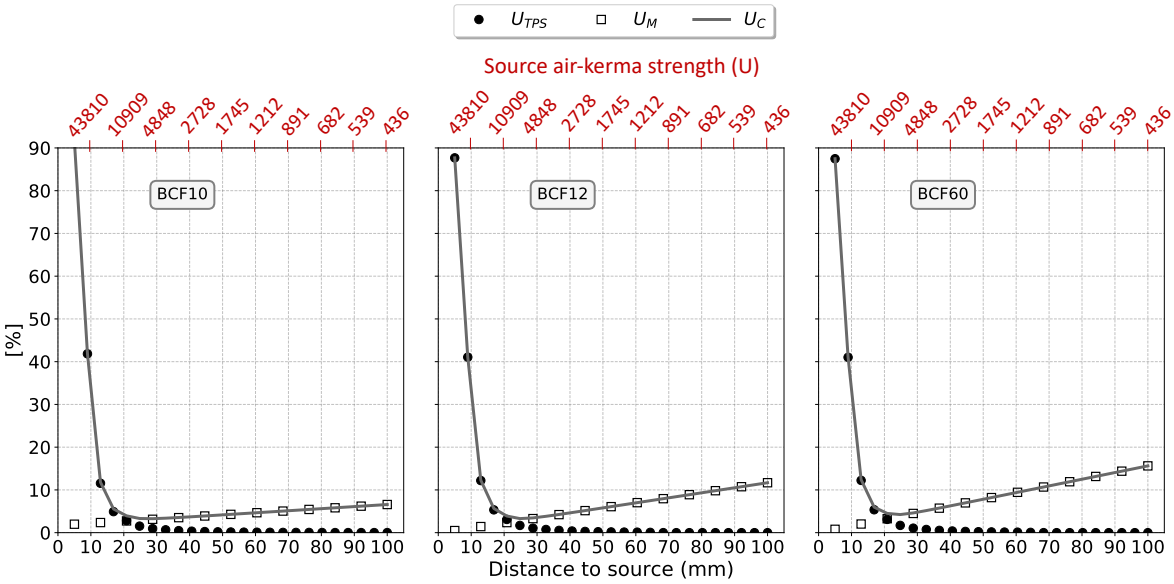

Figure 3.5 – Contribution of the measurement and positioning uncertainties to the mPSD response in HDR brachytherapy. The uncertainty values are relative to the dose at the given depth. U_c is the combination of the TG-43 dose gradient uncertainty (U_{TPS}) and the measurements uncertainty (U_M).

Table 3.2 – Recommended distance to source for mPSD calibration for HDR brachytherapy.

	Sweet-spot	
Scintillator	**Distance (mm)**	U_c (%)
BCF10	17.2	3.8
BCF12	17.4	3.6
BCF60	17.5	4.3

3.5.2 Contribution to the uncertainty chain

Figure 3.5 shows the relative contribution of detector position uncertainty (U_{TPS}) and measurement uncertainty (U_M) as a function of source-to-detector distance for all three scintillators. The bottom of the x-axis expresses the distance to the source. The top x-axis translates the distances to the source (dose rates) to a source air-kerma strength equivalence. Table 3.2 shows the sweet-spot values associated with each scintillator in the mPSD. The maximum U_M observed was 17 % for the BCF60 at 100 mm from the source. U_M values for BCF10 and BCF12 were always under 13% at all the distances tested.

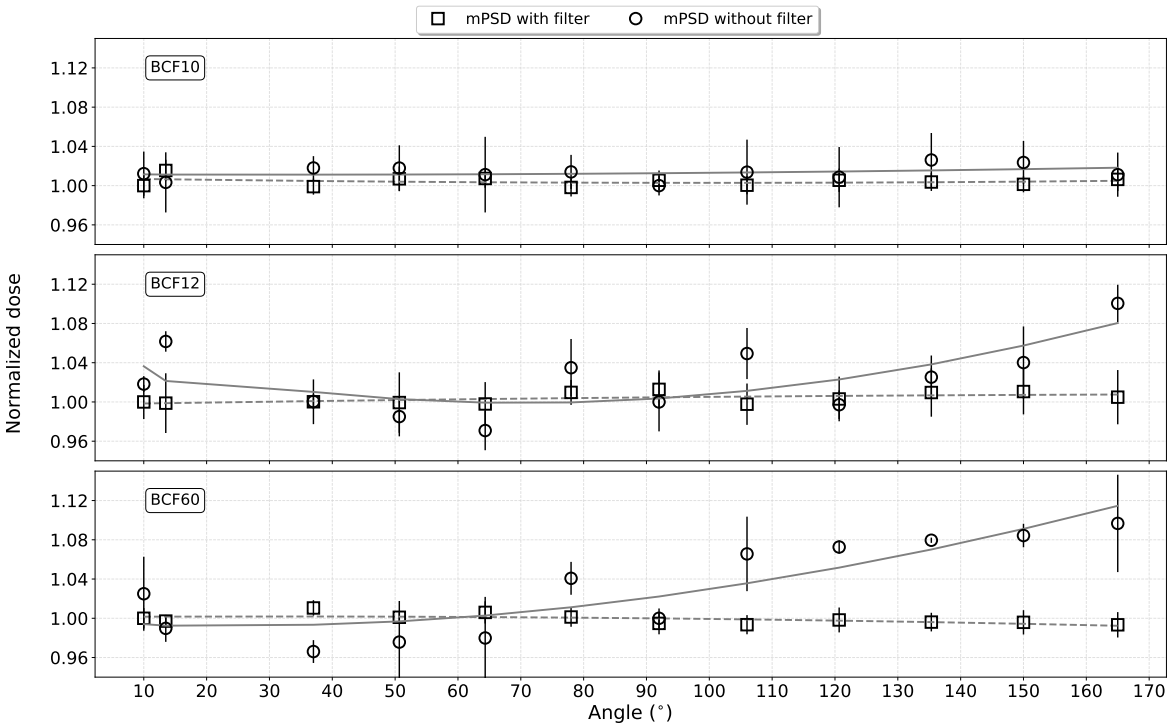

Figure 3.6 – The mPSD's response as a function of angle to the HDR brachytherapy source. Dose values are normalized to 90°. Bars represent standard deviations. Dotted lines are the trends in the mPSD's response.

3.5.3 Angular dependence

Figure 3.6 depicts the angular dependence of the mPSD system with and without the use of a bandpass filter coupled to the BCF60 scintillator. The solid and dotted lines represent the trendlines of each detector's response. The dose values in Figure 3.6 are normalized to each scintillator's response at 90°. The results for BCF10 evidenced an agreement with the TG-43 U1 expected dose within 2 % in all the angles explored. In the case of the scintillators BCF12 and BCF60 without filter, deviations of 10 % are observed at angles beyond 90 °. However, when a filter is used the agreement is within 2 % as in BCF10.

3.5.4 Source position tracking

Absorbed dose measurements

The violin plots [100] in Figure 3.7 show the density distributions of the relative differences between each scintillator's measured dose and the dose calculated by TG-43 during irradiations with Plans 1 and 2. The inner boxes represent the interquartile ranges, and the white dots inside the boxes indicate the median values. The scintillators' measured doses did not deviate

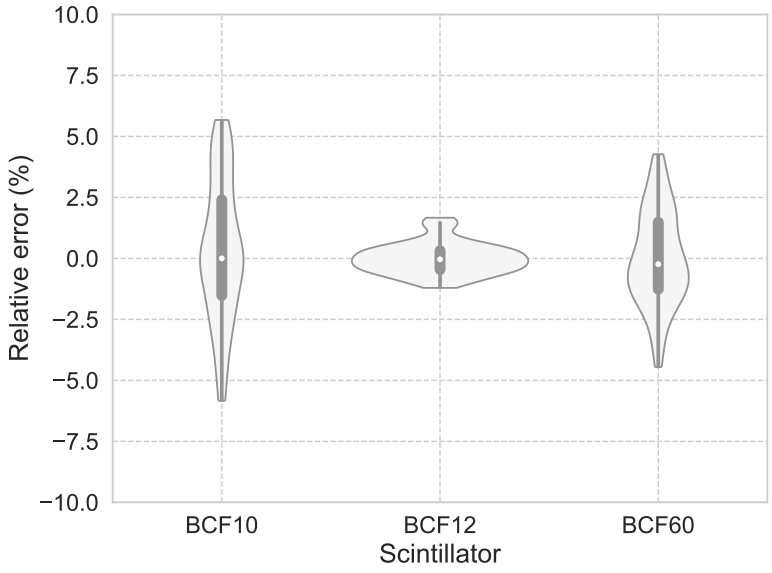

Figure 3.7 – Density distribution of the relative errors between the scintillators' measured doses and TG-43 during source-tracking analysis for HDR brachytherapy. Boxes represent interquartile ranges (quartile 1 and quartile 3), and the white dots inside the boxes represent the median values. The inner vertical lines extend from each quartile to the minimum or maximum.

by more than 5% from the TG-43 predicted dose. The median values were close to 0, as seen from the distributions displayed by the envelop of the violin plots. BCF12, the middle sensor, had the least dispersion, with an interquartile range within 1% of the deviations. The interquartile range in BCF10 was found within 2.5 % of the deviations, while in BCF60, within 2.2 %.

Source-position determination

Figure 3.8 presents the determination of the source position by triangulation [101]. The origin of coordinates for source position calculation was considered at the center of BCF10. The upper-left side in figure 3.8 shows the axis convention used for calculations, the mPSD's orientation and the scintillators' effective position in the z-axis. Figures 3.8a, 3.8b, and 3.8c illustrate the results obtained during irradiations with Plan 1, while the results for Plan 2 are shown in figures 3.8d, 3.8e, and 3.8f. Figures 3.8a and 3.8d illustrate the delivery of Plans 1 and 2, respectively. Figures 3.8b and 3.8e summarize the absolute deviation (in mm) on the x and z axes, between the calculated position of the mPSD and the planned one, for a source moving along the z axis (Plan 1) or along the x axis (Plan 2). Figures 3.8c and 3.8f show the absolute difference between the radial distance to the planned source position and the triangulated one, along the same two axes. The gray vertical lines in Figures 3.8c and 3.8f represent the standard deviation of each triangulated position. The dotted lines in Figures

3.8b, 3.8c, 3.8e, and 3.8f represent the trendlines of the calculated deviations.

The radial distance to the source was defined as the distance from each scintillator's effective center to the source dwell position. We observed differences above 1 mm in the radial distance prediction at distances past 62 mm for BCF10, 60 mm for BCF12, and 55 mm for BCF60. Results from Plan 1 (Figures 3.8b and 3.8c) demonstrated that when the source dwelled at the extremities of the mPSD, deviations in source reporting could reach a maximum of 1.8 ± 1.6 mm in the x or z axes. The trendlines shown in Figure 3.8b help to visualize this behaviour. However, as depicted in Figures 3.8e and 3.8f, the maximal observed deviation from the planned position for the delivered Plan 2 was always smaller than 0.92 ± 0.5 mm.

3.5.5 Planned vs. measured dwell time

Figure 3.9 shows the deviations between the measured dwell times for our mPSD system and the planned ones as a function of distance to the source. The dotted lines represent the average measurement differences for each individual scintillator, whose positions are represented by squares. The shaded region around the average line shows the standard deviation extracted from all the dwell times measured. Taking as reference a range from −10 to +10 mm around each scintillator's effective position (radially), the average dwell time measured by BCF10 was within 0.03 ± 0.04 s of the planned dwell time, while the BCF12 average response was 0.04 ± 0.04 s, and that of BCF60 was 0.03 ± 0.05 s. The maximum deviation observed at all distances was 0.56 ± 0.25 s for a single scintillator, with a weighted average of the three scintillators below 0.33 ± 0.37s at all distances covered in this study.

3.6 Discussion

3.6.1 Improved light collection efficiency

In this study, we evaluated the influence on the dosimetry system's light collection efficiency of introducing a BA block and replacing a band-pass filter on channel 4. Because of the geometry and light-cone divergence, signal losses were observed in all the channels. Nonetheless, these results demonstrate that the additional optical block helps to collimate the light transmitted through the mPSD's optical fiber and consequently reduce the signal collection losses by a factor of almost 2. Important gains were observed in CH-2's x and y-directions and CH-3, reaching values of 3.26, 4.19, and 4.60, respectively. According to the analysis of the profile's FWHM, the mean FWHM value for the reference system was 4.43 ± 0.24 mm, while in Test #1 it was 4.06 ± 0.08 mm. The change of the filter in CH-4 produced a mean signal of 0.193 ± 0.12, in contrast to the mean signal of 0.068 ± 0.13 obtained in Test #1. A10033-63 and

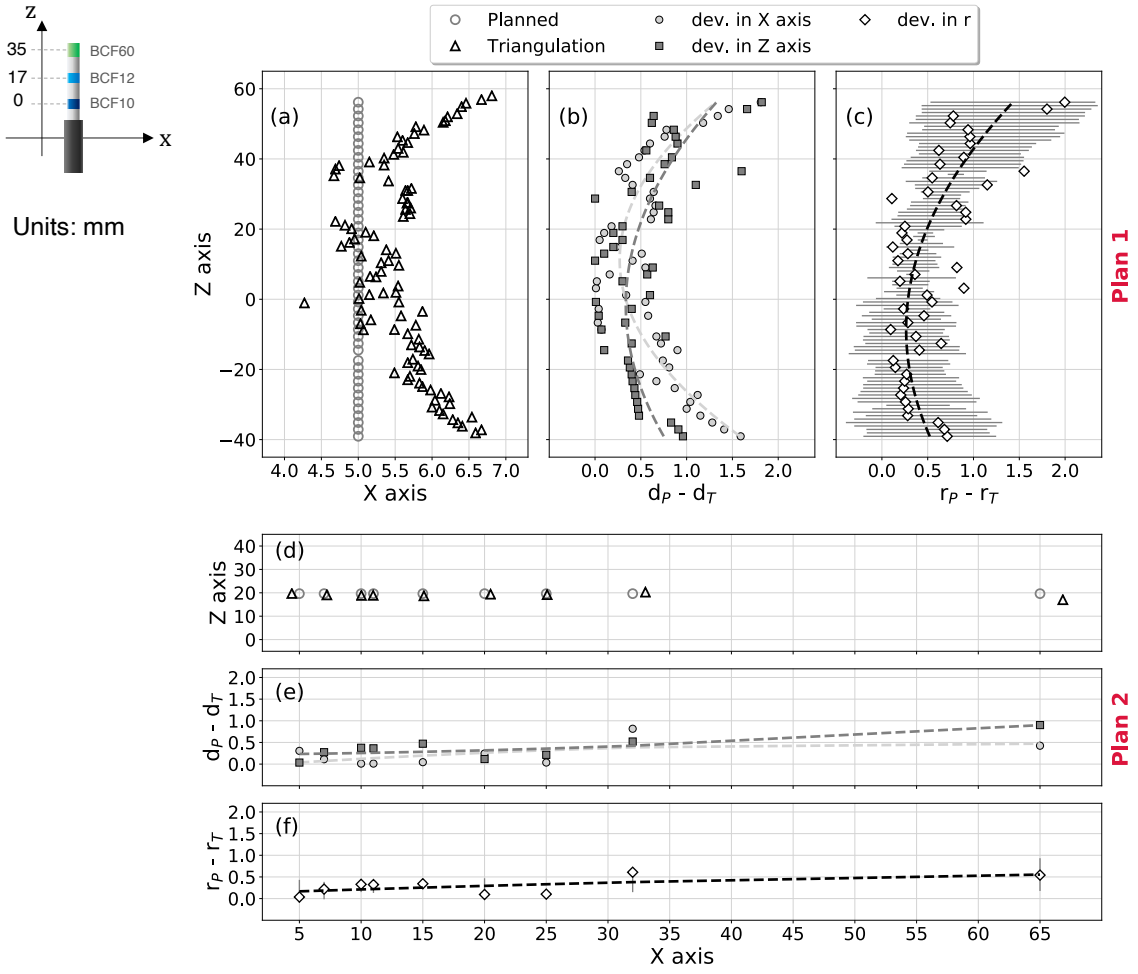

Figure 3.8 – Source-position determination. (a), (b), and (c) illustrate the results for Plan 1. (d), (e), (f) highlight the findings in Plan 2. (a) and (d) illustrate the plans. (b) and (e) show differences (in mm) between the distance from the mPSD to the planned source position and the distance to the triangulated one: (b) for Plan 1, (e) for Plan 2. (c) and (f) show the absolute difference between the radius to the planned position and the radius to the triangulated one for Plan 1 (c) and Plan 2 (f). Dotted lines represent the trendlines of the deviations between the calculated positions and the planned ones. In (c) and (f), the standard deviation of each triangulated position is represented with a gray lines vertical to the radial deviation trendline.

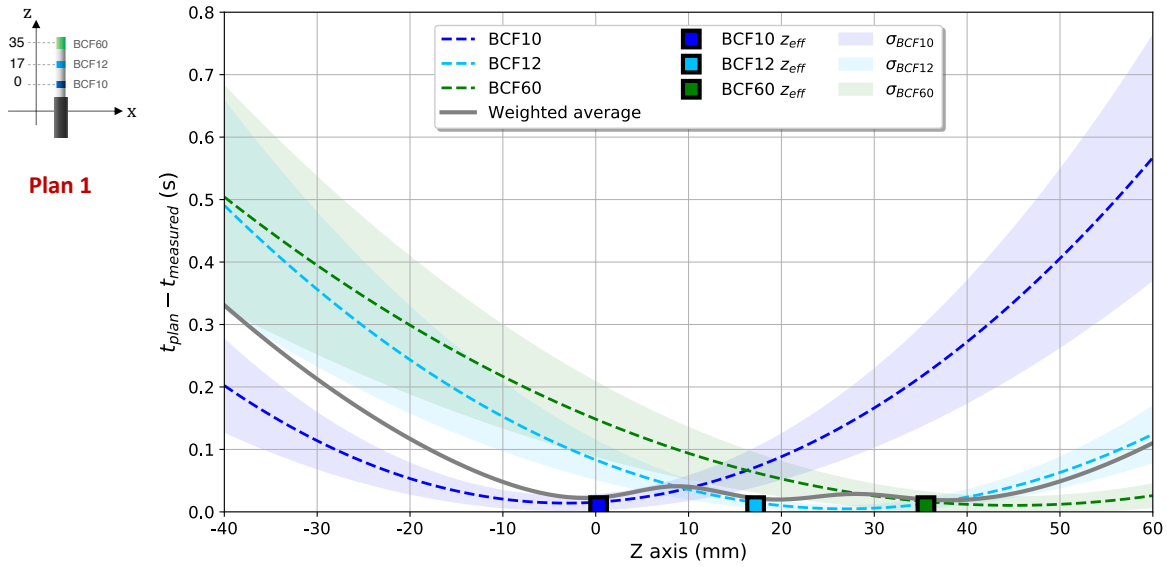

Figure 3.9 – Deviation of mPSD measured dwell times from planned dwell times as a function of distance to the source. Dotted lines represent the average of the scintillators' deviations. The continuous line represents the sensors' weighted average deviation. The shaded region represents the standard deviation. The squares along the bottom correspond to each scintillator's effective position.

A10033-71 are longpass filters with cut-on wavelengths of 600 nm and 510 nm, respectively. Linares Rosales et *al.* [30] showed that in the wavelength range of 510 to 600 nm, there was scintillation light that was not used. Hence, replacing the A10033-63 filter with the A10033-71 filter allowed for additional improvement in the signal-collection efficiency in CH-4.

3.6.2 Contribution to the uncertainty chain

The most appropriate distance for mPSD calibration was found using Figure 3.5 as a metric. A similar study was performed by Andersen *et al.* [8] with an aluminum oxide crystal (Al_2O_3:C) attached to a 1-mm optical fiber reporting a maximum U_M of about 40 % at 50 mm from the source. Even if the light produced by the scintillators in the mPSD was subject to multiple optical filtration, the measurement uncertainty remained low at the longest distances, in comparison with the results reported by Andersen et *al.* [8]. It is important to note that the uncertainty in the expected dose U_{TPS} was solely accounted for by the positioning uncertainty. AAPM Task Group 138 and GEC-ESTRO [102] reported that the expanded relative propagated uncertainty (k = 2 or 95% confidence level) for dose at 1 cm of high-energy brachytherapy sources along their transverse plane was 6.8%. This uncertainty would compound with U_C to complete the error chain. These distances represent the best compromise between mispositioning and measurement uncertainty for the mPSD system under evaluation. Of course, U_C is specific to the detector used in this case, to each sensor of the multipoint dosimeter.

Such analysis should be performed as a standard of practice when reporting the performance of an in vivo dosimeter owing to the strong distance dependence displayed in brachytherapy. On the other hand, it is well known that HDR sources have a wide range of air-kerma strengths in the clinic due to decay, affecting the measurement uncertainty directly. In this study, an independent investigation of the uncertainty as a function of the air-kerma strengths was not done. However, as the distance to the source is directly related to the dose rate, from Figure 3.5, we can infer that if the dose rate decreases, the measurements uncertainty increases. As previously mentioned, U_c is the combination of the TG-43 dose gradient uncertainty (U_{TPS}) and the measurement's uncertainty (U_M). The U_{TPS} behaviour in percentage is invariable in time. Thus changes in S_k solely influence the measurement uncertainty U_M. We hypothesize is that the slope of the U_M increases, especially at long distances from the source with the decreasing of the source air-kerma strength. As a consequence, the sweet-spot shifts slightly (1 - 4 mm) toward shorter distances for the used range of ^{192}Ir's activity in a clinical context.

3.6.3 Angular dependence

Previous studies have analyzed the angular dependence of some plastic scintillators [81, 103–105], but to our knowledge, none have examined a multipoint detector configuration. A study by Archambault et al. [81] on a single-point plastic scintillator dosimeter composed of BCF12 and irradiated using an external beam found no angular dependence in response, with a maximum deviation of 0.6%. They highlighted the importance of employing a stem-effect removal technique to avoid larger deviations caused by angular dependence. Wang et al. [103, 104] also found angular independence for a BCF12 detector, with responses varying by about 2%. Furthermore, the angular independence of a BCF60 detector has been previously established [105]. A study by Lambert et al. [18] recommended the use of plastic scintillator dosimeters with diameter-to-length ratios below 5:1 for brachytherapy purposes; this would ensure detector response variation within 1.5% as a function of angle to the source. The mPSD under evaluation in the present study was composed of 3 mm of BCF10, 6 mm of BCF12, and 7 mm of BCF60. In this context, only the diameter-to-length ratio of BCF10 would fall into the range recommended by Lambert et *al.* [18]. Figure 3.6 shows that as angles went beyond 90°, a clear angular dependence emerged in the BCF12 and BCF60 curves, up to almost +10% when no filter was used. We hypothesized that this effect was due to cross-excitation of the sensors. We tested this hypothesis by using a 400 to 600-nm bandpass filter coupled to the BCF60 sensor, which would be the one producing the least amount of direct scintillation light at large angle (farthest from the source) and thus the most susceptible to excitation by the other two scintillators. After this simple addition to the system, all of the scintillator responses were essentially flat at all angles.

3.6.4 Source position tracking

Minimal dose deviations from the TG-43 U1 expected dose was found in the scintillator BCF12. During measurements, the distance from the BCF12 detector to the source remained relatively constant owing to its central position inside the mPSD, whereas the BCF10 and BCF60 detectors were subject to more extreme distance variations and accordingly exhibited greater dispersion in the difference between measured and expected (TG-43) doses. Nonetheless, for each sensor, 75% of the sample was found to be within a deviation range of 2.5%. The high-dose-gradient field imposed by the ^{192}Ir source at short distances may induce a substantial uncertainty in the dose determination, on the order of 20% per millimeter at 1 cm from the source. That effect was not observed in this study. We explain this result thus: the actual position of each sensor in the mPSD was calibrated initially. Also, the expected dose values used in this study were calculated by considering each scintillator as a volume, not as a single point in space. Such an approach accounts for the fact that the dose gradient is not constant and varies as a function of distance to the source, including inside the scintillator volumes themselves.

The source-position tracking showed that, as the source moved away from each scintillator volume, the scintillators' capacity to report a precise distance to the source decreases, and the source triangulation process became less efficient. This effect is attributed to the increase of the measurement uncertainty in combination with reduced accuracy of the dose prediction models in those measurement conditions. As previously mentioned, we used the hyper-spectral formalism proposed in [30,32] for system calibration and to extract the dose measured by each scintillator independently. This formalism is a linear regression model, which can accurately perform data extrapolation. However, we are trying to predict/fit a dose decay behaviour, which is not linear (as a function of the distance to the source), with a linear model. As a consequence, the fitting process, is more accurate and representative of the data in those situations similar to the calibration conditions (shorter distances to the source). Figure 3.8 provides an idea about the experimental limits of the source tracking with the mPSD. Essentially we can not measure a situation in which we are at 10 cm from the source. For a clinical application, we should ensure a region of application relative to the mPSD position, where most of the dwell positions will be within 6 cm from the mPSD. On the other hand, finding HDR treatments with the ^{192}Ir sources stepping within a range of 6 cm is common in a clinical context, especially for prostate cases. Therriault-Proulx et al. [9] used a multipoint configuration with a single optical fiber as an in vivo verification tool for HDR brachytherapy. Based on a determination of each independent scintillator's offset, they used a weighted approach to report the overall offset between the expected and calculated positions of the ^{192}Ir source. Although this weighted offset improved their source-position detection, offsets greater than 2.5 mm were reported, limiting their HDR brachytherapy measurements to a range within 3 cm of the source. In contrast, the current study demonstrated that an optimized system can

extract source positions with maximal deviations of no more than 1.8 mm for a range up to 10 cm from the source. Johansen et *al.* [10] performed a study of source tracking in a series of prostate HDR treatments with a single point detector composed of a radioluminescent crystal of Al_2O_3:C. The dose rate for each dwell position was used to determine the positions of the individual treatment catheters relative to the dosimeter. They found an average dose agreement with the TG43 U1 expected dose of -4.66 ± 8.40 %. Among the limitations of the study done in [10] we can find that the detector's response to each planned source dwell position leads to a sphere of probable locations around the sensitive volume. Additionally the accurate catheter reconstruction depends on accounting with the information for at least 3 dwell positions. A multipoint system like the one in this paper proposed is advantageous for this kind of situation since the source location is available from the first second the source arrives at the planned location. Besides that, the mPSD under analysis is subjected to degeneration in the detector radial direction. By combining the mPSD's response with another detector, we can eliminate the mPSD's degeneration in the radial direction. There is no restriction about which detector should be used for such a set-up. It has to be explored, but it could be combined with a single point detector, another mPSD or simply with a similar system to the one proposed by Guiral et *al.* [12].

3.6.5 Planned vs. measured dwell time

When the source was moved to larger distances from a given scintillator's effective position, the deviations between the measured and planned dwell times increased accordingly. Evidently, at short distances from the source, the high gradient field characteristic of the ^{192}Ir source allowed to us obtain a sharp pulse of signal and, as a consequence, proper differentiation of the signal from one position to the subsequent one. At long distances, as shown by Andersen et *al.* [8], detectable source displacement is more difficult to obtain for small dwell times owing to the increased measurement uncertainty. The capability of the mPSD system in measuring the source dwell time was evaluated for a range up to 10 cm of source movement around the sensors. The beauty of our mPSD system, is that one or more additional sensors could be placed closer to the source to provide an alternate measurement. In our case, a weighted average over all three scintillators was performed (continuous line in Figure 3.9), resulting in a maximum deviation of 0.33 ± 0.37 s. This level of accuracy is sufficient for clinical validation of individual dwell times for most configurations. Guiral et *al.* [12] conducted a similar study of source dwells time verification in HDR brachytherapy with ^{192}Ir. The system consisted of 4 GaN-based dosimeters, inserted into a gynecological multichannel applicator of 30 mm diameter. The applicator accounted for 9 surface channels, where 1 dosimeter was inserted per surface and five channels were used for treatment delivery. Measurements for dwell time verification in [12] were done for a 24 dwell-position protocol with a 5 s dwell time covering 60 mm of distances to the source. The findings in [12] showed an agreement with the expected

dwell time of 0.05 ± 0.09 s. However, in comparison with the current study, the authors in [12] only explored a dwell time of 5 s, while our analysis included dwell times down to 1 s, for a wider range (100 mm) of source displacement. Having dwell times in the order of 1 s is very common in a clinical practice, hence the importance of understanding what happens for those kinds of situations. Furthermore, the effect of having a 2.5 mm dwell position step in Ref. [12] produces a more pronounced dose gradient between 2 subsequent dwell positions, and as a result, an easier detection. In this study, a 1 mm step between two dwell-position was used.

3.6.6 Perspective and applicability

The optimization and characterization efforts over the dosimetry system has led to a novel platform that comprises 3 parts: 1) a multi-point plastic scintillator dosimeter, 2) a compact assembly of photomultiplier tubes coupled to dichroic mirrors and filters for high-sensitivity scintillation light collection, and more recently 3) a Python-based graphical user interface used for system management, data acquistition and signal processing. A clinical trial is now on going at our institution using the presented characterized system. In this first clinical implementation, we will be looking at the clinical workflow for in vivo dosimetry using this technology and the data will be used to seek optimal action thresholds.

The mPSD's system here presented could be used in any form of HDR brachytherapy. However, in the range of energies typical from electronic brachytherapy, the scintillators composing the mPSD suffer from energy dependence and quenching [28, 106]. In such a case, additional correction factors have to be included and will depend on changes in energy spectra with distance from the source.

3.7 Conclusions

In this study, we presented the performance of an mPSD system for HDR brachytherapy and studied the uncertainty chain by extracting the relative contributions of measurement and positioning uncertainties as function of distance from the source. We used this analysis as a metric to find the conditions that ensure the best compromise between positioning and measurement uncertainties for mPSD calibration. The mPSD angular response was flat within 2%, provided that cross re-excitation of the scintillators was prevented by a bandpass filter. The triangulation approach was applied to track the source position in space. As long as the mPSD-to-source distance was within 6 cm, the source position could be extracted to within 1 mm of the expected position, increasing to 1.8 mm at 10 cm. In all of the explored conditions, dose differences relative to TG-43 expected doses were within 5%. At distances up to 6.5 cm the dose deviation distribution for each sensor was within 2.5% of the TG-43 expected dose.

The mPSD's capacity for measuring the source dwell time was evaluated for a range of source displacement up to 10 cm, with a maximum single-scintillator deviation of 0.56 ± 0.25 s. The extracted dwell times from measurements exhibited the largest deviations for small dwell time values (1 s) and longer distances from the scintillator's effective position. However, the maximum average weighted deviation of the measured dwell times over all three scintillators was 0.33 ± 0.37 s. Thus, this study demonstrated that the described system can be used as an in vivo dosimeter for real-time source tracking, individual dwell time measurements, and dose reporting.

Acknowledgement

The present work was supported by the National Sciences and Engineering Research Council of Canada (NSERC) via the NSERC-Elekta Industrial Research Chair grants Nos. 484144-15 and RGPIN-2019-05038, and by a Canadian Foundation for Innovation (CFI) JR Evans Leader Funds grant # 35633. Haydee Maria Linares Rosales further acknowledges support from Fonds de Recherche du Quebec - Nature et Technologies (FRQ-NT) and by the CREATE Medical Physics Research Training Network grant of the Natural Sciences and Engineering Research Council of Canada (Grant # 432290). We also thank Amy Ninetto from Scientific Publications Services in the Research Medical Library at The University of Texas MD Anderson Cancer Center for editing our manuscript.

Chapter 4

3D source tracking and error detection in HDR using two independent scintillator dosimetry systems

Haydee M. Linares Rosales[1,2], Jacob G. Johansen[3], Gustavo Kertzscher[3], Kari Tanderup [3], Luc Beaulieu[1,2], Sam Beddar[4]

[1]Département de radio-oncologie et Axe Oncologie du CRCHU de Québec, CHU de Québec - Université Laval, QC, Canada.

[2]Département de physique, de génie physique et d'optique et Centre de recherche sur le cancer, Université Laval, Québec, Canada.

[3]Aarhus University Hospital, Department of oncology, Aarhus C, Denmark.

[4]Department of Radiation Physics, The University of Texas MD Anderson Cancer Center, Houston, TX 77003, United States.

4.1 Résumé

Objectif : Le but de cette étude est d'effectuer une reconstruction 3D de la position de la source en combinant des mesures de dosimétrie in vivo de deux systèmes de détection indépendants.

Méthodes : Des mesures du taux de dose ont été effectuées dans un fantôme d'eau pendant l'irradiation en curiethérapie HDR avec une source de ^{192}Ir. La réponse de deux systèmes de détection, le premier basé sur plusieurs détecteurs à scintillateur plastique (mPSD à trois points) et le second sur un seul cristal inorganique (ISD composé de CsI :Tl), a été combinée. Les données ont été acquises dans des conditions TG-43U1, y compris un plan de prostate HDR. Des cathéters ont été placées à des distances couvrant une plage de mouvement de source de 120 mm autour des détecteurs. La distance de chaque position d'arrêt à chaque scintillateur du mPSD a été déterminée sur la base des débits de dose mesurés et transposée en une position le long du cathéter (z) et à une distance radiale du mPSD (xy) pour chaque position d'arrêt de la source. La même méthodologie a été appliquée au ISD. Les coordonnées de la source en (x,y) et z ont été dérivées de l'intersection de la circonférence délimitée par le mPSD avec la sphère autour de l'ISD. Nous avons évalué la précision de la reconstruction de la position de la source en fonction de la distance à la source, de l'emplacement des détecteurs dans le volume de maesure (p.ex. la prostate), ainsi que la capacité de détecter les erreurs de positionnement.

Résultats : Environ 4000 positions d'arrêt ont été suivies pour huit plans HDR différents. Une intersection entre de l'anneau défini par les mesures du mPSD et de la sphère autour de l'ISD a été observée dans 77,2% des positions d'arrêt (en supposant aucune incertitude expérimentale). Cela a augmenté à 100% si une l'incertitude expérimentale (à hauteur de 1 σ) étaient comsidérées. Cependant, seulement 73 (96)% des positions d'arrêt planifiés ont été trouvées dans la bande d'intersection pour 1 (2) σ d'incertitudes. La différence entre les positions reconstruites et planifiées de la source était généralement inférieure à 3 mm pour une plage de distances à la source allant jusqu'à 50 mm. À des distances supérieures à 50 mm, des écarts plus importants sont observés. Les mesures pour un plan de prostate HDR démontre que l'importance su positionnement ds détecteurs, avec au moins un des détecteurs situé au milieu du volume donnant de meilleurs résultats par rapport aux scénarios où les deux détecteurs étaient situés en dehors du volume de la prostate. L'analyse a montré une probabilité de détection qui, dans la plupart des cas, est loin du seuil de détection aléatoire. Des erreurs de 1 (2) mm peuvent être détectées dans des plages de 5-25 (25-50) mm de distance à la source, avec un taux de vrai positif et vrai négatif supérieur à 80%.

Conclusion : En combinant les réponses de deux détecteurs, nous avons déterminé les coordonnées absolues de la source d'^{192}Ir. La combinaison du système mPSD et ISD en curiethé-

rapie HDR, constitue une alternative prometteuse pour le suivi de la position de la source en 3D en temps réel.

4.2 Abstract

Purpose: The aim of this study is to perform 3D source position reconstruction by combining in vivo dosimetry measurements from two independent detector systems.

Methods: Time resolved dosimetry was performed in a water phantom during irradiation of a ^{192}Ir HDR brachytherapy source using two detector systems. The first was based on multiple (three) plastic scintillator detectors and the second on a single inorganic crystal (CsI:Tl). Brachytherapy treatments were simulated in water under TG-43U1 conditions, including an HDR prostate plan. Treatment needles were placed in distances covering a range of source movement of 120 mm around the detectors. The distance from each dwell position to each scintillator was determined based on the measured dose rates. The three distances given by the mPSD was recalculated to a position along the catheter (z) and a distance radially away from the mPSD (xy) for each dwell position (a circumference around the mPSD). The source x, y, and z coordinate were derived from the intersection of the mPSD's circumference with the sphere around the ISD based on the distance to this detector. We evaluated the accuracy of the source position reconstruction as a function of the distance to the source, the most likely location for detector positioning within a prostate volume, as well as the capacity to detect positioning errors.

Results: Approximately 4000 source dwell positions were tracked for eight different HDR plans. An intersection of the mPSD torus and the ISD sphere was observed in 77.2 % of the dwell positions, assuming no uncertainty in the dose rate determined distance. This increased to 100 % if 1σ uncertainty bands were added. However, only 73(96) % of the expected dwell positions were found within the intersection band for 1(2) σ uncertainties. The agreement between the source's reconstructed and expected positions was generally within 3 mm for a range of distances to the source up to 50 mm. At distances beyond 50 mm, more significant deviations are observed. The experiments on an HDR prostate plan, showed that by having at least one of the detectors located in the middle of the prostate volume, measurement deviations considerably reduced compared to scenarios where the detectors were located outside of the prostate volume. The analysis showed a detection probability that, in most cases, is far from the random detection threshold. Errors of 1(2) mm can be detected in ranges of 5-25 (25-50) mm from the source, with a true detection probability rate higher than 80 %.

Conclusions: By combining two detector responses, we enabled the determination of the absolute source coordinates. The combination of the mPSD and the ISD in vivo dosimetry constitutes a promising alternative for real-time 3D source tracking in HDR brachytherapy.

4.3 Introduction

Brachytherapy (BT) is a cancer treatment modality in which radiation dose is administrated to patients through a radioactive source placed in/or close to the tumoral region. BT treatments are employed for a wide variety of cancers such as skin, gynecological, breast, prostate and lung cancer [14, 107]. The high gradient field is the main advantage BT offers, allowing to deliver a high dose to the target while preserving adjacent healthy tissues and reducing the toxicity level. However, the accurate dose planning and delivery requires a very high level of precision, as a dose variation of more than 10 % per mm can be expected close to the source. This can make even small treatment miss-administration or errors lead to nefarious consequences in patients if it goes undetected.

At the same time, the steep dose gradients poses a challenge for accurate dose verification. In vivo dosimetry (IVD) is the most direct measurement of the absorbed dose in regions of interest like organs at risk (OAR). IVD is therefore an ideal candidate for treatment verification during BT. Despite several studies [10, 14, 48–53] focusing on developing methods for real-time monitoring, nowadays there is a limited availability of commercial systems that allow for the implementation of such a technique. Thus many Centers don't perform IVD, and therefore events may remain unnoticed, or if detected they are typically only identified post-treatment [10]. A study published by Tanderup et al. [7] summarized the aspects that need to be taken into account when considering a detection system as a potential tool for IVD applications in BT. In this study, plastic and inorganic scintillators were used together. Scintillator detectors have characteristics (size, sensitivity, online read-out) that make them suitable for this kind of applications. Plastic scintillator detectors (PSDs) are furthermore water equivalent. On the other hand, they are affected by stem effect, which is the contaminating Cherenkov and fluorescence light induced in the fiber-optic cable. Stem effect can cause large deviations in the measured dose rate for/in/during HDR BT with an ^{192}Ir source, if not taken into account [22, 23]. The production and removal of stem effect in PSDs are widely discussed topics [16, 17, 20, 32, 35–37, 75]. Furthermore, the use of PSD in a multipoint configuration (mPSD) could be used to assess the dose at multiple points simultaneously, thereby improving treatment verification quality and accuracy [9, 31, 33]. Inorganic Scintillator Detectors (ISD) exhibit light yields (photons/keV) 2-3 orders of magnitude greater than PSDs [86]. The high signal intensity reduces the impact of the stem signal to a neglible level. Furthermore, it enables the use of smaller scintillator volumes that measure dose rates with small statistical uncertainties. ISDs are however not water equivalent and they exhibit an energy dependence on the photon spectrum they are exposed to.

This paper will focus on the use of four scintillator point detectors for real-time 3D source tracking in HDR BT. The study was performed with an ISD and a mPSDs systems. The latter containing three PSDs as described by Linares et al. [108]. Both mPSD and ISD

have previously been used for source tracking during BT. In both cases a degeneracy in the azimuthal angle was observed [10,108]. In this paper, the two systems are combined to resolve this degeneracy.

4.4 Materials and Methods

4.4.1 The detector systems

Two independent detector systems were used in this study, one for the mPSD and one for the ISD. These are described in this section.

mPSD system

One of the systems used for HDR BT was a 1 mm diameter mPSD composed by organic scintillators BCF-10, BCF-12 and BCF-60 scintillators from Saint Gobain Crystals (Hiram, Ohio, USA), with lengths of 3 mm, 6 mm, and 7 mm respectively. The scintillators and optical fiber were tightly light-shielded. The mPSD was coupled to 15 m long optical fibre type *Eska GH-4001* from Mitsubishi Rayon Co., Ltd. (Tokyo, Japan) connecting to a light collection box. The box consisted of a beam aligner block A10760 from Hamamatsu (Bridgewater, USA) [89] coupled to an Olympus infinity-corrected objective lens RMS40X from Thorlabs (Newton, USA); as well as photomultipliers tubes (PMT) coupled to a set of dichroic mirrors and filters. Four sets of PMTs, mirrors and filters were used, one for each scintillator and one to account for the stem effect [22,32]. A detailed description of the entire system can be found in [30,108].The signal was read and sent to a computer at a rate of 100 kHz using a data acquisition board (DAQ) type DAQ NI USB-6216 M Series Multifunction from National Instruments (Austin, USA) [90]. The scintillation light detection system is independently controlled from the irradiation unit with homemade software based on Python.

ISD system

The ISD consisted of a 1.0 mm-diameter and 0.5 mm-long scintillating crystal made of CsI:Tl that was coupled to a 1 mm-diameter and 15 m-long fiber-optic cable. The crystal and optical fiber were shielded from light using an opaque plastic tube. A more detailed characterization of the CsI:Tl crystal can be found in [86,87]. The optical fiber was connected to a Si-diode photodetector (s8745-01 from Hamamatsu), which was connected to a data acquisition system (usb2408 from Measurement Computing) that monitored the signal with a 30 kHz sample rate. The signal was averaged across 50 ms internally in the data acquistion system before sent to the user computer at a rate of 20 Hz.

4.4.2 Dose measurements

Dose measurements were carried out in a 40 × 40 × 40 cm^3 water tank with an additional layer of 10 cm solid water (Plastic Water Standard, CIRS, Virginia, USA) on each side to ensure TG41-U1 conditions [46]. A Flexitron HDR afterloader from Elekta (Elekta Brachy, The Netherlands) coupled to 30 cm needles from Best Medical International (Springfield, VA, USA), was used for irradiation. The needles were placed in the water tank in a series of different configurations (see section 4.4.2) by means of a custom-made poly(methyl methacrylate) holder composed of two needles insertion templates of 12 x 12 cm^2, each having 225 holes in a 5 mm spacing grid [9, 30]. Both template were placed 20 cm apart. All needle ends were placed at the same height. The mPSD and ISD dimensions allowed them to be inserted into an additional needle each. The guidetubes were connected to the treatment needles, before the two detectors were placed in their respective needles. The dose rate was recorded with both systems and analysed post-irradiation.

Study cases

Three different treatment configurations were used as study cases. Figure 4.1 shows a schematic of the two detectors and needles distribution in the x-y plane. The first type of treatment was used to study the response of the dosimeters when arranged in a symmetric configuration relative to the detectors as shown in figure 4.1(a). The detectors were surrounded by nine hollow plastic needles at different distances in the x-y axis. In the second treatment configuration (figure 4.1(b)) sixteen needles were positioned asymmetrically around the detectors in a very confined space. The third type of treatment used in this study was an HDR prostate plan. The needles, detectors, as well as the custom-made poly(methyl methacrylate, PMMA) holder were scanned using a CT on rails Somaton Sensation Open from Siemens (Malvern, USA). The CT scan geometry was exported to Oncentra Brachy v4.0 (Elekta Brachy, The Netherlands) where the plan was created with a prescribed dose per fraction of 15 Gy. Figure 4.1(c) shows a schematic of the template used for a prostate treatment irradiation. Sixteen needles were reconstructed and used for treatment delivery. Several measurements were done in order to evaluate the benefit of positioning the mPSD and ISD in different locations inside the treatment volume.

Table 4.1 details the characteristics of the plans created. The first column in table 4.1 shows the set-up configuration used for measurements according to figure 4.1. The second column refers to the plan number assigned to each test and will be used in the further sections. The third and fourth columns in table 4.1 show the x,y,z coordinates of the position of the ISD and mPSD respectively. The mPSD z-coordinate refers to BCF10's position. The fifth column in table 4.1 shows the number of needles used for irradiation. The sixth column

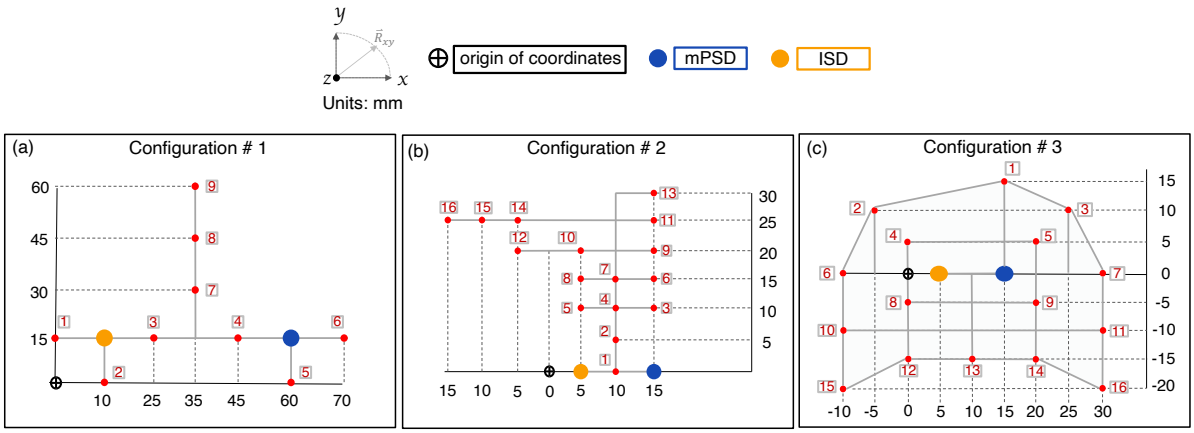

Figure 4.1 – Schematic of the 2 detectors and needles distribution in the x-y plane during in-water measurements with the mPSD and ISD systems. Measurement set-up when studying the dosimeters response in a symmetric (a) and asymmetric (b) configurations. (c) Needle positions during the HDR prostate plan irradiation. The detectors are placed as in plan 5.

shows the number of dwell positions planned at each needle, while in column seven are shown the lowest/highest distances explored in the z-axis. Column number eight contains the dwell position steps planned for each treatment. The last column in table 4.1 refers to the dwell times used for measurements.

Table 4.1 – Irradiation plan parameters used to study the mPSD and ISD systems response. The number of dwell position, source step and dwell time varied from position to position in configuration 3. Therefore only the ranges [min-max] are given.

Configuration	Plan	ISD position (mm)	mPSD position (mm)	Number of needles	Number of dwell p.	lowest/highest Z (mm)	Source step (mm)	dwell t (s)
1	1	(10, 15, 0)	(60, 15, -4.4)	9	21	-31/+69	5	5
2	2	(5, 0, 0)	(15, 0, 19)	16	101	-25.8/+74.2	1	3
3	3	(5, 0, 0)	(15, 0, -6.8)	16	2-8	+18.6/+53.6	5-30	0.2-34.1
	4	(10, -20, 0)	(15, 0, -4.2)	16	2-8	+20.6/+55.6	5-30	0.2-34.1
	5	(10, 20, 0)	(15, 0, -6.0)	16	2-8	+19.2/+54.2	5-30	0.2-34.1
	6	(10, 20, 0)	(10, -20, -4.0)	16	2-8	+17.6/+52.6	5-30	0.2-34.1
	7	(0, -20, 0)	(20, -20, -4.4)	16	2-8	+18.2/+53.2	5-30	0.2-34.1
	8	(5, 0, 0)	(15, 0, -6.8)	16	121	-44/+76	1	1

4.4.3 Calibration

A calibration is needed to transform the recorded signal into dose rate for each system. The calibration for the mPSD included removal of the stem signal, while the calibration for the ISD included an energy correction term. Both calibrations were carried out using measurements obtained under the same experimental conditions as described above.

The calibration matrix and dose values for the mPSD were calculated according to the formula-

tion published by Linares et *al.* [30] for a 3 points mPSD configuration, based on the formalism proposed by Archambault et al. [32]. Thus the quantity of interest, dose, is insensitive to stem effect contribution.

The ISD calibration was performed using a series of dwell positions in needle 1 of configuration 1. A total of 101 dwell positions were used with dwell step size of 1 mm and dwell times of 5 s. The shape of the measured dose rates were used to determine the point in the source needle closest to the ISD. The actual distance to the detector for each dwell point could then be derived. A calibration coefficient (CF) was determined as the ratio of the measured signal and the dose rate based on TG43 for each of the points taking into account the energy correction, which was determined prior to the calibration. The energy dependency was determined by measuring the signal from the source at a range of source positions. The positions covered distances from 5 mm to 50 mm and angles from 10 degrees to 170 degrees. The ratio of the measured signal and the dose rate based on TG43 was determined at each point and normalised at 10 mm, 90 degree. The ratio was then plotted as function of the measured dose and fitted to polynomial function. The equation for transforming measured signal (MS) from the ISD to dose rate (DR) is given in equation 4.1.

$$DR = \frac{MS \cdot CF}{3.872 \cdot 10^{-6} \cdot (MS/S_k)^{-0.8083} + 0.6517} \tag{4.1}$$

Here S_k is the source strength.

4.4.4 3D source position reconstruction

From dose rate to distance to the source

The dose rate for a given dwell position was determined for each of the four sensitive volumes by averaging the signal in Volt recorded during the dwell. This average value was then converted into dose rate using the calibration described in section 4.4.3. The distances between the individual source positions and the individual sensitive volumes were determined based on the relation between dose rate and distance on TG43-U1 formalism $r(\theta)_{i,j} = f^{-1}_{TG43}(DR)$. Here i, j is the source dwell position and the four active volumes/crystals respectively. f^{-1}_{TG43} is the inverse function of the TG43-U1 formalism. The angular dependency stems from the anisotropy of the dose distribution. In the same manner, the uncertainty of the mean dose rate were determined and transformed into an uncertainty in the distance $\sigma_{r_{i,j}}$. Thus, a distance and uncertainty between source and sensitive volume were determined for each dwell position and each sensitive volume.

The relative position of the four sensitive volumes are known as well as the distance from a single dwell position to each volume. This enables a determination of the most probable dwell position based on dose rate, as described in 4.4.4.

Needle offset calculation

The positioning and CT reconstruction of the needle and dosimeters lead to a positional uncertainty in the order of 0.5 mm. To reduce this positional uncertainty, needle offsets were calculated using the radial distances measured with the mPSD's sensors and the ISD. According to the recommendations provided by Johansen et *al.* [10], the distance offset of the measurements, was separated into a shift along the needle (z) and one radially away from the dosimeter (r). This was done by making a joint virtual shift of all the dwell positions in a single needle to best match the measured dose rates to TG43. The needle shift was found applying the *Dynamic Time Warping* (DTW) method. DTW is a well-known technique to find an optimal alignment between two given sequences. It is a point-to-point matching method under some boundary and temporal consistency constraints. The sequences are warped in a nonlinear fashion to match each other [109].

Figure 4.2 shows an example of the needle shift fitting routine used in this paper. The needle shifts calculations were done following 2 steps. We first built the 2D-shaped sequences of data to be used. The first sequence was created using the ensemble of radial distances measured by the four detectors (measurement sequence, blue dots in figure 4.2). The second sequence was used as a reference and built based on the planned radial distance to each one of the detectors (red line in figure 4.2). Both, the measurement and reference sequences were created as a function of the afterloader indexer or index number, which is the shared information between the detectors. However, since the shift analysis involved four scintillators, for each needle, the index number's array had dimensions equal to four times the afterloader indexer. Thus, the sequences' information was sorted concatenating the information for each one of the scintillators in the following order: BCF10, BCF12, BCF60, CsI:Tl. In the second step, our DTW algorithm simulated shifts in the reference sequence's r and z directions to find the optimal fit to the measured data (dashed-blue lines in figure 4.2). Since at short distances to the source miss-positioning errors has more remarkable effects and the measurement uncertainty increases with the distance to the source [8], the inverse square of the distance to the source was used as a weighting factor for DTW calculations. A (z, r) offset were found for all needles in all the configurations in Table 4.1, and the updated source positions were used as the ground truth in the further analysis.

3D source position reconstruction

The 3D ^{192}Ir source location in the space was calculated finding the intersection between the circumference predicted with the mPSD and the sphere around the single ISD. Figure 4.3 shows the schematic of the mPSD-ISD responses (degeneracy) to determine the source position in a 3D space. Figure 4.3(a) shows the schematic when the measurement uncertainty

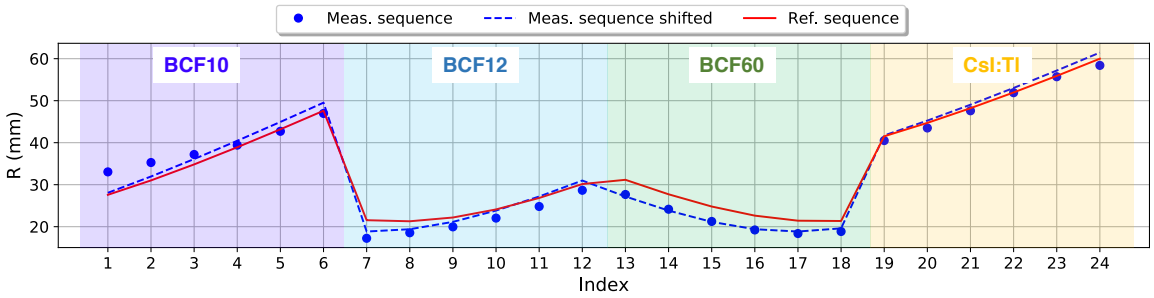

Figure 4.2 – Example of the needle shift fit routine. The blue dots are the measured radial distances (measurement sequence) for the dwell positions, the red line is the expected curve based on the planned positions (reference sequence), the dashed-blue curve is after the shift in needle position. The inserted shaded regions represent the index limits for the data collected by each scintillator. For interpretation of the references to color in this figure legend, the reader is referred to the Web version of this article.

is excluded from the source location calculation. In such a case, and based on the distance to the detectors, the goal is to find the intersection points between the mPSD's predicted circle and the sphere around the ISD. When the mPSD-ISD intersected once, the intersection point was used as source location. In cases where two intersection points were found, the closest point to the planned location was used as source coordinate. In case of no interception, we selected, for the mPSD, the point on the torus (figure 4.3) closest to the planned position, and for the ISD, the point on the sphere closest to the planned position. Then the average of these two coordinates was used as reconstructed source position.

Figure 4.3(b) shows a schematic of the intersection areas obtained when including the uncertainty budget of each dosimeter in the calculations. The uncertainty in the measured dose rates were transformed into uncertainty bands on the distances, and the intersection areas were determined rather than intersection points. In figure 4.3(c) are represented the possible cases that can arise when extracting the intersection region in 4.3(b). The source location was defined as the mean coordinate defined by the region. In cases where more than one intersection band was found (figure 4.3(c) case 3 and 4), the closest band to the planned source position was selected.

4.4.5 Detection of positioning errors

The last experiment performed in this study was to evaluate the capacity of the mPSD-ISD combined system to detect treatment positioning errors in HDR BT with an ^{192}Ir source. This analysis was done in two stages. We initially derived the Receiver Operating Characteristic (ROC) curve and based on it, we analyzed the performance through positioning errors introduced in configuration #1 and #3 in figure 4.1. The reasoning to build the ROC, was to establish a metric that allows during real-time acquisitions the classification of deviations

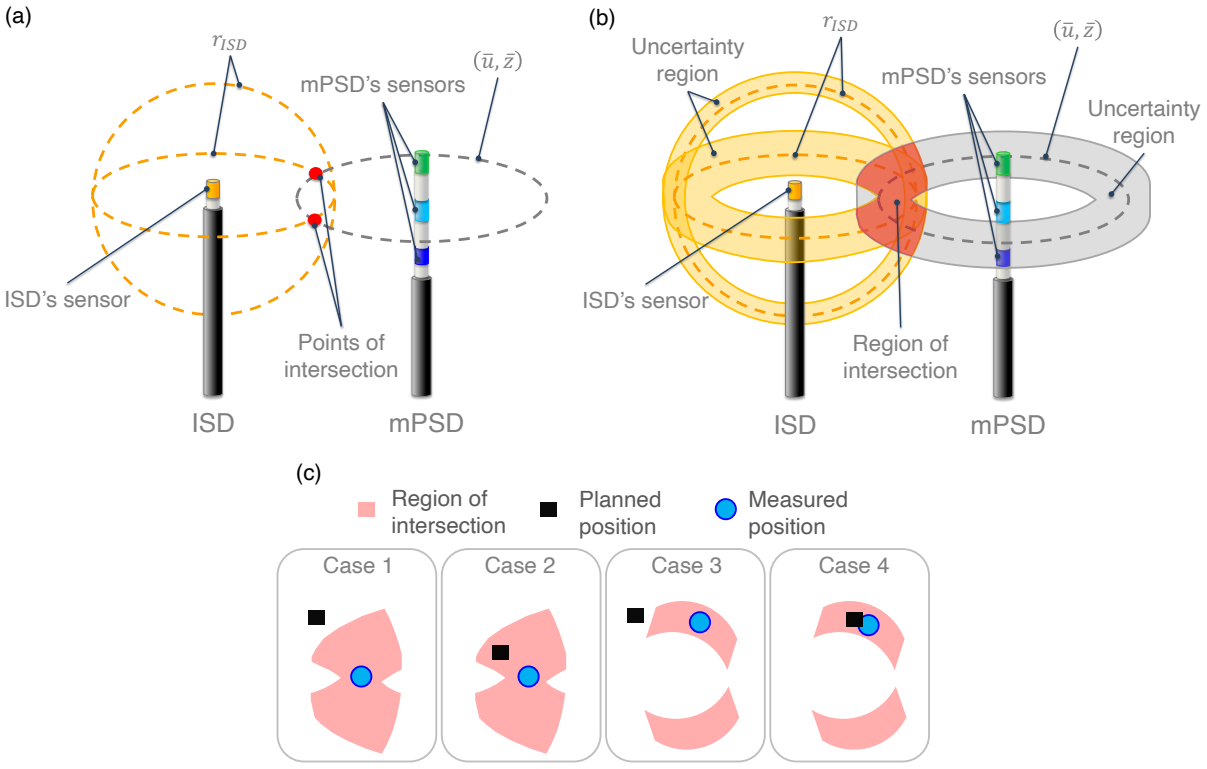

Figure 4.3 – Schematic that illustrates the combination of mPSD-ISD responses to determine the source position using no uncertainties (a) and non-zero uncertainties (b), and possible cases (c) that can arise when extracting the intersection region in (b).

into possible errors with certain level of confidence.

Figure 4.4 shows the workflow followed to obtain the ROC curve. We build a database of information with 3741 dwell positions from plans number 1, 2, and 8 in table 4.1. Three main steps were followed. In step 1 we extracted the planned and measured source coordinates in a 3D space after offset correction as described in section 4.4.4. We then calculated the point-to-point *Euclidean distance* between the measured and planned location. This array of *Euclidean distances* is referred as the *reference deviation*. In step 2, we used the measured source coordinates without modifications. However the planned coordinates were modified to simulate positioning errors. Dwell positions were randomly selected, and errors of 0.5, 1.0, 1.5, 2.0, 2.5 and 3.0 mm were introduced by shifting the z coordinate. The point-to-point *Euclidean distance* was then calculated using the measured and the "modified" source coordinates. This data-set of deviations is referred as *modified deviations*. The dichotomous analysis is performed in step 3. We used the *reference* and *modified* deviations to quantify the sensitivity/specificity of the dosimeters in detecting the errors introduced. For each error simulated, a contingency table was built associating an error to a deviation beyond a given range. Those dwells where no error was programmed and the system detected no error constituted the true negatives, while the dwells where an error was programmed and detected constituted the true positives.

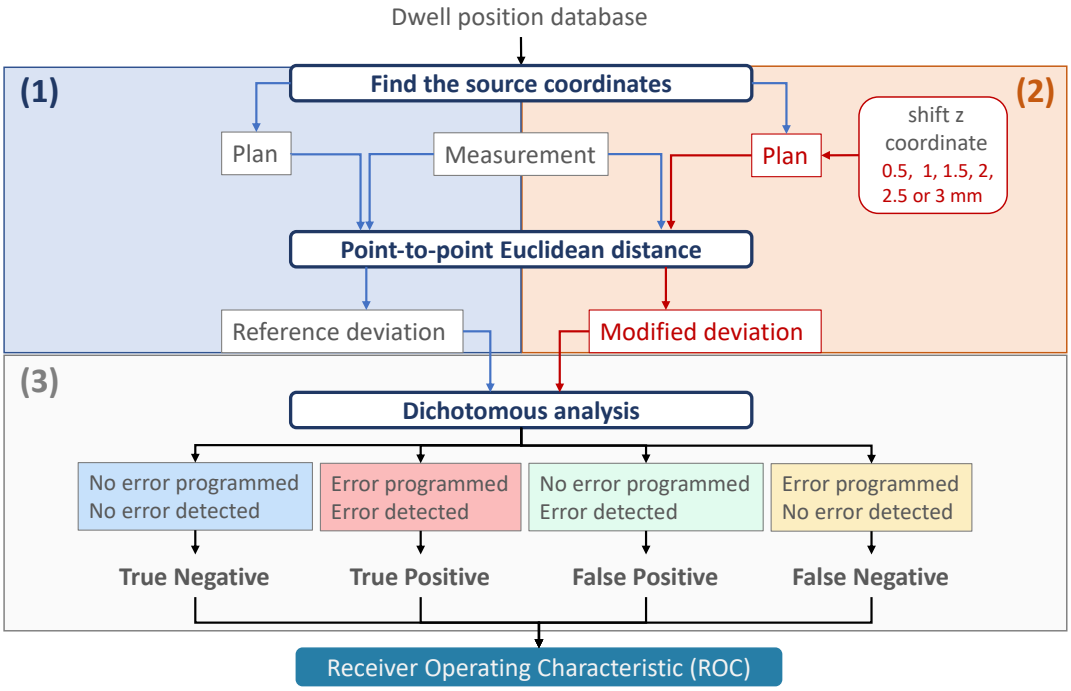

Figure 4.4 – ROC calculation workflow.

If at a specific location, the system detected a condition different from the reference, then we classified that deviation as false-negatives or false-positives. Since the error detection is influenced by the measurement uncertainty [7,8], the ROC analysis was done for three ranges of radial distances with respect to the source independently: 5 - 25 mm, 25 - 50 mm and 50 - 75 mm.

Different plans were delivered with and without modifications made to the reference source position. We aimed to simulate different types of dose delivery errors that current afterloader safety systems are unable to detect. The study was conducted using the configuration number 1 and 3 in table 4.1. In configuration number 1, the needles 5 and 6 were exchanged; and wrong dwell positions were planned in needles 3, 7, and 9. For the irradiations in a prostate template (configuration number 3), plan 3 constituted the reference. Needle 5 and 9 were swapped, as well as needle 12 with 13, and 15 with 16. The deviations were classified into error or not, using the ROC curves as the metric and a *distance-based threshold selection*. In the *distance-based threshold selection* approach, the threshold to consider a deviation as an error was set by fixing the combination of false positive rate (FPR) at 20 % and the true positive rate (TPR) at 80 %. Thus for dwell positions with a planned distance to the source within 5 to 25 mm range, the deviation threshold used was 1 mm; for dwells falling within 25 to 50 mm range, the deviation threshold used was of 2 mm; and for the dwell positions with distances to the source beyond 50 mm, the deviation threshold used was 3 mm.

4.5 Results

4.5.1 Measurement uncertainty influence on the source position reconstruction accuracy

A total of 3741 source dwell positions were tracked while using the plans number 1, 2, and 8 in table 4.1. A range of 120 mm in the z-axis was covered. The violin plots [100] in figure 4.5 show the density distributions of the differences between the measured source position and the planned position in the x, y and z axis. The inner boxes represent the interquartile ranges, and the line inside the boxes indicate the median values of the distributions. The black dots in each deviation distribution represents the outliers (points which fall more than 1.5 times the interquartile range above the third quartile or below the first quartile). The analysis performed assuming no measurements uncertainty in extracting the source location calculation is represented by 0σ in figure 4.5. 1σ and 2σ in figure 4.5 refers to the deviations obtained when the uncertainty in the measured dose rates were transformed into uncertainty bands to find the source location. Table 4.2 summarizes the influence of the uncertainty budget in the measurement accuracy of the source location in a 3D space. Number of dwells with intersections refer to those dwell positions where an intersection between the mPSD's predicted ring and the sphere predicted by the ISD intersect. The analysis shown in the following sections corresponds to a source tracking with 2σ bands criterion.

Table 4.2 – Influence of the uncertainty budget in the measurement accuracy of the source location in a 3D space.

	0 σ	**1** σ	**2** σ
Number of dwells with intersection	77.2 %	100 %	100 %
Expected positions within the intersection area	Not applicable	73 %	96 %

4.5.2 Source position reconstruction accuracy as function of the distance to the source

The distance dependency of the deviations (2 σ) shown in in table 4.2 is given in figure 4.6. Figure 4.6 shows the heat map of the mean deviations between the measured and expected source locations as a function of the distance to the mPSD-ISD systems. The radial distances to the mPSD (R_{mPSD}) were taken considering as the origin of the coordinates the position of BCF10.

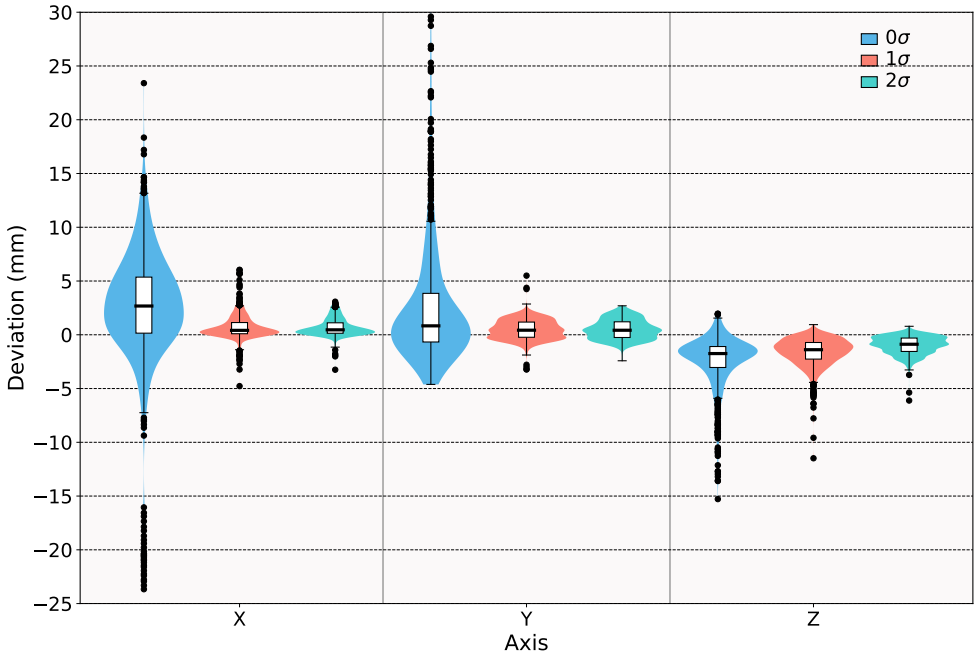

Figure 4.5 – Density distribution of deviations between the planned and measured position. Boxes represent interquartile ranges (quartile 1 and quartile 3), and the solid line inside the boxes represent the median values. The inner vertical lines extend from each quartile to the minimum or maximum.

4.5.3 mPSD-ISD positioning in an HDR prostate plan

Figure 4.7 summarizes the results obtained for irradiations with a prostate template (# 3 in table 4.1). The y-axis represents the point-to-point deviations between the mPSD-ISD's reconstructed source location and the planned position. The x-axis represents each dwell position index number. The vertical lines delimit each needle's data. For easy understanding and visualization of the results obtained, the schematics in the right panels of figure 4.7 illustrate the plan's number and for each the needle numbers as well as the detectors' positions. The squares in figure 4.7 represent the deviations from the plan when using the combined responses of the mPSD and ISD. The dots and triangles represent the independent contribution of the mPSD and ISD to the observed combined deviation. Overall, the accuracy in reconstructing the source position remains within 3 mm from the plan, especially if at least one dosimeter is placed centrally in the prostate.

4.5.4 Detection of positioning errors

Figure 4.8 summarises the key results obtained when quantifying the error detection probability as a function of the distance to the source. Figure 4.8(a) shows the ROC curves obtained

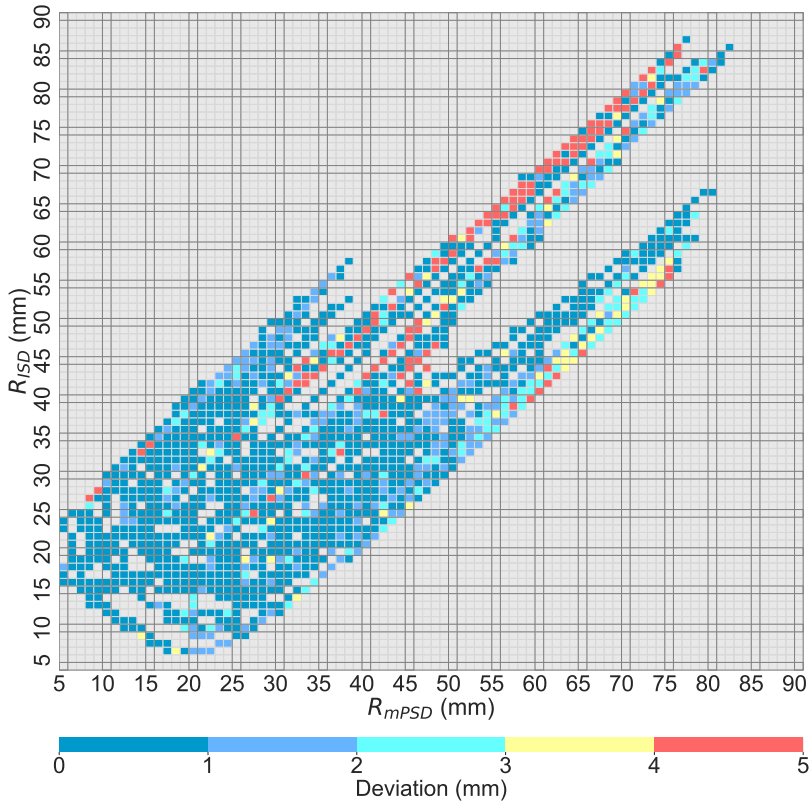

Figure 4.6 – Source position reconstruction deviations. Heat map of deviations between the measured and expected source locations as a function of the distance to the mPSD-ISD systems. The fields in gray represent the regions where no data is available to quantify the deviations. Please see the online paper version for color's reference.

for the different ranges of distances to the source. For visualization purposes, only the curves for introduced error of 0.5, 1.0, 2.0 and 3.0 mm are illustrated. Figure 4.8(b) shows the areas under the curve (AUC) as a function of the full range of introduced errors as well as for the three categories of source-to-dosimeter distances.

Figure 4.9 shows the heat map of deviations translated to an error probability according to the binary classifiers extracted from the contingency table for plans 1 and 3. The x-axis shows the dwell position index and the y-axis the needle number according to the schematic shown in figure 4.1. The fields in gray in figure 4.9 refer to non-programmed dwell positions.

Table 4.3 summarizes the results of the binary classification done over plan number 1 and 3 for error detection, where we show the results for the distance-based threshold selection as well as the results for fixed error's thresholds used in all the range of distances to the source. Active dwells in table 4.3 refers to the total number of active dwell positions on the plan used as the reference. The sensitivity expresses the proportion of actual positives that are correctly identified, while the specificity, the proportion of actual negatives that are correctly identified. The accuracy reflects the fraction of the measurement in agreement with what was expected.

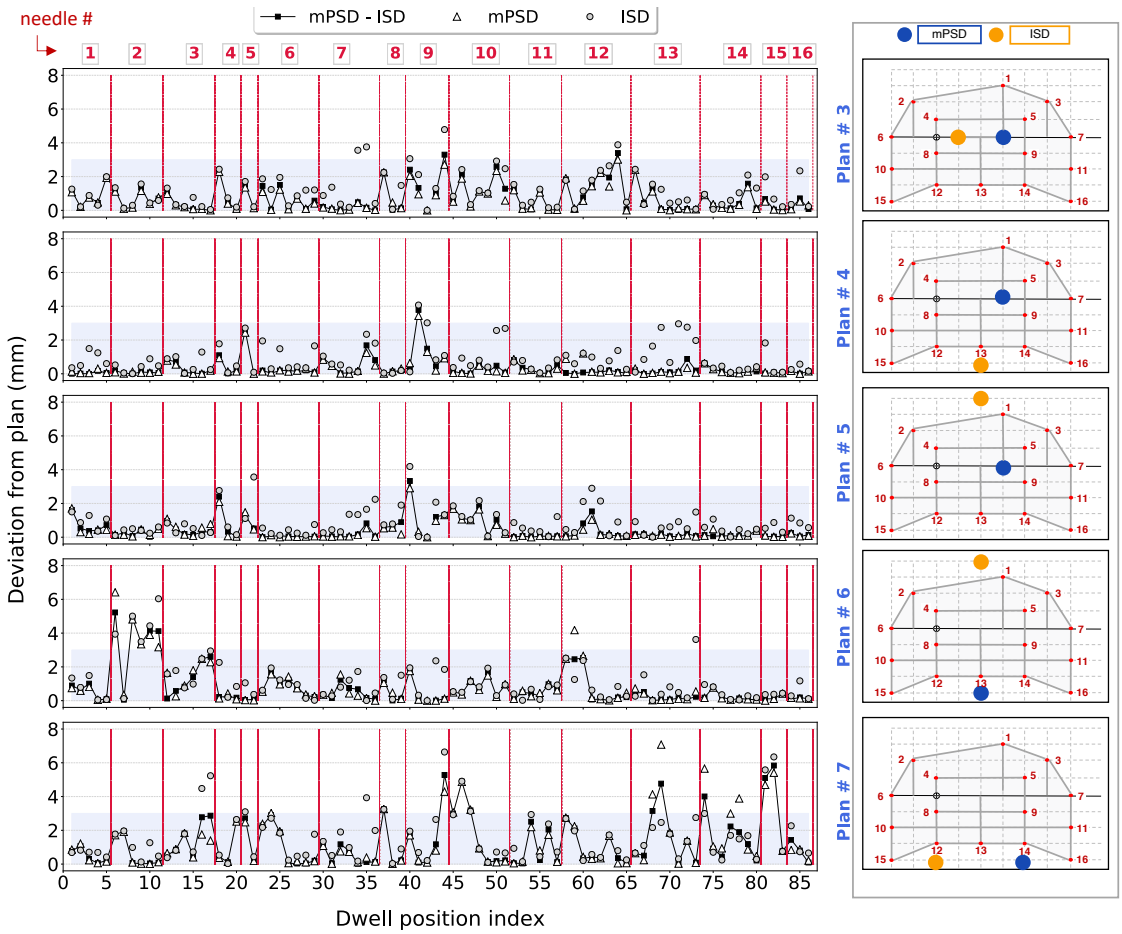

Figure 4.7 – mPSD-ISD deviations from the planned position for the prostate plan (C. # 3). The squares represent the deviations from the plan when using the combined responses of the mPSD and ISD. The dots represent the independent deviation of the ISD, while the triangles the mPSD's deviations. The vertical lines represent the limits of the data associated to each needle. The annotated values in the graph upper side show the needle numbers. The shaded region represents a 2 mm deviation range. The schematics in the right side of the figure illustrate the plan's numbers as well as the detectors' positions for each configuration.

The sensitivity, specificity and accuracy are statistical measures of the performance of a binary test such as the classification of an in vivo measurement into "No alarm" or "Alarm" [7].

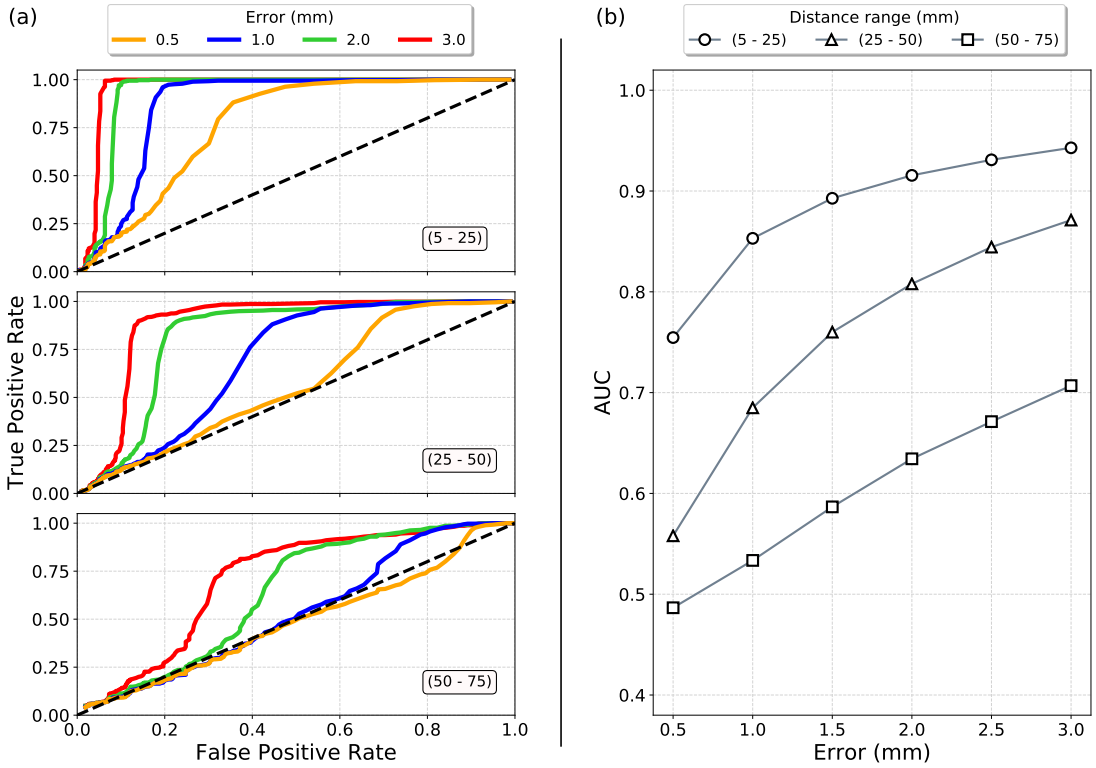

Figure 4.8 – mPSD-ISD error detection probability as a function of the distance to the source. (a) ROC analysis. (b) AUC. The dashed line in (a) shows the limit for random detection probability.

Table 4.3 – Summary of error detection probabilities found for plan 1 and 3.

Acceptance threshold (mm)	Plan	Active dwells (#)	True Negatives (#)	False Positives (#)	True Positives (#)	False Negatives (#)	Sensitivity (%)	Specificity (%)	Accuracy (%)
1	**1**	**189**	23	61	114	0	100.00	27.38	69.19
2			51	33	114	0	100.00	60.71	83.33
3			68	16	103	11	90.35	80.95	86.36
1, 2, 3 *			53	31	103	11	90.35	63.10	78.79
1	**3**	**86**	16	41	30	2	93.75	28.07	51.69
2			36	21	24	8	75.00	63.16	67.42
3			45	12	14	18	43.75	78.95	66.29
1, 2, 3 *			43	14	21	11	65.62	75.44	71.91

∗ Distance-based thresholds selection: 1 mm for dwells within 5-25 mm range, 2 mm for dwells within 25-50 mm range and 3 mm for dwells beyond 50 mm range.

4.6 Discussion

4.6.1 Measurement uncertainty influence on the source position reconstruction accuracy

The inclusion of the measurement uncertainty in the source location calculation leads to the improvement on the source location estimation accuracy. In such a case the highest densities

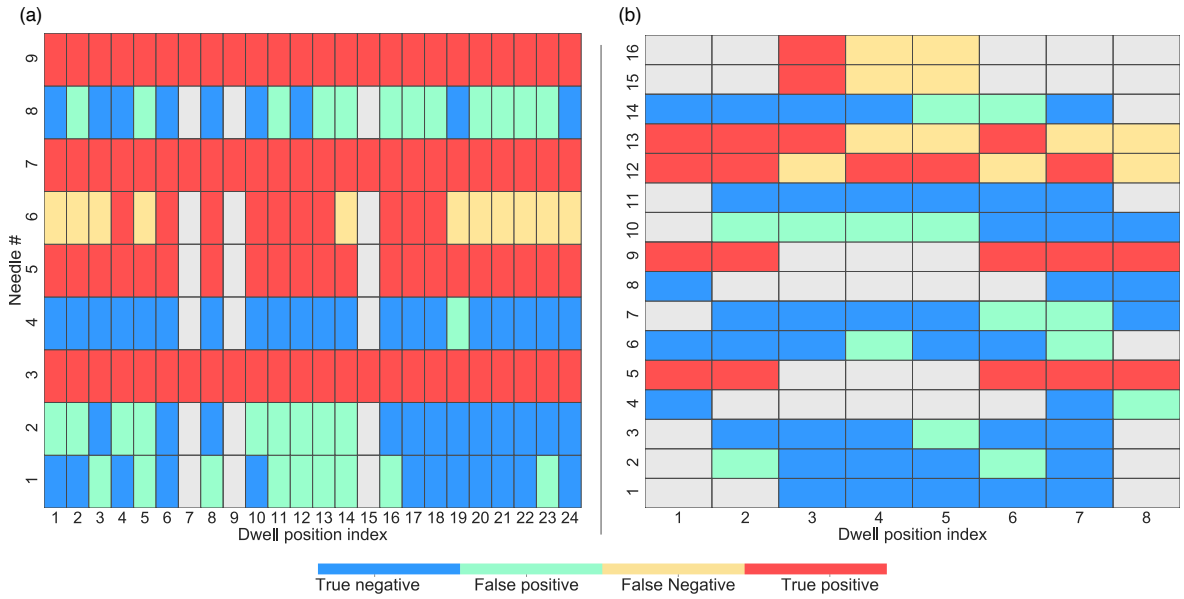

Figure 4.9 – Heat map of deviations classified into errors for plan number (a) 1 and (b) 3 when using the distance-based threshold to classify deviations as treatment' errors. The fields in gray correspond to not programmed dwell positions.

and median values were found close to 0 (values close to 0 and a small dispersion around it represent better agreement with the reference). When the uncertainty was excluded from the tracking process, no intersections were identified between the mPSD and ISD based distances in 22.8 % of the cases. In contrast, intersections were always identified when the measurement uncertainty was considered. However, only 73(96) % of the expected dwell positions were found within the intersection band for 1(2) σ uncertainties. Thus, considering a 2σ criteria increases the overlap regions between the two dosimeters and leads to a better agreement with the expected position in all axes.

4.6.2 Source position reconstruction accuracy as function of the distance to the source

In this study, we covered up to 12 cm range of source movement around the mPSD-ISD detectors. Figure 4.6 provides an idea on the experimental limits of the source tracking with the mPSD-ISD systems. For distances from the source greater than 5 cm, measurement uncertainties and possibly inaccuracies in the energy correction for the inorganic crystal lead to large positional uncertainties, between 3 and 5 mm from the planned position. For most clinical cases, dwell positions beyond 5-6 cm are rarely observed. However, finding HDR treatments with the ^{192}Ir sources stepping within a range of 5-6 cm is common in a clinical context, especially for prostate cases.

Several studies [10,12,14,48–53,110] have focused on the source tracking topic in HDR BT. The common point between those studies is the degeneracy in one of the detector axes, leading to source tracking report in a plane, not a point in the space. Some other authors have proposed different methods based on pinholes collimation panels to find the source location in 3D coordinates [111–114]. This is the first study to report on 3D source tracking based on point detector dosimetry. By combining the mPSD and ISD responses, we broke that degeneracy, enabling a determination the source location. The method here proposed can be extended to the combination of different systems. There is no restriction about which detector should be used for such a set-up.

4.6.3 mPSD-ISD positioning in an HDR prostate plan

The reconstruction of the source position in the prostate template (configuration # 3 in table 4.1) showed an overall agreement with the planned position of 3 mm or better for most dwell positions. Having at least one of the two detectors located inside the the prostate volume (plan # 3, 4, 5), reduces the measurement's deviations considerably. However, an increased deviation is observed in the experiments done with at least one of the detectors at distal positions from the prostate volume. As could be observed in plan # 6 and # 7 in Fig. 4.7, deviations up to 7 mm were seen, with the worst results in plan # 7, where both dosimeters are positioned out of the prostate volume. Thus selecting the optimal location for the detector's positioning within a clinical volume needs to be based on the system uncertainty and in particular the overall performance as a function of distances from the source.

4.6.4 Detection of positioning errors

In agreement with the study reported by Andersen et *al.* [8], as the detector-to-source distance increases, the capability to detect errors is affected. Because of an increase of the measurement uncertainties, at long distances to the source, large errors should occur, to be detected by the dosimetry systems. This effect is shown in figure 4.8. At short distances, there is a high probability of detecting positioning errors of 1 mm or more, with a low incidence of false alarms. As could be observed in figure 4.8(a), for the dwell positions with distances to the source beyond 50 mm, more than 3 mm of deviations has to be accepted if considering the FPR-TPR criterion previously set. However, according to the recommendations established for HDR BT practices [115], we decided to set the threshold to 3 mm of detected deviation relative to the planned position. The AUC was found higher than 0.85 and 0.68 at ranges of 5 - 25 and 25-50 mm from the source, respectively. However, for distances to the source within 50 - 70 mm range, the detection of 0.5 and 1.0 mm errors was essentially consistent with random results (AUC around 0.5), and only large errors of 3 mm or more can be detected with some confidence.

Figure 4.9 and table 4.3 summarize our findings when evaluating the detection of positioning errors and the *distance-based threshold selection* in plan number 1, and 3. mPSD-ISD's best performance was observed in plan # 1. The accuracy observed was 78.79% compared to 71.91% for plan # 3. The sensitivity in plan # 1 is also superior. Several factors can explain such behaviour. First of all, from the schematics in figure 4.1, we can infer that the needles distribution is more complex in configuration # 3 than configuration # 1. In the latter, a single intersection band (see figure 4.3c for reference) of its responses was found in 92 % of the dwell positions. In configuration # 3, the source position reconstruction was complicated by the symmetrical arrangement of needles relative to the mPSD and ISD (needles 4, 5, 8 and 9). In most of the dwell positions in needle 4, 5, 8 and 9, we found a dual-band behaviour. Thus the swap in those pairs of needles becomes difficult to detect if there is, for instance, similar "needles identities" (*i.e* having the same dwell positions planned). Thus, the second factor influencing the error detection capability is the needles arrangement and dwell position distribution around the mPSD-ISD locations. Thus detector positioning appears an important factor influencing outcome. In needle 5 and 9 in figure 4.9b, we were able to correctly detect the needle swap because, in needle 5, only the position 1 and 2 were active, while in needle 9, the active dwell positions were 6 to 8. Overall, dosimeter configurations shown in plan # 4 and # 5 constitute better choices. Based on these results, we recommend to have a dosimeter close to the central portion of the prostate and one in or very close to an OAR, for instance rectum or urethra. Fig. 7 shows the importance of having a dosimeter placed centrally, and our ROC analysis shows that a lower threshold can be set close to the dosimeter. Hence placing a dosimeter in OAR could put priority to that OAR.

Finally, the impact of using different thresholds (1,2 and 3 mm) for considering a deviation in the source position reconstruction as an error has been investigated (e.g. table 4.3). The use of 1 mm thresholds for all source-dosimeter distances improves the sensitivity. However, it compromises the specificity. For any system, there is a trade-off between sensitivity and specificity since the number of false alarms is increased if the sensitivity is increased by lowering the threshold for error detection [7]. The best balance sensitivity/specificity/accuracy in plan number 1 is obtained for a deviation threshold of 3 mm, while in plan number 3 is obtained with the distance-based threshold selection. The advantage of a distance-based threshold is that it leverages the maximum performance (as underlined by the AUC results) of a given dosimeter, taking into account its associated uncertainty chain. In a clinical setting, thresholds should be chosen to allow potentially clinically significant errors to be detected while accepting that this will result in some unnecessary treatment interruptions or post-treatment investigations.

In this paper, we solely used the threshold values extracted from the ROC analysis to classify deviations as errors. However, considering only the threshold criterion in combination with measurement uncertainty led to the miss-classification of an event into false positives/negatives. In this sense, if using, for instance, the distance-based threshold method, we found that

from the 67 dwell positions classified as false positives/negatives in plan number 1 and 3, the difference between reconstructed source position deviation from the plan and the classification threshold was smaller than 0.5 mm for 35 of them. Basing the action threshold in the results for a single dwell position will probably represent an unnecessary treatment interruption. A more robust algorithm for error classification has to be considered to minimize unnecessary treatment interruptions without forgetting the clinical significance of deviations. A solution to reduce the number of false alarms could be the inclusion of the source dwell time measurements in combination with the thresholds approach on source position deviations.

4.7 Conclusions

In this study, we performed a 3D source position reconstruction by combining in vivo dosimetry measurements from two independent detector systems. By combining the mPSD and ISD responses, we broke the degeneracy in the detectors' radial direction, enabling a determination of the source location. The inclusion of the measurement uncertainty in the source location calculation leads to improved source location estimation accuracy. For a range of distances within 50 mm from each system, the deviations in the source position reconstruction are below 3 mm from the planned position. The measurements in an HDR prostate plan configuration demonstrated the effectiveness mPSD-ISD combination for measurements in a range of distances to the source with clinical relevance. We recommend the positioning of one detector in the center of the prostate volume and the other outside of it. We also recommend a non-symmetrical distribution of the treatment needles around the detectors, which would allow the real-time detection of positioning errors with a high rate of accurate classification, while keeping the false alarms rate low.

Acknowledgement

The present work was supported by the National Sciences and Engineering Research Council of Canada (NSERC) via the NSERC-Elekta Industrial Research Chair grants Nos. 484144-15 and RGPIN-2019-05038, and by a Canadian Foundation for Innovation (CFI) JR Evans Leader Funds grant # 35633. Haydee Maria Linares Rosales further acknowledges support from Fonds de Recherche du Quebec - Nature et Technologies (FRQ-NT) and by the CREATE Medical Physics Research Training Network grant of the Natural Sciences and Engineering Research Council of Canada (Grant # 432290).

Chapter 5

On the use of machine learning methods for mPSD calibration in HDR brachytherapy

Haydee M. Linares Rosales[1,2], Gabriel Couture[1,2], Louis Archambault[1,2], Sam Beddar[3,4], Luc Beaulieu[1,2]

[1]Département de physique, de génie physique et d'optique et Centre de recherche sur le cancer, Université Laval, Québec, Canada.

[2]Département de radio-oncologie et Axe Oncologie du CRCHU de Québec, CHU de Québec - Université Laval, QC, Canada.

[3]Department of Radiation Physics, The University of Texas MD Anderson Cancer Center, Houston,TX, United States.

[4]The University of Texas MD Anderson UTHealth Graduate School of Biomedical Sciences, Houston, TX, United States.

5.1 Résumé

Objectif : Évaluer la faisabilité de l'utilisation d'algorithmes d'apprentissage machine (ML) pour l'étalonnage d'un détecteur multipoints à scintillateurs plastiques (mPSD) en curiethérapie à haut débit de dose (HDR).

Méthodes : Des mesures de dose ont été effectuées dans des conditions de curiethérapie HDR. Le système de dosimétrie consistait en un détecteur mPSD optimisé et d'un assemblage compact de tubes photomultiplicateurs couplés à des miroirs dichroïques et des filtres. La source de ^{192}Ir, contrôlé par un projecteur de sources, a été envoyée à diverses positions dans des cathéters maintenus en place par support en PMMA, garantissant une précision de position des cathéters de 0,1 mm. Des mesures de la dose pour des déplacements de la source allant de 0,5 à 12 cm du mPSD ont été effectuées dans des conditions conformes aux recommandations du TG-43 U1. Les doses individuelles aux scintillateurs ont été extraites à l'aide d'un modèle de régression linéaire, de forêt d'arbres décisionnels et d'un réseaux de neurones artificiels. La dose prédite par le formalisme TG-43 U1 a été utilisée comme référence pour l'étalonnage du système mPSD et pour l'entraînement des algorithmes de ML. Les performances des différents algorithmes ont été évaluées en utilisant différentes tailles d'échantillon et différentes distances source-mPSD.

Résultats : Nous avons constaté que les conditions d'étalonnage influençaient la précision de mesure de dose. Les écarts entre les valeurs de dose prédites par les différentes méthodes proposées et celles prévues par le TG-43 U1 sont généralement inférieurs à 20%. Néanmoins, ces écarts sont réduits à moins de 7% lorsque les mesures étaient effectuées dans la même plage de distances que celles utilisées pour l'étalonnage. Dans de tels cas, les prédictions avec l'algorithme de la forêt d'arbres décisionnels ont montré des écarts minimes ($<$2%). Cependant, la performance de cet algorithme a été compromise lorsque les prévisions ont été faites au-delà de la plage utilisée pour l'étalonnage. Étant donné que l'algorithme de régression linéaire peut extrapoler les données, la prédiction de dose par cet algorithme a été moins influencée par les conditions d'étalonnage par rapport à la forêt d'arbres décisionnels. Le comportement de l'algorithme de régression linéaire était plus lisse que celui des algorithmes de la forêt d'arbres décisionnels et du réseau de neurones dans la plage des distances ayant servi à l'étalonnage, mais les écarts observés étaient plus importants. Le nombre de mesures disponibles à des fins d'entraînement constitue le paramètre qui influence le plus les modèles de forêts d'arbres décisionnels et de réseaux de neurones. Leurs précisions tendaient à converger vers des écarts d'environ 1% à partir pour un nombre de positions d'arrêt supérieures à 100.

Conclusion : Les algorithmes d'apprentissage automatique couplés à un système mPSD optimisé sont des alternatives prometteuses pour la déconvolution précise de la doses d'un dosimètre mPSD pendant un traitement de curiethérapie.

5.2 Abstract

Purpose: We sought to evaluate the feasibility of using machine learning (ML) algorithms for multipoint plastic scintillator detector (mPSD) calibration in high-dose-rate (HDR) brachytherapy.

Methods: Dose measurements were conducted under HDR brachytherapy conditions. The dosimetry system consisted of an optimized 1-mm-core mPSD and a compact assembly of photomultiplier tubes coupled with dichroic mirrors and filters. An ^{192}Ir source was remotely controlled and sent to various positions in a homemade PMMA holder, ensuring 0.1-mm positional accuracy. Dose measurements covering a range of 0.5 to 12 cm of source displacement were carried out according to TG-43 U1 recommendations. Individual scintillator doses were decoupled using a linear regression model, a random forest estimator, and artificial neural network algorithms. The dose predicted by the TG-43U1 formalism was used as the reference for system calibration and ML algorithm training. The performance of the different algorithms was evaluated using different sample sizes and distances to the source for the mPSD system calibration.

Results: We found that the calibration conditions influenced the accuracy in predicting the measured dose. The decoupling methods' deviations from the expected TG-43 U1 dose generally remained below 20 %. However, the dose prediction with the three algorithms was accurate to within 7 % relative to the dose predicted by the TG-43 U1 formalism when measurements were performed in the same range of distances as used for calibration. In such cases, the predictions with random forest exhibited minimal deviations (< 2 %). However, the performance random forest was compromised when the predictions were done beyond the range of distances used for calibration. Because the linear regression algorithm can extrapolate the data, the dose prediction by the linear regression was less influenced by the calibration conditions than random forest. The linear regression algorithm's behavior along the distances to the source was smoother than those for the random forest and neural network algorithms, but the observed deviations were more significant than those for the neural network and random forest algorithms. The number of available measurements for training purposes influenced the random forest and neural network models the most. Their accuracy tended to converge toward deviation values close to 1% from a number of dwell positions greater than 100.

Conclusions: In performing HDR brachytherapy dose measurements with an optimized mPSD system, ML algorithms are good alternatives for precise dose reporting and treatment assessment during this kind of cancer treatment.

5.3 Introduction

Several studies [10,14,48–53,86,87] have focused on developing detectors and methods for real-time source monitoring in brachytherapy. The benefits and limitations of plastic scintillation detectors (PSDs) in a single or multi-point configuration (multipoint PSD [mPSD]) have been well documented [15–17, 19–21, 25–28, 30, 34, 75]. In a recent study, Linares Rosales *et al.* [30] demonstrated that with proper optimization of the optical chain in combination with the mathematical formalism proposed in [32], the use mPSD is suitable for real-time source tracking in high dose rate (HDR) brachytherapy.

The goal of the present prospective study was to evaluate the feasibility of machine learning (ML) algorithms for mPSD calibration in HDR brachytherapy based on prior mapping of the response of the mPSD to different radiation source positions. We compared three methods of scintillator dose decoupling: (1) a linear regression model [30, 32]; (2) a random forest estimator, and; (3) Artificial Neural Network (ANN) algorithms. To the best of our knowledge, no previous reported studies have examined the use of ML algorithms for scintillator detector calibration in HDR brachytherapy.

5.4 Materials and Methods

5.4.1 HDR brachytherapy dose measurements

Experimental setup

Dose measurements were performed in HDR brachytherapy, under full TG43 conditions [46,99]. The dosimetry system used for the measurements comprises three parts: 1) a fully optimized and characterized multi-point plastic scintillator dosimeter (1- mm- core mPSD; using BCF-60, BCF-12, and BCF-10 scintillators) [30], 2) a light detection system, and 3) a Python-based graphical user interface for system management and signal processing. The light detection system was composed of a compact assembly of photomultiplier tubes coupled with dichroic mirrors and filters for high-sensitivity scintillation light collection [30]. The photomultiplier tubes were independently controlled and read simultaneously at a rate of 100 kHz using a USB-6216 M Series multifunction data acquisition board (National Instruments, Austin, TX).

Figure 5.1 shows a schematic of the source positions with respect to the scintillators and the nomenclature used in this work. Each source dwell position was labeled as p_{nk}, where n represents the catheter number and k represents the point of measurement inside the catheter. Sixteen catheters were positioned in a PMMA holder [9,30], covering a 40-mm range of source displacement in the x direction. The source dwelled at 121 locations inside each catheter

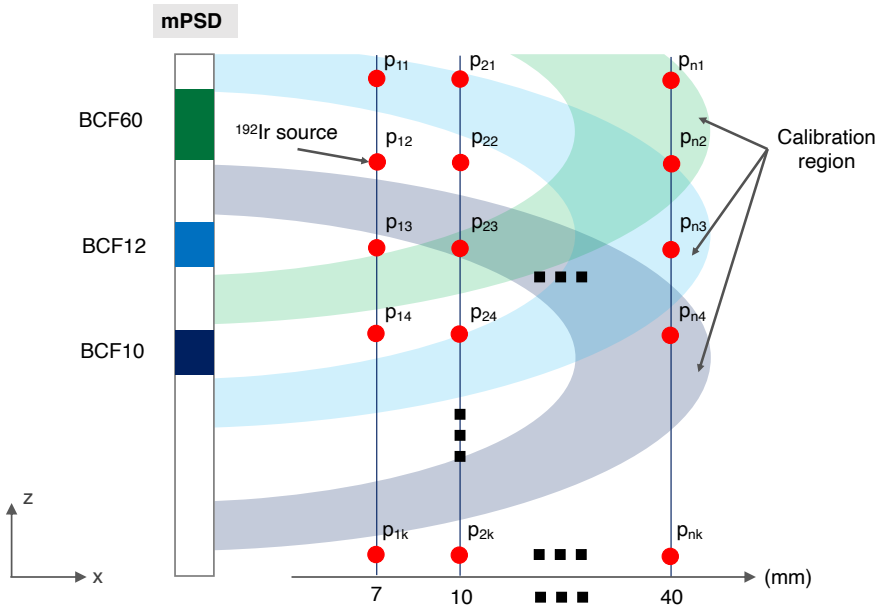

Figure 5.1 – Schematic of the source positions and nomenclature used for data training with ML algorithms during HDR brachytherapy dose measurements. The shaded regions around the scintillator centers represent the regions used during the system calibration.

with 1-mm steps for a total of 1936 independent dwell positions. A source dwell time of 1s was planned for each position. Thus, for a single source dwell position, 1×10^5 samples were collected. The circular-shaped shaded region around each scintillator center represents the region of radial distances considered during the system calibration (see section 5.4.2 for details).

Dose calculation model

According to a formalism for a three-point mPSD described previously [30] the signal produced by the source at position p_{nk}, can be described by the voltage function $V_{nk} = f([V^1_{nk}, V^2_{nk}, V^3_{nk}, V^4_{nk}])$, which is a combination of the four voltages $(V^1_{nk}, V^2_{nk}, V^3_{nk}, V^4_{nk})$ collected at each measurement channel of the mPSD system [30]. Dose calculation with mPSDs is based on the assumption that the recorded signal results from the linear superposition of spectra; no self-absorption interactions among the scintillators in the mPSD are considered [32].

Individual scintillator doses were decoupled using: 1) a linear regression model, 2) a random forest estimator and, 3) ANN algorithm. The linear regression model used for dose estimation is a hyperspectral approach previously for a three-point mPSD [30, 32]. A random forest is a meta-estimator that fits a number of classifying decision trees on various sub-samples of the data set and uses averaging to improve the predictive accuracy and control over-fitting. A regression tree is an efficient way of mapping a complex input space to continuous output parameters. Highly nonlinear mappings are handled by splitting the original problem into a set of smaller problems that can be addressed with simple predictors [116]. The linear regression and random forest dose calculations were done

using the *scikit-learn* Python library [117]. Also, an ANN is a family of algorithms involving several processing layers that learn representations of data. A fully connected network was used when doing the dose calculations with the ANN. The ANN was implemented with the *version 2.2.4* of the *Keras* framework [118], relying on the *TensorFlow* backend.

Table 5.1 summarizes the hyperparameters used to train each dose prediction model. The hyperparameters that are not specified were set to default levels. The random forest's hyperparameters were optimized using the grid search optimization method [119]. The ANN architecture was optimized using a manual search algorithm [119]. The input layer in the ANN had four neurons corresponding to the number of measurement channels in the mPSD system, whereas the output layer had three neurons corresponding to the received dose at each scintillator at a given source dwell position (p_{nk}). The number of neurons per layer used was 96, except in the study cases 2F-I in table 5.2. In those cases, to avoid overfitting of the dose, the number of neurons was set equal to the number of dwells used as training data. The early stopping method was used to monitor the loss function during the training phase. When the accuracy is not improved over 100 epochs, the training phase is stopped and outputs the best combination of weights.

Table 5.1 – Hyper-parameters used for training of the dose prediction models [117, 118].

Linear Regression	**Random Forest**	**Neural Network**
`fit intercept` = False	`number of estimators` = 300	`hidden layers` = 2
`normalize` = False	`maximum depth` = 80	`neurons per layer` = 96*
	`criterion` = mean square error	`Adam optimizer's learning rate` = 0.005
	`minimum sample to split` = 2	`batch size` = 16
		`number of epochs` = 1000
		`loss function` = mean absolute error
		`activation function of hidden layer` = ReLu
		`activation function of output layer` = Linear
		`weight initialization` = normal distribution
		`validation split ratio` = 0.2
		`early stopping patience` = 100

∗ The number of neurons per layer used was 96 all over the paper, except in the study cases 2F-I in table 5.2. In those cases, to avoid over-fitting, the number of neurons was set equal to the number of dwells used as training data.

The dose predicted by the TG-43 U1 formalism [46] was used as the reference for the system calibration and training. The finite size of each scintillator was accounted for during calculations; the TG-43 U1 dose values were integrated over each scintillator's sensitive volume.

5.4.2 Evaluation of the influence of calibration on the dose prediction model

The choice of calibration conditions influences the accuracy and noise of the measured dose [8, 30]. The measurement database was composed of the mPSD signals collected at 1936 dwell positions. Our first step was to randomly split the measurements' database into a training and testing data sets. The training data set was fixed as the 70 % (1355 dwell positions) of the measurements recorded at all the distances to the source (0-100 mm range). The testing data set was the remaining 30 % of the measurements (580 dwell positions), and was used to evaluate the model's performance in dose prediction. The performance of different algorithms was compared when using different sample sizes

and distances to the source for the mPSD system calibration. Thus, region mappings were radially created around each scintillator center according to the distance to the source (see figure 5.1 for visual reference). Two criteria were used to assess each model's performance as a function of the distance to the source used for calibration. The first criterion, referred to as the *inside region*, evaluated the model performance in the same region in which the calibration was performed. The second criterion, referred to as the *outside region*, evaluated the performance at distances outside the calibration region.

Table 5.2 summarizes the parameters used for defining the training and testing data sets in each case studied. The main goal of the study case 1 was to evaluate the impact of the distance to the source selection. With study case 2, the impact of the sampling size on the algorithms' dose prediction was assessed. The sampling size in Table 5.2 refers to the number of measurement points (i.e., dwell positions) considered for training and/or testing. The second and third columns in Table 5.2 list the ranges of distances considered during the training and testing processes. For the training data, those in the training data set falling in the desired region of interest for calibration were selected. Next, a percentage or number of dwell positions to be used as training data was randomly selected. Columns four to seven in Table 5.2 show information related to the sampling size used to train and test the algorithms. Column four lists the percentages of the training data used (relative to the available measurement database). Column five lists the numbers of dwell positions used for training purposes. For study case 1, 677 dwell positions were randomly selected from the training data set. Because the primary goal for study case 1 was to study the impact of the distance to the source and the available measurement data fluctuated according to each range of distances to the source, the training data were fixed to 677 dwell positions. For study case 2, different sampling sizes were randomly selected from the training data set over the entire range of explored distances to the source. Because the training data are randomly selected, when a small number of dwell positions is involved in the calibration, the accuracy of the dose prediction can be compromised by non optimal selection of the dwell position for mPSD calibration. Because of the aforementioned, for study cases 2F-I, the training data were randomly selected 150 times, and the system training was performed as well.

Table 5.2 – Data selection parameters for mPSD calibration with ML algorithms.

Study case ID		**Distance to the source**		**Sampling size**			
		Training	**Testing**	**Training**		**Testing**	
		(mm)	**(mm)**	**(%)**	**(# of dwell)**	**(%)**	**(# of dwell)**
1	A	0 - 50	0 - 100	35	677	30	580
	B	25 - 75					
	C	50 - 100					
	D	0 - 25 and 75 - 100					
	E	0 - 100					
2	F	0 - 100	0 - 100	0.2	4	30	580
	G			0.5	10		
	H			5	94		
	I			10	189		
	J			30	580		
	K			50	944		
	L			70	1360		

5.5 Results

5.5.1 The influence of the calibration on the dose prediction model

Distance to the source

Figure 5.2 shows the relative deviations (i.e., [measured - expected]/expected) from the expected TG-43 U1 [46] dose obtained with the random forest, linear regression, and ANN algorithms for the sensors in the mPSD. For visualization purposes, the figure only illustrates the results for the BCF-10 scintillator because the results for the BCF-12 and BCF-60 scintillators demonstrated the same behavior. Each solid line in the figure represents the median value of the distribution of deviations at each dwell position. The shaded regions contouring the models' median values represent the standard deviations. The dashed rectangles highlight the regions used for mPSD calibration. The correspondence of the regions to the study cases in Table 5.2 is indicated on the right side. The columns in Figure 5.2 represent the results for each scintillator in the mPSD.

Sample size

Figure 5.3 shows the influence of the training sample size on the models' performance. The solid lines are the relative median deviations from the expected TG-43 U1 dose [46] obtained with the random forest, linear regression, and ANN algorithms. The shaded regions represent the ranges of deviations between the median deviations and the median deviations plus the standard deviations. We created Figure 5.3 based on the deviations obtained at all distances to the source for study case 2 in Table 5.2. The relative deviations for training done with fewer than 100 dwell positions resulted from calculations done 150 times each.

Overall performance

Table 5.3 summarizes the performance of the different models used for mPSD dose prediction. We rated the models as advantageous (++), good (+), or inconvenient (-). To evaluate each model's performance, we took into account different criteria. First, we considered the dose measurement accuracy, which we evaluated using the expected TG-43 U1 dose [46] as a reference. Additionally, we considered the implementation complexity of each model to provide the reader with an overall point of comparison (interpretability of the trained model, degrees of freedom, training process, and sensitivity to metaparameters adjustment). Table 5.3 also shows each model's performance for a small training set with the intent of evaluating the extent of the required user's expertise in mPSD manipulation to obtain accurate results with each model analyzed.

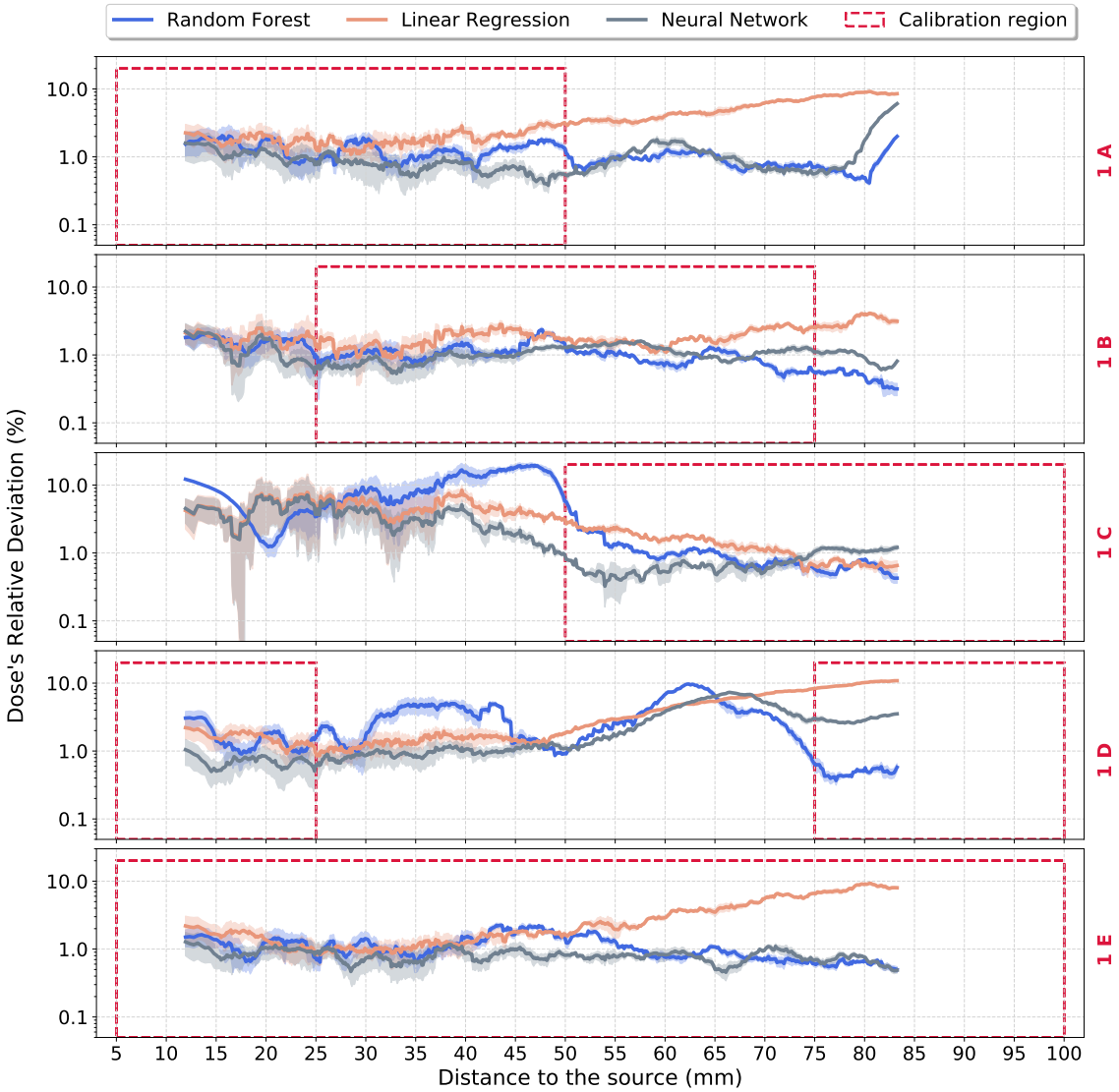

Figure 5.2 – Influence of the calibration region on the dose prediction model.

5.6 Discussion

In this study, we evaluated the feasibility of ML algorithms for mPSD calibration in HDR brachytherapy. The overall models' deviations from the expected doses generally remained below 20 %. In agreement with the observations previously [30], the dose prediction accuracy and measurement uncertainty were dependent on the calibration conditions and dose prediction model. We observed the best accuracy for calibrations done in study case 1E (Table 5.2), in which we used the measured data covering the whole range of distances explored to extract the calibration factor for signal translation into the dose. However, when considering only a portion of the data (i.e., study cases 1A-D), we found the best agreement in study case 1B. In this case, the linear regression model resulted in median dose deviations smaller than 7 %. The study done by Linares Rosales et *al.* [30] also explored the dose agreement with TG-43 U1 [46] over distances to the source ranging from 5 to 65 mm. At 65 mm

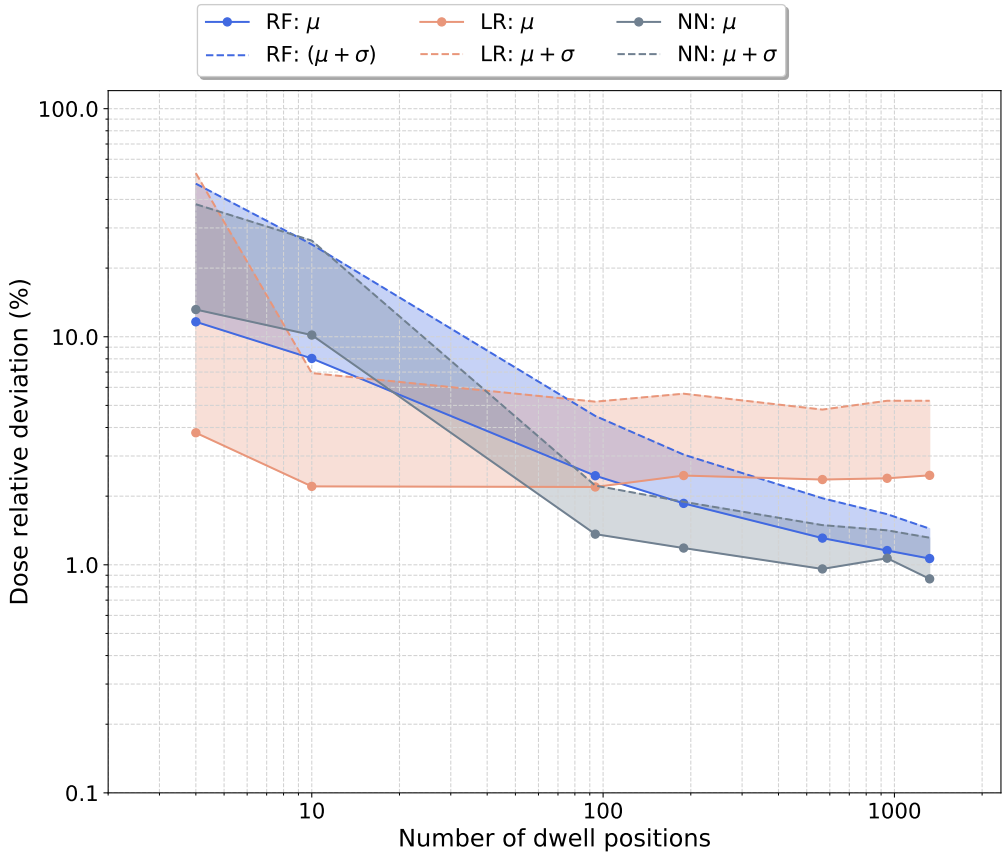

Figure 5.3 – Influence of the training sample size on the dose prediction model.

from the source, they observed relative deviations of 21.3 %, 12.4 %, and 13.7 % for the BCF-10, BCF-12, and BCF-60 scintillators, respectively. In the present study, the dose agreement with the expected TG-43 U1 dose was superior to the findings in [30] due to optimal selection of the calibration conditions. On the other hand, the selection of data for study case 1C or 1D for calibration purposes led to increased deviation at short distances to the source. This effect was most pronounced while using region 1C, where deviations could reach 11 % relative to the TG-43 U1 reference dose. Based on the findings shown in figure 5.2, we recommend the use of data at distances from the source ranging from 25 to 75 mm (region 1B) for model training and mPSD calibration. When using this region, the relative dose deviation obtained with the three ML algorithms remained small (0.2-4.2 %) at all of the explored distances from the source. We do not recommend using data in the source's high-gradient field for mPSD calibration because it will lead to unbalanced fitting of the dose. As a result, increased deviations at large distances from the source can be expected.

The number of available measurements for training purposes influences random forest and ANN models the most. As shown in figure 5.3, the median ($\pm$ standard deviation) dose deviation for the predictions with linear regression remained almost constant at about 2.12 % $\pm$ 3.98 % when we used at least 10 dwell positions. In principle, the linear regression model can be trained with only four dwell positions. However, the dose prediction accuracy would be highly influenced by the user's experience with mPSD technology, which could lead to poor calibration conditions. The random data selection used to create

Table 5.3 – Overall performance of the models used for mPSD calibration and dose measurement.

Criteria	Applicability	Linear regression	Random forest	Neural network
Accuracy	*inside region*	+	++	+
	outside region	+	-	-
Method implementation complexity	-	++	+	-
Performance for small training set	-	++	-	-
mPSD's manipulation: required user expertise	-	-	++	++

++, advantageous; +, good; -, inconvenient.

Figure 5.3 highlights this effect. The use of four dwell positions in the model's training could lead to dose deviations on the order of 50 % from the expected TG-43 U1 dose [46]. The results obtained with the random forest and ANN algorithms were similar. The accuracy obtained with those models begins to converge toward deviation values close to 1 % from a number of dwell positions greater than 100, which may not be feasible for clinical end users.

Table 5.3 summarizes the findings of this study. In general, the dose predictions with all three models were accurate within 7 % relative to the dose predicted by TG-43 U1 [46], when measurements are done over the same range of distances used for calibration (the *inside region* criterion in table 5.3). In such cases, the predictions with the random forest algorithm exhibit minimal deviations, but the performance is compromised for predictions made outside the calibration region. Signal spikes and abrupt signal changes in the measured dose are frequently observed with the random forest and ANN algorithms under conditions different from the calibration ones as observed in regions 1A, 1C, and 1D in Figure 5.2. The best accuracy for both inside and outside the calibration range is obtained with the linear regression model. The behaviour of the deviations along the distances to the source is smoother for linear regression than for the other two algorithms even if larger deviations are observed. This behavior reflects the well-known fact that linear regression algorithms can extrapolate data but the random forest algorithm cannot and that linear regression algorithms outperform the random forest algorithm in situations with low signal-to-noise ratios (typical of long distances to the source). Indeed, because the random forest algorithm is not a differentiable function but rather a combination of decision trees with discrete output values (in agreement with given output values in the training phase), it cannot accurately predict the dose beyond the range of the calibration region. The accuracy of the dose predictions attained with the ANN algorithm is similar to that with the random forest algorithm. A non optimal ANN architecture may explain this effect. Indeed, the ANN's internal operations, which consist of simple functions (e.g., the linear function), try to reproduce the physical system behavior by adjusting its internal weights. The difficulty when training such an algorithm is finding the optimal network architecture that will enable it to reproduce the behavior of the underlying physical system without overfitting of the dose.

Apart from the mentioned above, in selecting a proper method for mPSD dose measurement, the method implementation complexity must be considered. Interpreting the results obtained with the

linear regression model is easier than that for the ANN or random forest algorithm. These kinds of methods require fewer data than more refined models to produce acceptable results. However, more refined models, such as the random forest and ANN models, may have better performance when appropriately trained. Indeed, Figure 5.2 shows that the random forest is usually the best algorithm when the calibration region encompasses the prediction region, even if the data are randomly selected during the training process (e.g., region 1E in Figure 5.2). The last two criteria we considered in Table 5.3 were the models' performance using a small training data set and the user expertise required to manipulate the mPSD.

Although the linear regression model's median dose deviation remains relatively constant across the training sample sizes, the achieved agreement with the expected TG-43 U1 dose depends on the dwell position selected for training and calibration among other parameters. The effect of the data selections becomes critical when using four dwell positions, for instance. This is why we considered the linear regression model to be inconvenient according to the user expertise criterion. When using four dwell positions for training purposes, significant deviations are also observed with the random forest and ANN models (performance ranked as inconvenient for a small training data set) because they can incorrectly interpolate positions in regions not present in the training data set. However, as shown in Figure 5.3, at a certain number of training dwell positions, the accuracy achieved with random forest and ANN models is superior to that achieved with the linear regression model while being independent from the user expertise in selecting the appropriate dwell position.

Given the results described herein, taking a large number of dose measurements in a clinical environment may be considered time-consuming. Nevertheless, for example, setting 200 dwell positions for training purposes with dwell times of 1 s each represents about 3.33 min of irradiation. The time-consuming factor associated with this process is setup of the experiments, meaning mPSD and catheter positioning to ensure TG-43 U1 conditions, connecting transfer tubes and double-checking verification to ensure lack of a catheter swap, and correcting catheter shifts. This process takes several minutes and must be optimized to reduce the time it takes.

Conclusions

In this study, we evaluated the benefits and limitations of using linear regression, random forest, and ANN algorithms for mPSD calibration in HDR brachytherapy. The drawback of these methods is the need to calibrate the detector at many locations relative to the source, which may result in a relatively long calibration time. The main benefits of using the models described herein are that calibration must only be done once for each detector and that the pretrained models' files can be distributed for mPSD implementation in brachytherapy clinics. Finally, our results suggest that the random forest algorithm has the best performance of the three algorithms tested when the data from the training region cover the prediction region. We also recommend using training data with the measurements in at least 100 dwell positions. In such cases, agreement 7 % with the expected TG-43 U1 dose is ensured with all the algorithms, and selection of the calibration dwell positions becomes less dependent on the user's expertise.

Acknowledgements

This work was supported by the National Sciences and Engineering Research Council of Canada via National Sciences and Engineering Research Council of Canada-Elekta Industrial Research Chairs grants 484144-15 and RGPIN-2019-05038 and by Canadian Foundation for Innovation John R. Evans Leaders Fund grant 35633. HMLR further acknowledges support from Fonds de Recherche du Quebec - Nature et Technologies and by CREATE Medical Physics Research Training Network grant 432290 from the Natural Sciences and Engineering Research Council of Canada. We also thank Donald R. Norwood from Scientific Publications Services in the Research Medical Library at The University of Texas MD Anderson Cancer Center for editing our manuscript.

Chapter 6

From conception to clinical trial: IViST - the first multi-sensor-based platform for real-time In Vivo dosimetry and Source Tracking in HDR brachytherapy

Haydee M. Linares Rosales[1,2], Audrey Cantin[2], Sylviane Aubin[2], Sam Beddar[3,4], Luc Beaulieu[1,2]

[1]Département de physique, de génie physique et d'optique et Centre de recherche sur le cancer, Université Laval, Québec, Canada.

[2]Département de radio-oncologie et Axe Oncologie du CRCHU de Québec, CHU de Québec - Université Laval, QC, Canada.

[3]Department of Radiation Physics, The University of Texas MD Anderson Cancer Center, Houston,TX, United States.

[4]The University of Texas MD Anderson UTHealth Graduate School of Biomedical Sciences, Houston, TX, United States.

6.1 Résumé

Cette étude visait l'introduction clinique de IViST (In Vivo Source Tracking), une nouvelle plateforme de dosimétrie basée sur plusieurs capteurs pour la surveillance de plans en temps réel en curiethérapie HDR. IViST est une plateforme composée de 3 grandes parties: 1) un détecteur multipoints à scintillateurs plastiques optimisé et caractérisé (3 points mPSD; en utilisant les scintillateurs BCF-60, BCF-12 et BCF-10), 2) un assemblage compact de tubes photomultiplicateurs (PMT) couplés à des miroirs dichroïques et des filtres pour la collecte de lumière à scintillation, et 3) une interface graphique basée sur Python utilisé pour la gestion du système et le traitement du signal. IViST peut mesurer simultanément la dose, trianguler la position de la source et mesurer le temps d'arrêt. En effectuant 100 000 mesures / s, IViST échantillonne suffisamment de données pour effectuer rapidement des tâches QA / QC clés, telles que l'identification d'un mauvais temps d'arrêt individuel ou des tubes de transfert interchangés. En utilisant 3 capteurs colinéaires et des informations planifiées pour une géométrie d'implant (de DICOM RT), la plateforme peut également trianguler la position de la source en temps réel. Un essai clinique est en cours avec le système IViST.

6.2 Abstract

This study aimed to introduce IViST (In Vivo Source Tracking), a novel multi-sensor-based dosimetry platform for real-time plan monitoring in HDR brachytherapy. IViST is a platform that comprises 3 parts: 1) an optimized and characterized multi-point plastic scintillator dosimeter (3 points mPSD; using BCF-60, BCF-12, and BCF-10 scintillators), 2) a compact assembly of photomultiplier tubes (PMTs) coupled to dichroic mirrors and filters for high-sensitivity scintillation light collection, and 3) a Python-based graphical user interface used for system management and signal processing. IViST can simultaneously measure dose, triangulate source position, and measure dwell time. By making 100 000 measurements/s, IViST samples enough data to quickly perform key QA/QC tasks such as identifying wrong individual dwell time or interchanged transfer tubes. By using 3 co-linear sensors and planned information for an implant geometry (from DICOM RT), the platform can also triangulate source position in real-time. A clinical trial is presently on-going using the IViST system.

6.3 Introduction

In vivo dosimetry (IVD) in BT aims to quantify in real-time the agreement between the treatment plan and delivered dose. Presently, BT clinics do not verify their treatments in real-time: (a) commercial real- time systems have small signal-to-noise ratios (SNR) (limited time resolution, large measurements uncertainties, detection of only large errors); (b) laboratory real-time systems can be cumbersome to operate (more difficult to disseminate to BT clinics and workflow); (c) detector systems do not employ sophisticated error detection algorithms, large false error rate, poor confidence in error reporting. Several studies [10, 14, 48–53] have been focused on developing detectors and methods for real-time source monitoring in BT. The advantages of using plastic scintillator detectors (PSDs) are listed in the literature [74, 75], a key one being their real-time response. Nevertheless, PSDs are affected by stem

effect and temperature variations [26,34]. The proper optimization of the optical chain combined with the implementation of mathematical methods to correct both dependencies of the detector response, the use of plastic scintillator detectors in a multipoint configuration (mPSD) is suitable for real-time source tracking in high dose rate (HDR) brachytherapy [30, 32, 120].

The main goal of this paper is to introduce IViST, as a new multi-sensor-based dosimetry platform for real-time plan monitoring in HDR brachytherapy as well as the first end-to-end application of IViST into the clinical context.

6.4 IViST as a platform

IViST is a novel platform that comprises 3 parts: 1) a 3 points mPSD, 2) a light collection system, and 3) a Python-based graphical user interface (Graphical User Interface (GUI)) used for system management and signal processing. IViST can simultaneously measure dose, triangulate source position, and measure dwell time.

6.4.1 Dosimetry system

The optimized dosimetry system consisted of a 1.0 mm-diameter core mPSD (using BCF-60, BCF-12, and BCF-10 scintillators) coupled to 15 m-long fiber-optic cable Eska GH-4001 from Mitsubishi Rayon Co., Ltd. (Tokyo, Japan). The mPSD fiber was connected to a data acquisition system consisting of a compact assembly of photomultiplier tubes (PMTs) coupled with dichroic mirrors and filters to achieve a highly sensitive scintillation light collection [30]. The scintillation light generated inside the mPSD is collected in real-time and deconvolved into different spectral bands for dose rate measurements without the contribution of the Cerenkov radiation [30, 32]. The PMTs are independently controlled from the irradiation unit and read simultaneously at a rate of 100 kHz using a data acquisition board (DAQ) type DAQ NI USB-6216M Series Multifunction from National Instruments (Austin, USA).

The thorough optimization and characterization efforts lead to the design of a first in vivo dosimetry system shown in figure 6.1. The detector was made light-tight to avoid environmental light contribution and physical damage. The mPSD's diameter allowed its insertion into a 24-cm plastic catheter (Best Medical International, Springfield, VA, USA), and is used in a supplemental catheter during measurements in HDR brachytherapy with ^{192}Ir. The light collection apparatus was enclosed into a custom-made box containing the light acquisition system as well as the DAQ. It is a passive light collection system that does not represent any electrical risk for patients. The system's dosimetric performance has been evaluated in HDR brachytherapy, covering a range of 10 cm of source movement around the sensors [30, 108]. Within a range of distances of 6 cm from the source, IViST can track the ^{192}Ir source with 1 mm positional accuracy, keeping the dose deviations from the TG43-U1 [46] expected dose smaller than 5 %. The detector further exhibited no angular dependence and the system high collection rate allows for dwell time assessment with a maximum average weighted deviation of 0.33 ± 0.37 s [108].

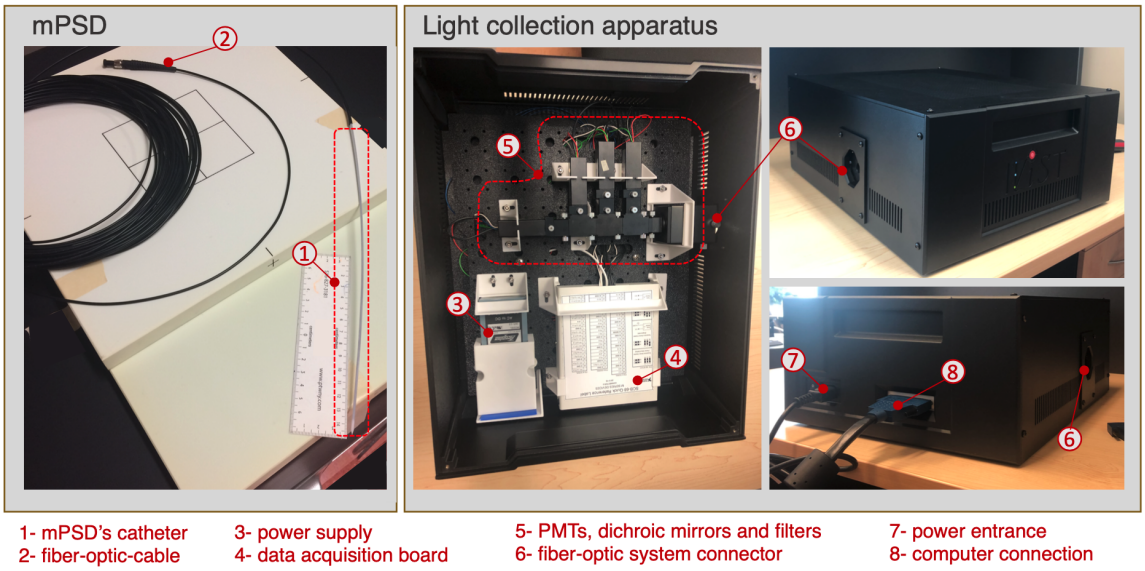

Figure 6.1 – IViST's dosimetry system. A detailed list of sub-components (e.g. filters, mirrors, PMTs) can be found in Linares Rosales et *al.* [108]

6.4.2 Graphical user interface for dosimetry system control

Figure 6.2 illustrates the graphical user interface (GUI) of the key software tools available to control the dosimetry system. The GUI was designed to allow any user an easy manipulation, without requiring a high level of expertise in the mPSD manipulation. PyQt5 was used to create the GUI. Figure 6.3 summarizes the main functionalities of the GUI and the relationship among them. The software's main windows give the user access to 2 main sections: Offline tools and In Vivo Dosimetry.

Within **Offline tools**:

- **Signal processing**: A measurement file is loaded in this module by the user. Then, the module allows for easy extraction and manipulation of the raw data previously collected. This module is crucial for future data usage during the mPSD calibration. It could also be used to extract the statistics associated with each dwell position (e.g. measured dwell time, mean raw signal, mean dose per dwell).
- **System calibration**: The module receives a measurement data set, and based on TG43's expected dose, generates the calibration models for raw signal translation into a dose value. Among the main features of this module, it allows for dose prediction with the hyper-spectral approach proposed in [32] as well as a Random Forest algorithm and Neural Network.
- **Dosimetry tools**: Performs the dosimetric analysis of the collected data. The user could, for instance, verify the agreement of the measured dose with that expected from TG43 and calculate the source position for the measured plan. The module also includes a catheter shift correction feature.

The In Vivo Dosimetry module contains the tools used for real-time data acquisition:

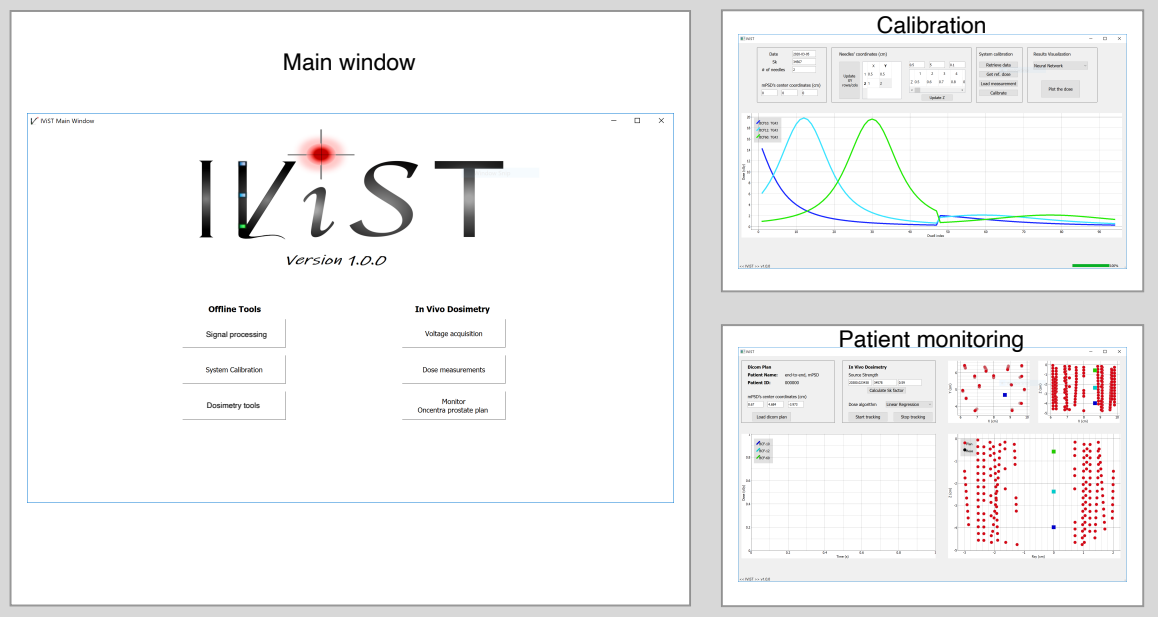

Figure 6.2 – IViST's graphical user interface. Illustration of some of the available functionalities.

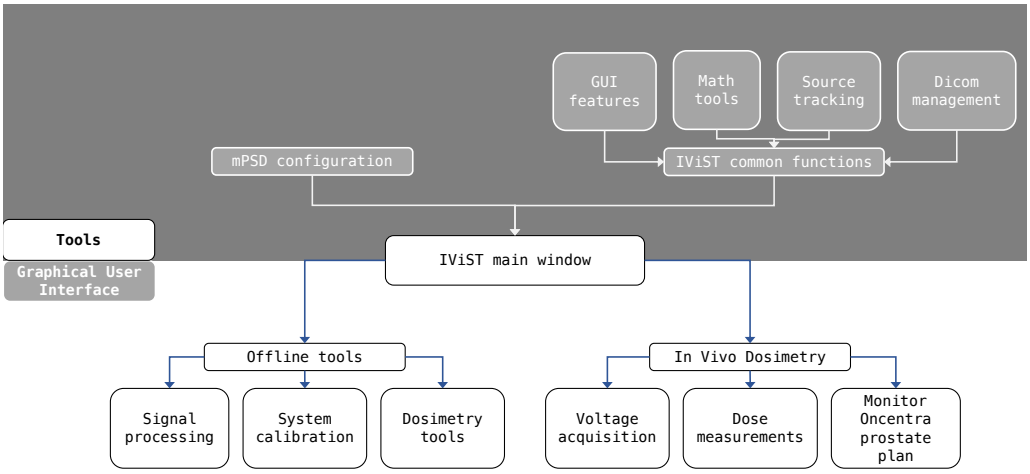

Figure 6.3 – IViST's code's diagrams.

- **Voltage acquisition**: Collects the raw measurement data from PMTs in volts.
- **Dose measurement** is similar to the **Signal processing** module, excepting that a calibration data file has to be available in advance to allow for real-time signal translation into absorbed dose.
- **Monitor Oncentra prostate plan**: Performs real-time tracking of a patient plan created in Oncentra Prostate. The module reads the plan data contained in the **.cha* files exported from the TPS, sets the treatment data as reference and monitors the patient plan in real-time. The system should be calibrated in advance. The GUI allows for real-time visualization of the measured dose at the mPSD location as well as the source location.

6.5 In vivo measurements for a prostate treatment: First Patient Measurements

In vivo dose monitoring was carried out for a prostate case as part of an ongoing clinical trial. Seventeen treatment catheters were positioned and reconstructed to deliver 15 Gy of dose in a fraction. An additional catheter devoted to measurements with the mPSD was introduced in the prostate volume. The mPSD's catheter was also reconstructed, but it was not used during the dose optimization process in the treatment planning system.

Figure 6.4 shows the heat map of deviations obtained between the planned source dwell positions and the results from the triangulation with the mPSD. The x-axis corresponds to the dwell position index, while the y-axis corresponds to the treatment catheter number. Catheter 8 is not plotted because it corresponds to the catheter dedicated to measurements with the mPSD. In total, 168 source dwell positions were tracked. As can be observed in figure 6.4, in most of the cases, the radial deviations remain below 3 mm. However, there are some dwell positions with deviations reaching 9 mm. This effect could be explained by the small source dwell times, 0.1 s (resultant from the dose optimization process), programmed at dwell-positions. Figure 6.5 presents the observed radial deviations as a function of the delivered dwell times for BCF10, BCF12, BCF60 sensors as well as for the mPSD's triangulation results. For dwell times of 0.1 s, radial deviations in the order of 4 mm were observed. IViST's data is collected at a rate of 100 kHz but averaged each 0.1 s. Thus a dwell time of 0.1 s makes almost impossible to distinguish one single dwell position from the previous/subsequent one, leading to a failed triangulation for those locations. However, for any dwell-time of 0.5 s or more, the average deviation is 2.17 ± 1.15 mm.

Figure 6.6 shows the mean deviations between the measured dwell times for our mPSD system and the planned ones. The measured dwell times at all the distances to the source were in agreement with the planned dwell time to better than 0.17 s . The overall average difference obtained was 0.06 ± 0.04 s. Larger deviations were observed for dwell positions with dwell times inferior to 0.5 s, especially for those positions at long distances from the scintillators' effective volumes. Even though the longest mPSD-to-source distance measured for this clinical case was 55 mm, the high gradient field characteristic of the ^{192}Ir source allowed to us obtain a sharp pulse of signal and, as a consequence, proper differentiation of the signal from one position to the subsequent one. As similar dwell time analysis was done by Linares Rosales [108] et *al.* through in-water measurements during HDR brachytherapy. They reported a

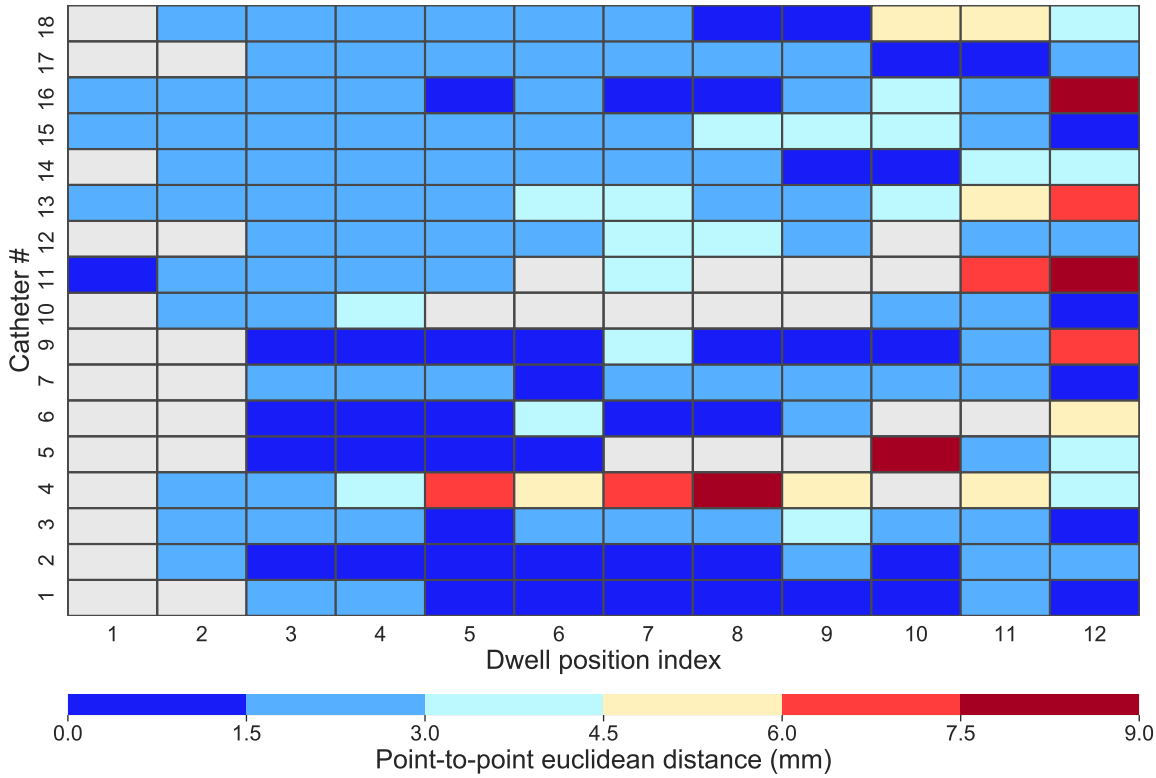

Figure 6.4 – Source position triangulation results. Heat map of deviations between the planned position and the triangulated one in a 3D space. The cells in gray correspond to non-programmed dwell positions.

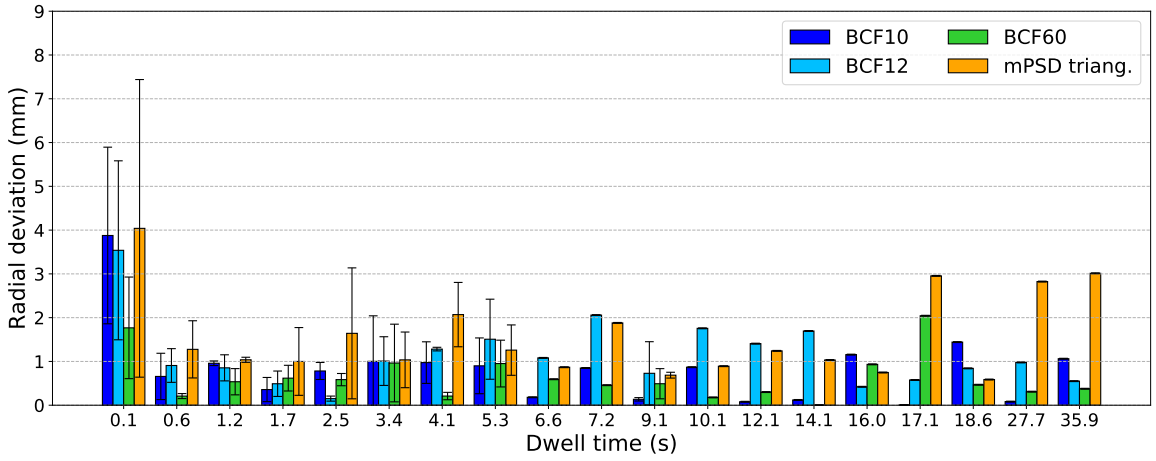

Figure 6.5 – Scintillator deviation of the expected source-to-dosimeter radial deviations as a function of the source planned dwell time.

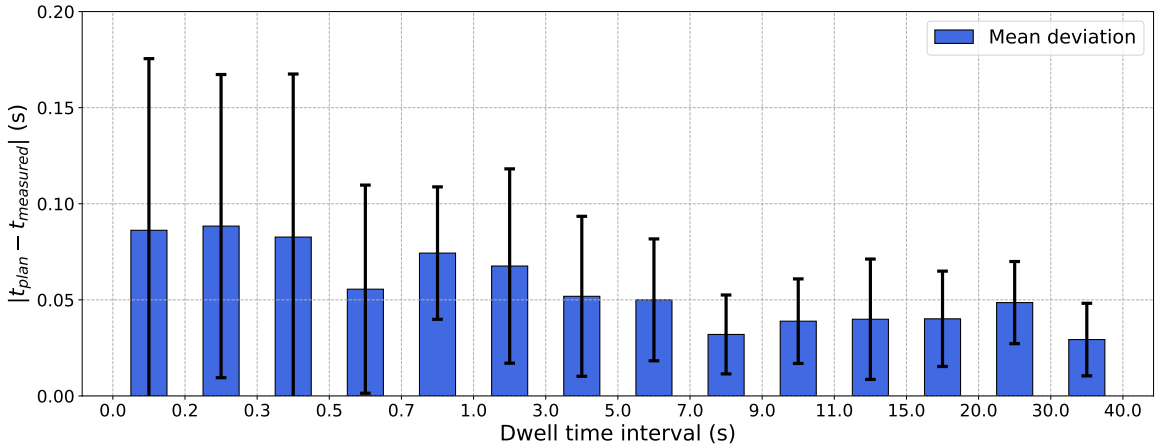

Figure 6.6 – Deviation of mPSD measured dwell times from planned dwell times as function of planned dwell-time intervals.

maximum deviation of 0.33 ± 0.37 s for a range of mPSD-to-source distance up to 10 cm. However, for the same range of distance explored in this paper, the results are equivalent [108].

6.6 Conclusions

A novel, multi-sensor dosimetric system was optimized for HDR brachytherapy in vivo dosimetry and enabled measurements over a wide range of clinically relevant dose rates. The system presented allows real-time dose, source position and dwell-time measurements. It has numerous potential in vivo QA/QC applications beyond the currently available commercial dosimeters and build on its widely-known intrinsic energy independence and water equivalence properties. The first clinical in vivo case measured with IViST has been presented here and the clinical trial is on-going.

Acknowledgements

This work was supported by the National Sciences and Engineering Research Council of Canada (NSERC) via the NSERC-Elekta Industrial Research Chair grant # 484144-15 and RGPIN-2019-05038. Haydee Maria Linares Rosales also acknowledges support from Fonds de Recherche du Quebec - Nature et Technologies (FRQ-NT).

Conclusions

The role of IVD in routine brachytherapy practice is crucial, as it is the only way to confirm in real time the dose delivered to the tumour and organs at risk. The clinical implementation of IVD requires a robust dosimetry system, i.e., small detectors with high SNR, minimally intrusive to the patient, fast and reliable, which provide real-time dose readout. Using any detector implies appropriate knowledge of its characteristics, behaviour, and range of applicability. An mPSD for in vivo HDR brachytherapy purposes was developed in this Ph.D. project. This section summarizes the results and key findings of this research project, covering the outcomes that range from the design and conception of the mPSD system to its introduction to the clinical setting for a technology clinical trial.

Return on the project's objectives

Table 7.1 presents a summary of the key results obtained during the development of the current Ph.D. project. The results are presented according to the specific objectives set in Chapter 1. Column number two in table 7.1 refers to the main aspects we targeted in each objective. Columns three and four show the key results obtained and the chapter presenting them for cross-reference in this document. Fields containing a check-mark instead of quantitative value, refer to the achieved task.

All the objectives established in this Ph.D. project were completed. Nevertheless, the objective 6 remains open for future investigations to complete the portrait started in this thesis project.

Table 7.1 – Summary of the Ph.D. key results per specific objective.

	Specific Objective	**Target**	**Key Results**	**Chapter**
1.	Design, build, optimize and characterize the response of a mPSD	**a.** mPSD to fit into a treatment needle	✓	2
		b. no external light contribution	✓	2

Continued on next page

Table 7.1–Summary of the Ph.D. key results per specific objective.

	Specific Objective	Target	Results	Chapter
		c. balanced scintillation light emission	optimal detector: BCF10: 3 mm, proximal position BCF12: 6 mm, central position BCF60: 7 mm, distal position	2
2.	Design and optimize the mPSD's light detection system	**a.** maximize the light collection	✓	2
		b. fast, stable and reliable response	collection rate 100 kS/s	3 - Annexe A
		c. minimize the contribution of elements generating spurious light	✓	2
		d. high SNR	SNR > 5 ^{192}Ir: 6 mGy/s , ^{169}Yb: 2 mGy/s	2, Annexe A
3.	Complete dosimetric characterization and assessment of the mPSD's system performance under HDR brachytherapy conditions.	**a.** angular dependence verification	10° - 170° range ΔDose $\leq 2\%$	3
		b. quantify contribution of positioning and measurement uncertainties	$U_M < 20\%$, *Sweet spot*: BCF10: 17.2 mm BCF12: 17.4 mm BCF60: 17.5 mm	3
		c. enable real-time verification of dose, source position and dwell time	✓	3
4.	Quantify the advantages and limitations of the use of different methods for mPSD's calibration.	**a.** enable the use of different algorithms for mPSD's calibration	✓	5

Continued on next page

Table 7.1–Summary of the Ph.D. key results per specific objective.

	Specific Objective	Target	Results	Chapter
		b. accurate dose prediction as a function of measurement database needed (sample size) for mPSD calibration	Linear Regression: 4 dwell positions - ΔDose $\leq$ 5% Random Forest, Neural Network: $\geq$100 dwell positions - ΔDose $\leq$ 2%	5
		c. selection of the distance to the source for mPSD calibration	25 - 75 mm range, for a source movement up to 100 mm around the mPSD	5
5.	Develop and test an algorithm for real-time source tracking and dwell time measurements in HDR brachytherapy.	**a.** dose measurement agreement with TG-43 U1 within 10 %	5%	3, 4, 6
		b. source position determination with 3 mm positional accuracy	distances $\leq$ 60 mm: 1 mm distances $>$ 60 mm: 2 - 3 mm	3, 4, 6
		c. dwell time assessment with 1s measurement accuracy	$<$ 0.4 s	3, 6
6.	Translation of the developed mPSD's system in the clinical setting for a technology clinical trial	**a.** develop a GUI for user interaction and management of the measurement's acquisition system.	- easy manipulation and interpretation of the results - independence of the treatment delivery unit	6
		b. biomedical electrical test and inspection	✓	Annexe C
		c. introduce the system to the clinical staff	✓	

Continued on next page

Table 7.1–Summary of the Ph.D. key results per specific objective.

Specific Objective	Target	Results	Chapter
	d. approval of ethics committee	✓	
	e. in patient real-time measurements	✓	6

Key findings

In this thesis, we optimized an mPSD system that can be used clinically in HDR brachytherapy. The signal analysis demonstrated that the scintillator with the shorter wavelength should be placed closer to the photodetector. The scintillator with the longer wavelength should be placed in the distal position. Because of the Stokes shift, the absorption spectrum always has a lower wavelength range than the emission spectrum. If the latter configuration is not used, inter-scintillator excitation and self-absorption effects can take place. As a consequence, the light transmission through the collecting fiber is not optimal. Thus, for a three points mPSD consisting of the scintillators BCF10, BCF12 and BCF60, BCF10 should be placed at the proximal position, BCF12 in the center and BCF 60 at the distal position. The scintillation light emission per millimeter of scintillator was more efficient in BCF10 than in BCF12 or BCF60 scintillators. The best prototype used 3 mm of BCF10, 6 mm of BCF12, and 7 mm of BCF60. Those dimensions were determined not only based on light emission balance but also to improve the detector's spatial resolution. The optimized luminescence system allowed for signal deconvolution using a multispectral approach, extracting the dose to each element while taking into account the Cerenkov stem effect. The global performance of the optimized system was evaluated in HDR brachytherapy simulations. In most of the explored conditions, the system provided a signal that is distinguishable from the background, i.e., SNR > 5 and SBR > 2.

An exhaustive analysis of the optimized system's dosimetric performance in HDR brachytherapy was carried out. Previous studies to this thesis explored the angular dependence of the scintillators BCF10, BCF12, BCF60 in a single point configuration [81,103–105]. For PSDs in a single point configuration, the main factor influencing the angular dependence of the scintillators is the stem effect, hence the importance of their removal [81]. In a multipoint configuration, we found that not only the stem effect has to be accounted for, but there is also a component of cross re-excitation of the scintillators that can cause deviations in the detector's response in the order of 10 %. Thus, to prevent this effect, a bandpass filter has to be coupled to the scintillators. This hypothesis was tested using a 400 to 600-nm bandpass filter coupled to the BCF60 sensor. BCF60 is the scintillator that produces the least amount of direct scintillation light at a large angle (farthest from the source), thus the most susceptible to excitation by the other two scintillators. After this simple addition to the system, the system responses was essentially flat (within 2%) at all angles.

We further evaluated the influence on the mPSD response of the positioning and measurement uncertainties. In agreement with Andersen et *al.* [8], we observed that positioning uncertainty dominates

in measurements made close to the source, whereas measurement uncertainty dominates at large distances. However, although the light produced by the scintillators in the mPSD was subject to multiple optical filtrations, the measurement uncertainty remained low at the largest distances relative to the results reported by Andersen et *al.* [8]. For example, a maximum measurement uncertainty of 17 % was observed for the BCF60 scintillator at 10 cm from the source. Based on the uncertainty chain, the best compromises between positioning and measurement uncertainties were reached at 17.2 mm, 17.4 mm, and 17.5 mm for the BCF10, BCF12, and BCF60 scintillators, respectively. The uncertainty in the expected dose U_{TPS} was solely accounted for by the positioning uncertainty. AAPM Task Group 138 and GEC-ESTRO [102] reported that the expanded relative propagated uncertainty (k = 1 or 68% confidence level) for a dose at 1 cm of high-energy brachytherapy sources along their transverse plane was 3.4%. This uncertainty would compound with U_C to complete the error chain. These distances represent the best compromise between mispositioning and measurement uncertainty for the mPSD system under evaluation. Of course, U_C is specific to the detector used in this case, to each sensor of the multipoint dosimeter. Such analysis should be performed as a standard of practice when reporting the performance of an in vivo dosimeter owing to the strong distance dependence displayed in brachytherapy.

The results exposed for source tracking are encouraging. At the beginning of this Ph.D. project in 2015 we set as the goal the development of a system capable to: (a) perform real-time dose measurements in agreement with TG43 U1 [46] within 10 %; (b) report a source position with 3 mm positional accuracy; and (c) measure the source dwell time with 1s measurement accuracy. However, as evidenced through the current document, we can track the source position with 5 % of dose agreement with TG43 U1, 1 mm positional accuracy for distances to the source up to 60 mm and 2-3 mm accuracy beyond 60 mm, and measure the source dwell time with deviations below 0.4 s from the planned value. It is important to emphasize that in this work the accurate determination of the position of each sensor in the mPSD was part of the calibration process. Furthermore, the expected dose values used were calculated by considering each scintillator as a volume, not as a single point in space. As such, the source position determination and the measurement of the source dwell times resulted in being highly influenced by the increase of the measurement uncertainty in combination with reduced accuracy of the dose prediction models with distance in those measurement conditions, rather than the high-dose gradients. Finally, we must underline that the system is unable to reliably perform measurements beyond a distance of 10 cm from the source. Thus, for clinical applications, we should ensure that most of the dwell positions are within 60 mm from the mPSD. This condition corresponds to the majority of clinical, especially prostate cases.

The mPSD developed in this project, where all sensors are located in a single line, is subjected to degeneracy for the source position predictions in the mPSD radial direction. By combining the mPSD and another dosimeter (here a CsI:Tl based ISD system), we broke the degeneracy in the detectors' radial direction, enabling a determination of the source location in 3D space. The inclusion of the measurement uncertainty in the source location calculation leads to improved position estimation accuracy. The in-water measurements using an HDR prostate plan configuration demonstrated the effectiveness of mPSD-ISD combination for measurements in a range of distances to the source with clinical relevance. In such a set-up, we recommend the positioning of one sensor close to the center of the prostate volume and the other outside of it. The positioning should ensure a non-symmetrical distribution of the treatment needles around the sensors. This would allow the real-time detection of

positioning errors with a high rate of accurate classification, keeping the false alarms rate low.

The calibration of the mPSD is a task to be performed with care. This process demands a level of expertise in the field that could represent a constraint for clinical implementation and daily usage of the system. We evaluated the benefits and limitations of using linear regression (the current approach used in our research group), random forest, and neural network algorithms for mPSD calibration in HDR brachytherapy. The drawback of these methods is the need to have a hundred or more dwell positions to reliably calibrate the system, which may result in a long calibration time and be unrealistic in a clinical setting. The main benefits of using the models described herein are that calibration must only be done once for each detector and that the pre-trained models' files can be distributed for mPSD implementation in brachytherapy clinics. Random forest algorithm has the best performance (dose deviations < 2 %) of the three algorithms tested when the data from the training region covers the prediction region. However, the performance of random forest was compromised when the predictions were made beyond the range of calibration distances. Because the linear regression algorithm can extrapolate the data, the dose prediction by the linear regression was less influenced by the calibration conditions than random forest. The linear regression algorithm's behavior along the distances to the source was smoother than those for the random forest and neural network algorithms, but the observed deviations were more significant than those for the neural network and random forest algorithms. The findings of this study suggest the use of training data with the measurements in at least 100 dwell positions within a 25 - 75 mm range of distances from the source. In such cases, agreement 7 % with the expected TG-43 U1 dose is ensured with all the algorithms, and selection of the calibration dwell positions becomes less dependent on the user's expertise.

The mPSD system developed during this project is the only system that can provide simultaneous real-time monitoring of the source dwell position, dwell time and dose delivered in HDR brachytherapy. Therriault-Proulx et al. [9] used a multipoint configuration and a weighted approach to report the overall offset between the expected and calculated positions of the ^{192}Ir source. Although this weighted offset improved their source-position detection, offsets greater than 2.5 mm were reported, limiting HDR brachytherapy measurements to a range within 3 cm of the source. Johansen et *al.* [10] used a single point detector composed of a radioluminescent crystal of Al_2O_3:C to track the source position during prostate HDR treatments. They found an average dose agreement with the TG43 U1 expected dose of -4.66 $\pm$ 8.40 %. However, the use of a single detector leads to a sphere of probable locations around the sensitive volume. Moreoever, the accuracy of the catheter reconstruction process critically depends on having at least three dwell positions for a given catheter. Guiral et *al.* [12] used 4 GaN-based dosimeters inserted into a gynecological multichannel applicator during HDR brachytherapy source tracking. A dwell time agreement of 0.05 $\pm$ 0.09 s with the plan was reported. Also, the source dwell positions were found within 0.11 $\pm$ 0.70 mm agreement. The experiments in [12] were done for a 24 dwell-position protocol with a 5 s dwell time covering 60 mm of distances to the source. However, in comparison with the current study, the authors in [12] only explored performance for long dwell times with a shorter range of source displacements and for dwell stepping of 2.5 mm (compared to 1 mm in our study), all leading to more pronounced dose gradient between 2 subsequent dwell positions, and as a result, an easier detection. For clinical applications, dwell-times below 5 s are frequent and most clinic will allow values down to 0.5-1.0 s. Finally, the use of flat panel detectors turns out to be suitable for source position tracking and dwell times assessment, but dose measurement has not been demonstrated convincingly for this technology. Differences below 2 mm from the planned position [11, 14] and 0.2 s

from the expected dwell time [14] were reported. However, its response is limited by the 2D nature of the comparison of planned and measured positions. Although some situations can be contrived where the system may have trouble distinguishing between catheter positions (where two catheters are aligned one above the other and project on to the detector as one), this is unlikely in the prostate brachytherapy clinical situation. Furthermore, flat panels are suitable for the pretreatment verification except for the acquisition rate that is not sufficient to measure small dwell times in the order of 0.2 s in HDR treatments [14].

The findings of this project led to the conception of a standalone system, IViST, and its translation to the clinical practice as part of a technology clinical trial. IViST stands for **I**n **Vi**vo **S**ource **T**racking. IViST is a platform comprised of three key parts: 1) a multi-point plastic scintillator dosimeter, 2) a compact assembly of photomultiplier tubes coupled to dichroic mirrors and filters enclosed into a custom-made box to preserve the optical chain stability and easy manipulation, and 3) a Python-based graphical user interface used for system management, data acquisition and signal processing. IViST can simultaneously measure dose, triangulate source position, and measure dwell time. By making 100 000 measurements/s, IViST samples enough data to quickly perform key QA/QC tasks such as identifying wrong individual dwell time or interchanged transfer tubes. CHU de Québec - Université Laval brachytherapy medical physics team has now been trained to use IViST. The first clinical in vivo case measured with IViST has been presented in Chapter 6, and the clinical trial is on-going. For this first clinical implementation, we are looking at the clinical workflow for in vivo dosimetry using this technology, and the data will be used to seek optimal action thresholds.

Recommendations and continuity

The mPSD system developed during this PhD project could be used in any form of HDR brachytherapy. However, in the range of energies typical for electronic brachytherapy, the scintillators composing the mPSD suffer from energy dependence and quenching [28, 106]. In such a case, additional correction factors have to be included and will depend on changes in energy spectra with distance from the source. In HDR brachytherapy with the ^{192}Ir source, the system is well-characterized. However, for an efficient clinical implementation of IVD with the proposed mPSD (and probably most in vivo dosimeters), one needs to consider two essential aspects: dosimeter positioning and thresholds for real-time error detection.

- **mPSD positioning:** Since source tracking using the mPSD suffers from degeneracy in the radial direction, its position inside a clinical volume has to ensure a non-symmetrical distribution of catheters around it. In that way, the system can adequately identify which measured dwell position belongs to which catheter, based on the catheter reconstruction step performed during the treatment planning process. Furthermore, it provides an accurate indication of positioning errors in the case that one or more catheter swaps take place.
- **Error detection in real-time:** In this thesis, we presented results for error detection that were solely based on the metrics extracted (position deviation thresholds) from the Receiver Operating Characteristic (ROC) analysis to classify deviations as errors. The usage of position deviation thresholds should be evolutionary with the distance to the source. If the latter is

not taken into account, the influence of the measurement uncertainty can lead to the misclassification of an event into false positives/negatives. Furthermore, trusting the information for a single dwell position will probably represent an unnecessary treatment interruption. A more robust algorithm for error classification has to be considered to minimize unnecessary treatment interruptions without forgetting the clinical significance of deviations of positioning errors. A solution to reduce the number of false alarms could be the inclusion of the source dwell time measurements in combination with the thresholds based on source position deviations.

The results presented in this thesis demonstrate a significant contribution to the IVD in brachytherapy. We can expect in the near future the systematic implementation of this technique. The preclinical prototype here presented meets the existing clinical needs for which no solution was previously available.

Appendix A

Monte Carlo dosimetric characterization of a new high dose rate ^{169}Yb brachytherapy source and independent verification using a multipoint plastic scintillator detector

Gabriel Famulari[1], Haydee M. Linares Rosales[2,3], Justine Dupere[4], David C. Medich[4], Luc Beaulieu[2,3], Shirin A. Enger[1,5,6]

[1]Medical Physics Unit, McGill University, Montreal, QC, Canada.

[2]Département de physique, de génie physique et d'optique et Centre de recherche sur le cancer, Université Laval, QC, Canada.

[3]Département de radio-oncologie et Axe Oncologie du CRCHU de Québec, CHU de Québec-Université Laval, QC, Canada.

[4]Department of Physics, Worcester Polytechnic Institute, Worcester, MA, United States.

[5]Department of Oncology, McGill University, Montreal, QC, Canada.

[6]Research Institute of the McGill University Health Centre, Montreal, QC, Canada.

A.1 Résumé

Objectif : Une source d'^{169}Yb a été développé en combinaison avec un système de rotation de blindage (AIM-Brachy) pour fournir la curiethérapie avec modulation d'intensité (IMBT). Le but de cette étude était d'évaluer les caractéristiques dosimétriques de la source d'^{169}Yb avec/sans blindage en utilisant des simulations Monte Carlo (MC) et d'effectuer une vérification de dose indépendante en utilisant une plateforme de dosimétrie basée sur un détecteur multipoints à scintillateurs plastiques (mPSD).

Méthodes : Les paramètres dosimétriques TG-43U1 de la source ont été calculés à l'aide de Rapid-BrachyMCTPS. Des mesures de débit de dose en temps réel ont été effectuées dans un réservoir d'eau pour la source avec/sans blindage à l'aide d'un projecteur de source conçu sur mesure. Pour chaque position d'arrêt, le débit de dose a été mesuré indépendamment par les trois scintillateurs (BCF-10, BCF-12, BCF-60). Pour la source non-blindée, le débit de dose a été mesuré à des distances allant jusqu'à 3 cm de la source sur une plage de 7 cm le long du cathéter. Pour la source blindée, les mesures ont été effectuées avec le mPSD placé à 1 cm de la source à quatre angles azimutaux différents (0°, 90°, 180° et 270°).

Résultats : Les paramètres dosimétriques ont été tabulés pour le modèle de source. Pour la source non-blindée, les différences entre les débits de dose mesurés et calculés étaient généralement inférieures à 5%-10%. Le long de l'axe transversal, les écarts étaient, en moyenne (plage), 3,3% (0,6%-6,2%) pour BCF-10, 1,7% (0,9%-2,9%) pour BCF-12 et 2,2% (0,3%-4,4%) pour BCF-60. La réduction maximale du débit de dose due au blindage à une distance radiale de 1 cm était de 88,8%±1,2%, contre 83,5%±0,5% selon les calculs MC.

Conclusions : La distribution de dose pour la source d'169Yb avec/sans blindage a été vérifiée expérimentalement en utilisant un mPSD, avec un bon accord avec les simulations MC dans les régions proches de la source. La source d'169Yb couplée au système de blindage partiel est une technique efficace pour implémenter l'IMBT.

A.2 Abstract

Purpose: A prototype ^{169}Yb source was developed in combination with a dynamic rotating platinum shield system (AIM-Brachy) to deliver intensity modulated brachytherapy (IMBT). The purpose of this study was to evaluate the dosimetric characteristics of the bare/shielded ^{169}Yb source using Monte Carlo (MC) simulations and perform an independent dose verification using a dosimetry platform based on a multipoint plastic scintillator detector (mPSD).

Methods: The TG-43U1 dosimetric parameters were calculated for the source model using RapidBrachyMCTPS. Real-time dose rate measurements were performed in a water tank for both the bare/shielded source using a custom remote afterloader. For each dwell position, the dose rate was independently measured by the three scintillators (BCF-10, BCF-12, BCF-60). For the bare source, dose rate was measured at distances up to 3 cm away from the source over a range of 7 cm along the catheter. For the shielded source, measurements were performed with the mPSD placed at 1 cm from the source at four different azimuthal angles (0°, 90°, 180° and 270°).

Results: The dosimetric parameters were tabulated for the source model. For the bare source, differences between measured and calculated along-away dose rates were generally below 5%-10%. Along the transverse axis, deviations were, on average (range), 3.3% (0.6%-6.2%) for BCF-10, 1.7% (0.9%-2.9%) for BCF-12 and 2.2% (0.3%-4.4%) for BCF-60. The maximum dose rate reduction due to shielding at a radial distance of 1 cm was 88.8%±1.2%, compared to 83.5%±0.5% as calculated by MC.

Conclusions: The dose distribution for the bare/shielded ^{169}Yb source was independently verified using mPSD with good agreement in regions close to the source. The ^{169}Yb source coupled with the partial-shielding system is an effective technique to deliver IMBT.

A.3 Introduction

The ^{169}Yb radionuclide has been investigated as a viable source for brachytherapy applications [121–125]. Radioactive ^{169}Yb is produced in a nuclear reactor by neutron activation of ^{168}Yb and decays by electron capture to ^{170}Tm. It primarily emits photons with energies in the 50-308 keV range and has an average energy of 93 keV. The half-life of ^{169}Yb is 32.0 days, which is shorter than that of ^{192}Ir but sufficiently long for a high dose rate (HDR) temporary implant brachytherapy source. The lower energy reduces the amount of shielding required in brachytherapy suites. The ^{169}Yb source can be produced with a specific activity appropriate for HDR brachytherapy (> 12 Gy h^{-1}), due to the high thermal neutron cross section of ^{168}Yb and the availability of ^{168}Yb in enriched form in Yb_2O_3 powder.

Intensity Modulated Brachytherapy (IMBT) is a brachytherapy technique that can be delivered using a shielded applicator or source to modulate the dose distribution [126]. Static and dynamic IMBT approaches can be used to modulate the dose distribution to the shape of the tumor, reduce the dose to organs at risk, provide a method for dose escalation or allow for fewer catheters to be implanted. Recently, an ^{169}Yb source was proposed to deliver dynamic-shield intensity modulated brachytherapy [127]. The source can be combined with a rotating platinum shield inside of an interstitial catheter to produce a highly anisotropic dose distribution. Platinum was selected as the shielding material due to its high density, high atomic number, machinability and ferromagnetic properties.

Current brachytherapy dose calculations are performed according to the guidelines from the update of the American Association of Physicists in Medicine (AAPM) Task Group Report No. 43 (TG-43U1) [46]. MC simulations are widely adopted to accurately characterize the dosimetric parameters for brachytherapy sources [102]. In particular, model-based dose calculation algorithms should be adopted for accurate dosimetry in cases where heterogeneities from the shielded applicator or source have to be taken into account [128]. For IMBT treatment planning, MC-generated dose distributions are typically used as inputs for the optimization algorithm during inverse optimization [126].

Several detectors have been studied to assess the dose delivery during a brachytherapy treatment. Plastic scintillator detectors (PSDs) show promise for obtaining accurate dose measurements in brachytherapy [18, 22–24, 29]. Additionally, the use of PSDs in a multipoint configuration (mPSD) has been reported to be a suitable tool to asses the dose at multiple points simultaneously, thereby improving treatment quality and accuracy [30–33]. Among the advantages of using PSDs, we can find their high spatial resolution, linearity with dose, energy independence in the megavolt energy range, and water equivalence. However, a non-negligible fraction of the light collected by PSDs consists of Cerenkov light. Whether Cerenkov light requires removal in brachytherapy applications depends on the radioactive source used and the measurement geometry. In HDR brachytherapy with an ^{192}Ir source, Cerenkov radiation can cause significant errors in dose reporting if it is not taken into account [22, 23]. In this study, the stem effect is accounted for using the multi-hyperspectral filtering method proposed by Archambault *et al.* [32].

The purpose of this study is to evaluate the dosimetric characteristics of a new ^{169}Yb source using the TG-43U1 [46] protocol and independently verify the dose distribution with an mPSD system.

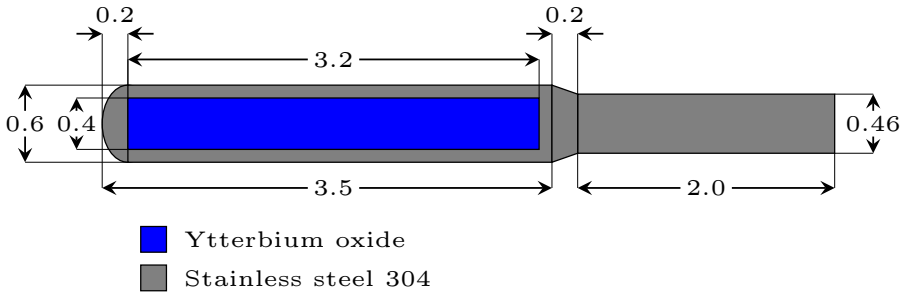

Figure A.1 – Materials and dimensions (mm) for the ^{169}Yb brachytherapy source.

A.4 Materials and Methods

A.4.1 Source characteristics

Figure A.1 shows the design of the ^{169}Yb source model (SPEC, St. Rose, LA, USA). The source has an active core which consists of Yb_2O_3 (6.9 g cm^{-3}). The active core has a diameter of 0.4 mm and a length of 3.2 mm. The active core is encapsulated in a 304 grade stainless steel cylinder (8.0 g cm^{-3}) with an outer diameter of 0.6 mm and a wall thickness of 0.1 mm. The tip of the encapsulation is a semi-spheroid (oblate) with a bisected axis of 0.2 mm and a major semi-axis of 0.3 mm. The tip is attached to a 3.2 mm long hollow cylindrical section followed by a 0.1 mm long solid cylindrical section. Following the solid cylindrical section is a conical section with a length of 0.2 mm. Attached to the conical section is a 2 mm section of a 304 grade stainless steel cable (8.0 g cm^{-3}) with a diameter of 0.46 mm.

A.4.2 Monte Carlo simulations

Simulations were performed using RapidBrachyMCTPS [129], an in-house MC code for brachytherapy applications based on the Geant4 simulation toolkit [130,131]. The decay spectrum was taken from the National Nuclear Data Centre [132]. Photons were tracked using the standard Penelope physics list with atomic deexcitation activated. Cross section data were taken from the EPDL97 [133] and EADL97 [134] cross-section libraries. Dose was approximated by collisional kerma. Collisional kerma was calculated using a tracklength estimator [135]. Consequently, electrons were not explicitly transported. Collisional kerma underestimates dose by <1% for radial distances >1 mm for typical ^{169}Yb sources [136]. Mass-energy absorption coefficients were taken from the mass-energy coefficient library present in RapidBrachyMCTPS [137].

In a first simulation, the air kerma strength per unit contained activity S_K/A was calculated in a large voxel (10×10×0.05 cm^3) at 100 cm from the source and corrected by 0.22% to give the air kerma strength at a point [136]. S_K/A was calculated in vacuum to avoid the need to correct for attenuation by air. Low energy characteristic x-rays were suppressed by discarding the contribution from photons

with energies less than 10 keV. The energy spectra of decay photons (including x-rays and gammas) and photons escaping the encapsulation were tabulated using a bin width of 0.1 keV. The photon yield was determined as the number of photons generated within the active core per decay.

In a second simulation, the source was placed in the center of a water phantom with a radius of 40 cm. The dose rate in water per unit contained activity $\dot{D}(r,\theta)/A$ was calculated in spherical shells divided in sections with a minimum resolution of 5°. The shell thickness varied with the radial distance r from the center of the active core as follows: 0.1 mm ($r \leq 1$ cm), 0.5 mm (1 cm $< r \leq$ 5 cm), 1.0 mm (5 cm $< r \leq$ 10 cm), and 2.0 mm (10 cm $< r \leq$ 20 cm). Primary and scatter separated (PSS) dose data were tabulated according to the formalism developed by Russell *et al.* [138, 139]. Along-away dose data were calculated using a grid of 1 mm^3 voxels. A total of 10^8 photons were simulated to obtain type A uncertainties below 0.2% for each simulation.

A.4.3 Experimental measurements

Dosimetry system

The dosimetry system consisted of a 1.0 mm-diameter core mPSD coupled to 15 m-long fiber-optic cable *Eska GH-4001* (Mitsubishi Rayon Co., Tokyo, Japan). The mPSD is composed by 3 mm of BCF-10, 6 mm of BCF-12 and 7 mm of BCF-60 crystals (Saint Gobain Crystals, Hiram, Ohio, USA). The size of the scintillators were optimized to balance the scintillation emission from each scintillator for optimal hyperspectral deconvolution and minimize variations in spatial resolution [30]. The mPSD's sensors and optical fiber were shielded from light using an opaque plastic tube. The outer diameter of the crystal and tube was 1.2 mm, which was thin enough to fit into most brachytherapy catheters including the plastic catheters used in this experiment. The optical fiber was connected to a data acquisition system consisting of photomultiplier tubes coupled to dichroic mirrors and filters that monitored the signal with a 100 kHz sample rate. A more detailed characterization of the mPSD system can be found in a previous study [30].

Real time dose rate measurements were performed under full scattering conditions [46]. The scintillation light generated inside the mPSD is deconvolved into different spectral bands in real time, converted to an electrical signal in the PMTs, and translated into dose rate without the contribution of the Cerenkov radiation. The mathematical formalism based on a linear regression proposed by Archambault *et al.* [32] was used as the stem removal technique. The calibration matrix and dose rate values were calculated according to the formulation published by Linares Rosales *et al.* [30] for a three-point mPSD configuration. Dose rate values provided by the scintillators were integrated over the scintillator volume to account for their finite size. A Python-based graphical user interface was used for system management and signal processing.

Dose rate measurements

Dose rate measurements were carried out using a custom-made afterloader (Worcester Polytechnic Institute and SPEC, Worcester, MA, USA). The distal end of a commercial guidewire (40 cm section)

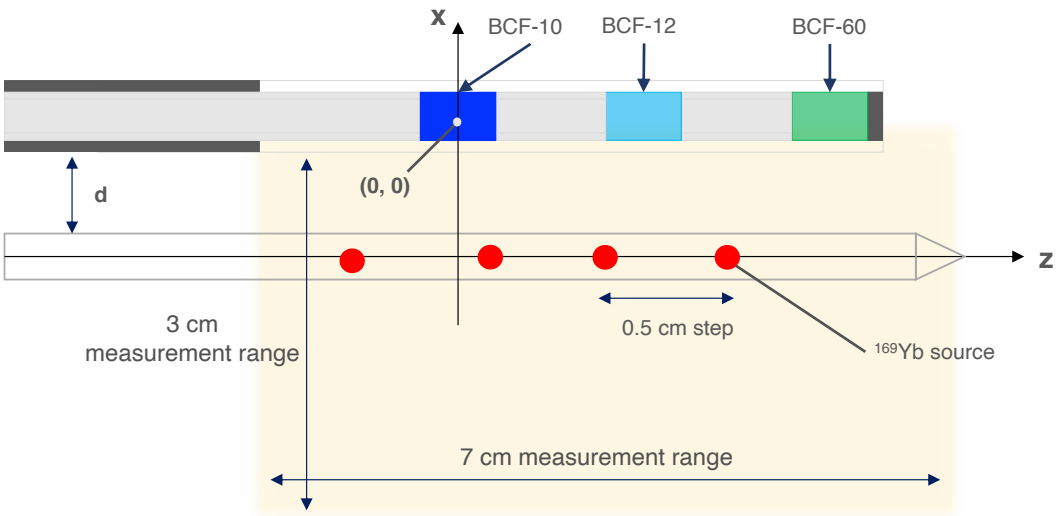

Figure A.2 – Schematic of the main parameters used for the along-away dose rate measurements from the bare ^{169}Yb source using the mPSD.

was replaced by a thinner diameter wire (0.46 mm). To ensure the accuracy and reproducibility of the source-to-detector distance, catheters were inserted into a custom-made polymethyl methacrylate (PMMA) phantom [9,30]. The phantom ensures that catheters are placed parallel to each other with a minimum spacing of 0.5 cm. The afterloader unit was able to move the source to the desired position along the catheter with a positional accuracy (k=2) within ±2 mm. The mPSD was inserted into an additional catheter for use in real-time dose verification. The light collection system was independently controlled from the afterloader unit. The source air kerma strength (S_K) was 780 U at the onset of measurements.

Figure A.2 shows a schematic of the parameters used for dose rate measurement as a function of distance to the source. Calculations were performed with a coordinate system, where the radial direction to the source is represented as x and the longitudinal direction as z. The coordinates' origin is considered at the effective center of the scintillator BCF-10. For the bare source, measurements in the x-direction were done with catheters positioned at 0.5, 1.0, 1.5, 2.0, 2.5, and 3.0 cm. In the z-axis direction, the measurements covered a range of distances of 7.0 cm. The source dwelled along each needle with a 0.5 cm step, from -1.5 cm to 5.5 cm in the z-direction. A dwell time of 1 min was programmed at each dwell position. The mPSD calibration and measurements were carried out under the same experimental conditions. The formalism proposed by Johansen *et al.* [10] was used to correct for source-to-detector positioning errors. Based on the calculated dose rate distribution, we determined the average source shifts within catheters by minimizing the chi-square between the measured dwell position and the expected one. The dose rate measured by the mPSD were compared to the MC-calculated along-away dose data as the reference.

Figure A.3 shows the setup for the dose rate measurements around the ^{169}Yb source in the presence of the platinum shield. The platinum shield was inserted into a catheter and the source was sent to a fixed position inside the shield. Measurements were taken with the mPSD placed at 1 cm at four different catheter positions, defined by their azimuthal angles with respect to the catheter containing

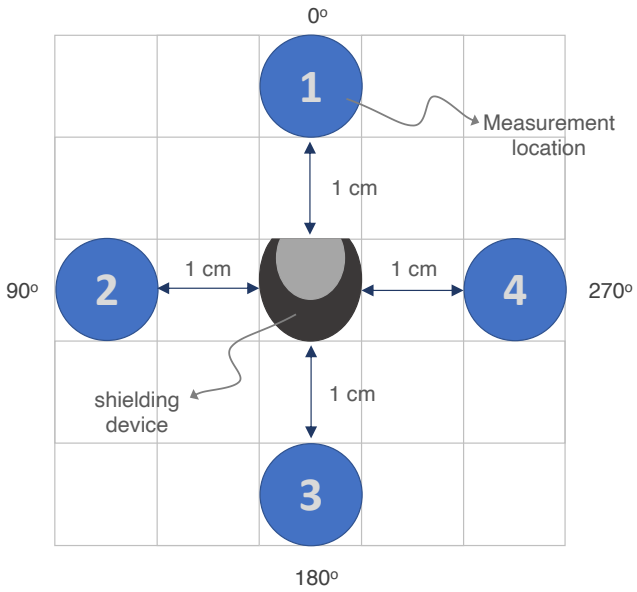

Figure A.3 – Schematic of the dose rate measurement setup around the platinum-shielded ^{169}Yb source. The mPSD was placed at a distance of 1 cm from the central catheter, containing the source and shield, at four different locations (indicated by 1-4). The source is offset from the central catheter's longitudinal axis by 0.4 mm. Figure not to scale.

the source and shield (0°, 90°, 180° and 270°). A dwell time of 1 min was programmed for each of the four positions. The dose rates measured by the mPSD were compared to MC-calculated data generated in a previous study [127] for this combined source and shield model. The dose distribution is centered along the catheter's longitudinal axis and considers a source offset of 0.4 mm.

A.5 Results

A.5.1 TG-43U1 parameters

The photon decay spectrum and photon spectrum after exiting the encapsulation are shown in Figure A.4. The average energy of the decay photons was 93.4 keV (excluding photons with energies less than 10 keV). The total photon yield from decay processes was 3.32±0.03 photons per disintegration. The average energy of the photons leaving the encapsulation was 108.8 keV. The air kerma strength per unit activity S_K/A was 1.24±0.03 U mCi^{-1}. The dose rate per unit activity $\dot{D}(r_0,\theta_0)/A$ at $r_0 = 1$ cm and $\theta_0 = 0$ was 1.50±0.03 cGy h^{-1} mCi^{-1}. The dose rate constant Λ was 1.21±0.03 cGy h^{-1} U^{-1}. Table A.1 compares S_K/A and Λ for this source model with those for other published ^{169}Yb sources.

The relative uncertainties in the air kerma strength per unit activity S_K/A, dose rate per unit activity $\dot{D}(r_0,\theta_0)/A$ at $r_0 = 1$ cm and $\theta_0 = 90°$, and dose rate constant Λ for the source model are displayed in Table A.2. Type A statistical uncertainties were 0.2% for S_K/A and $\dot{D}(r_0,\theta_0)/A$. The uncertainty due to the source geometry was determined by varying the diameter of the capsule and active core assuming a rectangular distribution over a tolerance of ±0.06 mm [102]. These uncertainties were 1.9% for S_K/A,

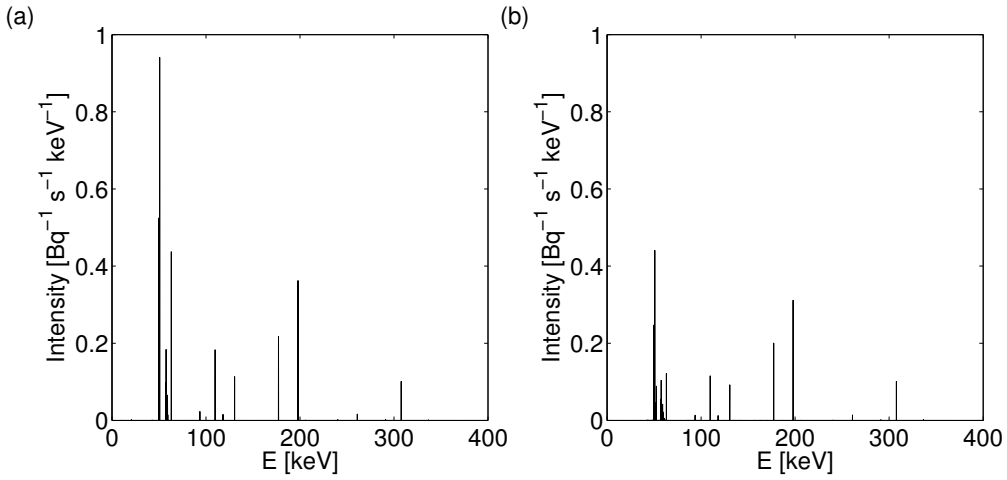

Figure A.4 – (a) Photon spectrum calculated from ^{169}Yb decay. (b) Photon spectrum exiting the stainless steel encapsulation. Photons with energies less than 10 keV were discarded. The bin width is 0.1 keV.

Table A.1 – Air kerma strength per unit activity S_K/A and dose rate constant Λ calculated for ^{169}Yb source models.

Source model	MC code	S_K/A (U mCi^{-1})	Λ (cGy h^{-1} U^{-1})
This model	Geant4	1.24±0.03	1.21±0.03
Ti capsule	MCNP5 [140]	1.15±0.03	1.19±0.03
GammaClip	MCNP5 [124]	1.37±0.03	1.22±0.03
M42	MCNP5 [123]	1.08±0.03	1.12±0.04
HDR 4140	MCNP5 [122]	1.10±0.03	1.19±0.03
Type 8	MCPT [141]		1.204±0.004
	EGS4 [142]		1.191±0.007
X1267	EGS4 [143]	1.33±0.04	1.21±0.03
	EGS4 [142]		1.17±0.01

1.6% for $\dot{D}(r_0,\theta_0)/A$ and 2.0% for Λ. The uncertainties due to the physics implementation in the radiation transport algorithm are about 0.2% [102] for high energy sources. The uncertainties in mass-attenuation coefficients (μ/ρ) and mass-energy absorption coefficients (μ_{en}/ρ) are about 0.5% [144] for photons with energies above 100 keV. The influence of the mass-attenuation coefficient uncertainties on S_K/A and $\dot{D}(r_0,\theta_0)/A$ were estimated to be no more than 0.1% [145]. The influence of the mass-energy absorption coefficient uncertainties on S_K/A and $\dot{D}(r_0,\theta_0)/A$ were set to 0.5%, since the calculations of S_K/A and $\dot{D}(r_0,\theta_0)/A$ are based on the product of photon energy fluence and (μ_{en}/ρ). The mass-energy absorption coefficient uncertainty on Λ was assigned based on the estimates from Andreo *et al.* [146] for the (water/air) ratios of mass-energy absorption coefficients. The uncertainty in the photon energy spectrum was separated into two components: the relative spectral contributions and the total photon yield per decay. The uncertainty due to the choice of photon spectrum was estimated as 0.1% [147] when total photon yield per decay is normalized to equal values. The uncertainty in

Table A.2 – Total relative standard uncertainty budget (in %) for calculation of dosimetric parameters.

Source of uncertainty	Type	S_K/A	$\dot{D}(r_0,\theta_0)/A$	Λ
Statistics	A	0.2	0.2	0.3
Source geometry	B	1.9	1.6	2.0
MC radiation transport	B	0.2	0.2	0.3
Mass-attenuation coefficients (μ/ρ)	B	0.1	0.1	0.1
Mass-energy absorption coefficients (μ_{en}/ρ)	B	0.5	0.5	0.1
Source photon spectrum	B	0.1	0.1	0.1
Photon yield	B	0.8	0.8	
Combined standard uncertainty (k=1)		**2.1**	**1.9**	**2.1**
Expanded uncertainty (k=2)		**4.2**	**3.8**	**4.2**

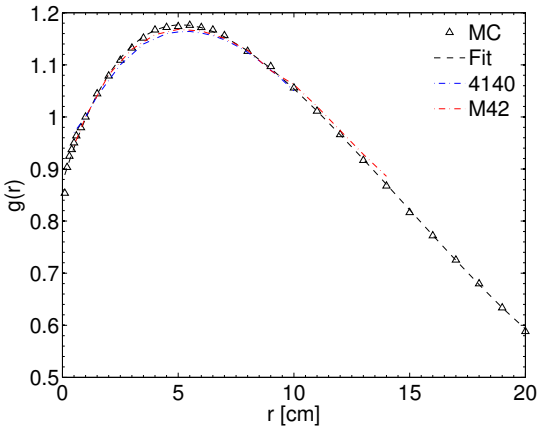

Figure A.5 – Radial dose function $g_L(r)$ calculated for the ^{169}Yb source model (L = 0.32 cm) and fifth order polynomial fit for $g_L(r)$. By definition, the uncertainty at r = 1 cm is 0. The relative uncertainty (k=1) is 2.1% otherwise. The results were compared to those for Implant Sciences Model HDR 4140 and SPEC Model M42.

photon yield was evaluated as the mean weighted uncertainty of the individual photon energies in the spectrum (0.8%) [124]. The uncertainties in photon yield largely cancel out when calculating Λ and were considered negligible. Unless stated otherwise, the uncertainties in Λ were determined using the quadrature sum of the uncertainties in S_K/A and $\dot{D}(r_0,\theta_0)/A$.

The radial dose function $g_L(r)$ based on a line source geometry function (L = 0.32 cm) is shown in Figure A.5, with a maximum of 1.176±0.035 at r = 5.5 cm. Since $g_L(r)$ is a ratio of dose rate values, a standard uncertainty (k=1) of 2.1% was conservatively assumed (similar to Λ), using a similar methodology for uncertainty propagation as Medich *et al.* [122]. The $g_L(r)$ was fitted to a fifth order polynomial function for treatment planning purposes between 0.2 cm and 20 cm:

$$g_L(r) = a_0 + a_1 r + a_2 r^2 + a_3 r^3 + a_4 r^4 + a_5 r^5 \tag{A.1}$$

where a_0 = 0.8746, a_1 = 0.1433, a_2 = -2.236×10^{-2}, a_3 = 1.364×10^{-3}, a_4 = -4.433×10^{-5} and a_5 =

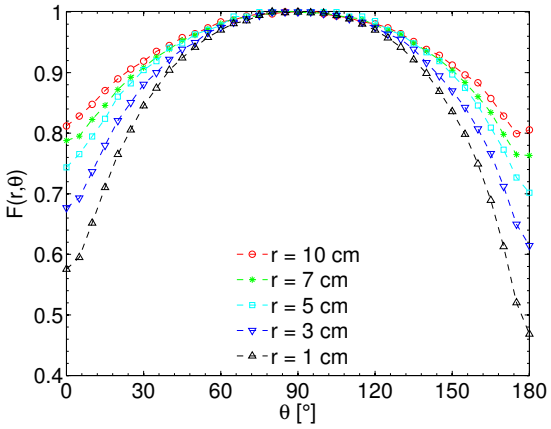

Figure A.6 – Two-dimensional (2D) anisotropy function $F(r,\theta)$ calculated for the ^{169}Yb source model. By definition, the uncertainty at $\theta = 90°$ is 0. The relative uncertainty (k=1) is 2.1% otherwise.

6.178×10^{-7} ($R^2 = 0.9981$). Deviations between fit and calculated values were within 1% over the entire range, with an average deviation of 0.43%.

The two-dimensional (2D) anisotropy function $F(r,\theta)$ is shown for a few values of r in Figure A.6 and tabulated with higher resolution in r in Table A.3. $F(r,\theta)$ ranges between 0.47 and 1.0 over all polar angles at $r = 1$ cm. $F(r,\theta)$ decreases at low polar angles, and increases with increasing distance r from the source. Since $F(r,\theta)$ is also defined as a dose rate ratio, the standard uncertainty (k=1) on $F(r,\theta)$ was estimated as 2.1%.

The PSS dose data are presented in Figure A.7. Scattered photons dominate the absorbed dose at radial distances greater than 3 cm. The majority of the dose at distances greater than 6 cm is delivered by multiple scattered photons, specifically. Since the PSS dose data is defined as a ratio of dose rate per unit of radiant photon energy, it is largely independent on photon yield, which results in a standard uncertainty (k=1) of 1.9%. The along-away dose data are shown in Table A.4. Since the along-away distribution is defined as a ratio of dose rate per unit air kerma strength, the uncertainty in Λ was adopted.

A.5.2 Experimental measurements

The dose rate measurements and relative deviations are shown in Figure A.8. The heat map colors in Figure A.8 show the dose rate distribution for each scintillator in the mPSD as a function of x and z distances. The origin of coordinates was set at the center of BCF-10 as illustrated in Figure 2. The annotated values show the measurements' relative deviations from MC-based along-away dose data at each source dwell position.

Figure A.9 shows the dose rate measured approximately along each scintillator's transverse axis (z = 0 cm for BCF-10, z = 2 cm for BCF-12, z = 3.5 cm for BCF-60). Mean differences between measured and calculated dose rates were, on average, 3.3% (0.6%-6.2%) for BCF-10, 1.7% (0.9%-2.9%) for BCF-

Table A.3 – Two-dimensional (2D) anisotropy function $F(r,\theta)$ calculated for the ^{169}Yb source model. The source tip is oriented along $\theta = 0°$. By definition, the uncertainty at $\theta = 90°$ is 0. The relative uncertainty (k=1) is 2.1% otherwise.

	r [cm]									
θ [°]	0.5	1.0	2.0	3.0	4.0	5.0	6.0	7.0	8.0	10.0
0	0.556	0.576	0.628	0.677	0.705	0.744	0.756	0.788	0.800	0.812
5	0.582	0.595	0.656	0.693	0.732	0.765	0.780	0.795	0.814	0.828
10	0.639	0.652	0.707	0.736	0.769	0.795	0.809	0.823	0.834	0.848
15	0.701	0.710	0.756	0.780	0.806	0.824	0.838	0.846	0.859	0.870
20	0.757	0.765	0.799	0.821	0.838	0.860	0.865	0.872	0.880	0.890
25	0.805	0.806	0.836	0.851	0.866	0.882	0.888	0.892	0.900	0.906
30	0.844	0.845	0.867	0.881	0.889	0.904	0.906	0.908	0.917	0.919
35	0.876	0.875	0.893	0.900	0.912	0.919	0.923	0.926	0.931	0.935
40	0.902	0.904	0.914	0.922	0.930	0.941	0.938	0.939	0.944	0.945
45	0.924	0.924	0.933	0.938	0.944	0.948	0.950	0.953	0.956	0.958
50	0.941	0.942	0.949	0.950	0.958	0.963	0.963	0.962	0.966	0.964
55	0.957	0.958	0.962	0.966	0.967	0.970	0.971	0.972	0.973	0.974
60	0.969	0.970	0.972	0.975	0.977	0.978	0.980	0.981	0.981	0.984
65	0.979	0.981	0.981	0.983	0.981	0.993	0.988	0.988	0.988	0.987
70	0.987	0.986	0.988	0.989	0.991	0.993	0.992	0.991	0.992	0.994
75	0.992	0.995	0.994	0.994	0.995	1.000	0.995	0.994	0.995	0.997
80	0.997	1.000	0.997	1.000	0.995	1.000	0.998	0.999	0.998	0.997
85	0.999	0.999	0.999	1.000	1.000	1.007	1.000	1.001	1.000	1.000
90	1.000	1.000	1.000	1.000	1.000	1.000	1.000	1.000	1.000	1.000
95	1.000	0.999	0.999	1.000	1.000	1.000	1.000	0.999	0.999	1.003
100	0.997	0.998	0.997	0.997	0.995	1.000	0.998	0.999	0.998	0.997
105	0.993	0.994	0.993	0.994	0.995	1.000	0.995	0.994	0.996	0.994
110	0.987	0.989	0.988	0.989	0.991	0.993	0.991	0.991	0.991	0.990
115	0.979	0.980	0.981	0.983	0.981	0.993	0.986	0.988	0.986	0.984
120	0.969	0.970	0.972	0.975	0.977	0.985	0.980	0.978	0.980	0.981
125	0.956	0.957	0.960	0.964	0.967	0.970	0.970	0.971	0.972	0.974
130	0.941	0.942	0.947	0.955	0.953	0.963	0.960	0.964	0.963	0.964
135	0.923	0.921	0.932	0.938	0.939	0.948	0.948	0.949	0.953	0.951
140	0.900	0.899	0.911	0.916	0.925	0.934	0.935	0.936	0.941	0.938
145	0.873	0.869	0.889	0.895	0.907	0.919	0.919	0.921	0.928	0.929
150	0.840	0.836	0.862	0.870	0.884	0.897	0.901	0.904	0.912	0.912
155	0.797	0.798	0.828	0.843	0.861	0.875	0.881	0.884	0.893	0.896
160	0.746	0.749	0.788	0.807	0.829	0.846	0.856	0.860	0.872	0.883
165	0.681	0.689	0.738	0.766	0.792	0.809	0.827	0.834	0.848	0.857
170	0.597	0.613	0.677	0.712	0.746	0.773	0.792	0.798	0.820	0.828
175	0.483	0.520	0.603	0.650	0.691	0.727	0.751	0.765	0.785	0.799
180	0.414	0.469	0.575	0.615	0.673	0.702	0.758	0.763	0.790	0.806

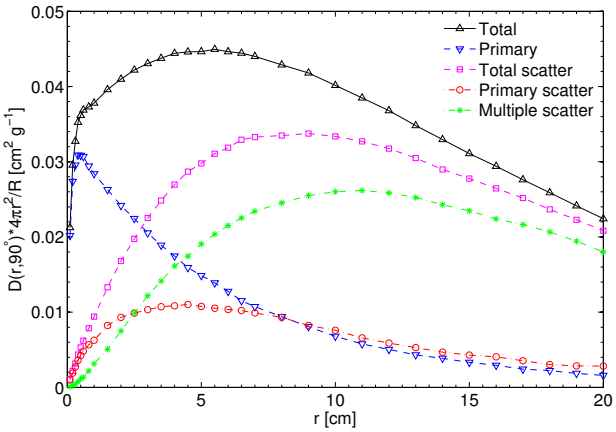

Figure A.7 – Primary and scattered separated (PSS) dose data along the transverse axis for the ^{169}Yb source model. The dose is normalized by the total radiant energy R of photons escaping the encapsulation. The relative uncertainty (k=1) is 1.9%.

Table A.4 – Along-away dose rate in water per unit of air kerma strength (cGy h^{-1} U^{-1}) calculated for the ^{169}Yb source model. The source is oriented along the z axis. The relative uncertainty (k=1) is 2.1%.

	Away x [cm]												
Along z [cm]	0	0.2	0.5	1.0	1.5	2.0	2.5	3.0	4.0	5.0	6.0	8.0	10.0
-10.0	0.011	0.009	0.010	0.009	0.011	0.010	0.011	0.010	0.010	0.008	0.009	0.007	0.006
-8.0	0.016	0.016	0.019	0.017	0.017	0.017	0.020	0.016	0.016	0.013	0.013	0.009	0.008
-6.0	0.030	0.028	0.032	0.030	0.031	0.030	0.031	0.030	0.024	0.021	0.017	0.014	0.008
-5.0	0.040	0.037	0.041	0.043	0.044	0.042	0.039	0.040	0.034	0.026	0.021	0.017	0.010
-4.0	0.059	0.058	0.063	0.069	0.065	0.061	0.062	0.052	0.043	0.033	0.027	0.017	0.012
-3.0	0.092	0.100	0.107	0.115	0.105	0.102	0.088	0.076	0.058	0.044	0.034	0.018	0.012
-2.5	0.126	0.137	0.160	0.162	0.145	0.126	0.109	0.090	0.064	0.049	0.035	0.019	0.013
-2.0	0.183	0.205	0.233	0.224	0.201	0.165	0.131	0.109	0.073	0.049	0.035	0.020	0.013
-1.5	0.290	0.344	0.394	0.362	0.282	0.215	0.162	0.126	0.081	0.055	0.041	0.020	0.013
-1.0	0.582	0.783	0.828	0.597	0.401	0.266	0.185	0.140	0.085	0.056	0.039	0.022	0.013
-0.5	2.39	3.35	2.26	0.985	0.530	0.320	0.212	0.148	0.092	0.058	0.040	0.022	0.013
-0.2	...	14.6	3.99	1.19	0.550	0.334	0.220	0.152	0.087	0.059	0.039	0.021	0.013
0	...	24.0	4.58	1.21	0.568	0.328	0.217	0.153	0.086	0.055	0.041	0.021	0.012
0.2	...	14.6	3.96	1.19	0.562	0.318	0.213	0.156	0.092	0.059	0.041	0.022	0.012
0.5	3.03	3.38	2.26	0.984	0.518	0.313	0.211	0.153	0.090	0.057	0.039	0.022	0.014
1.0	0.732	0.814	0.824	0.602	0.385	0.268	0.189	0.142	0.084	0.058	0.039	0.021	0.012
1.5	0.353	0.376	0.400	0.362	0.282	0.211	0.165	0.123	0.078	0.053	0.039	0.021	0.014
2.0	0.214	0.219	0.237	0.225	0.202	0.160	0.132	0.107	0.075	0.046	0.038	0.021	0.013
2.5	0.136	0.154	0.157	0.158	0.147	0.124	0.108	0.089	0.064	0.048	0.034	0.020	0.012
3.0	0.107	0.113	0.111	0.119	0.111	0.096	0.090	0.073	0.054	0.042	0.032	0.017	0.011
4.0	0.063	0.062	0.064	0.068	0.065	0.062	0.060	0.053	0.042	0.033	0.027	0.016	0.010
5.0	0.043	0.044	0.041	0.043	0.044	0.046	0.040	0.037	0.032	0.026	0.023	0.014	0.009
6.0	0.029	0.030	0.034	0.031	0.032	0.033	0.032	0.029	0.025	0.023	0.017	0.013	0.009
8.0	0.018	0.017	0.016	0.019	0.018	0.017	0.019	0.017	0.014	0.015	0.012	0.009	0.008
10.0	0.011	0.012	0.012	0.009	0.011	0.010	0.010	0.008	0.010	0.008	0.009	0.007	0.005

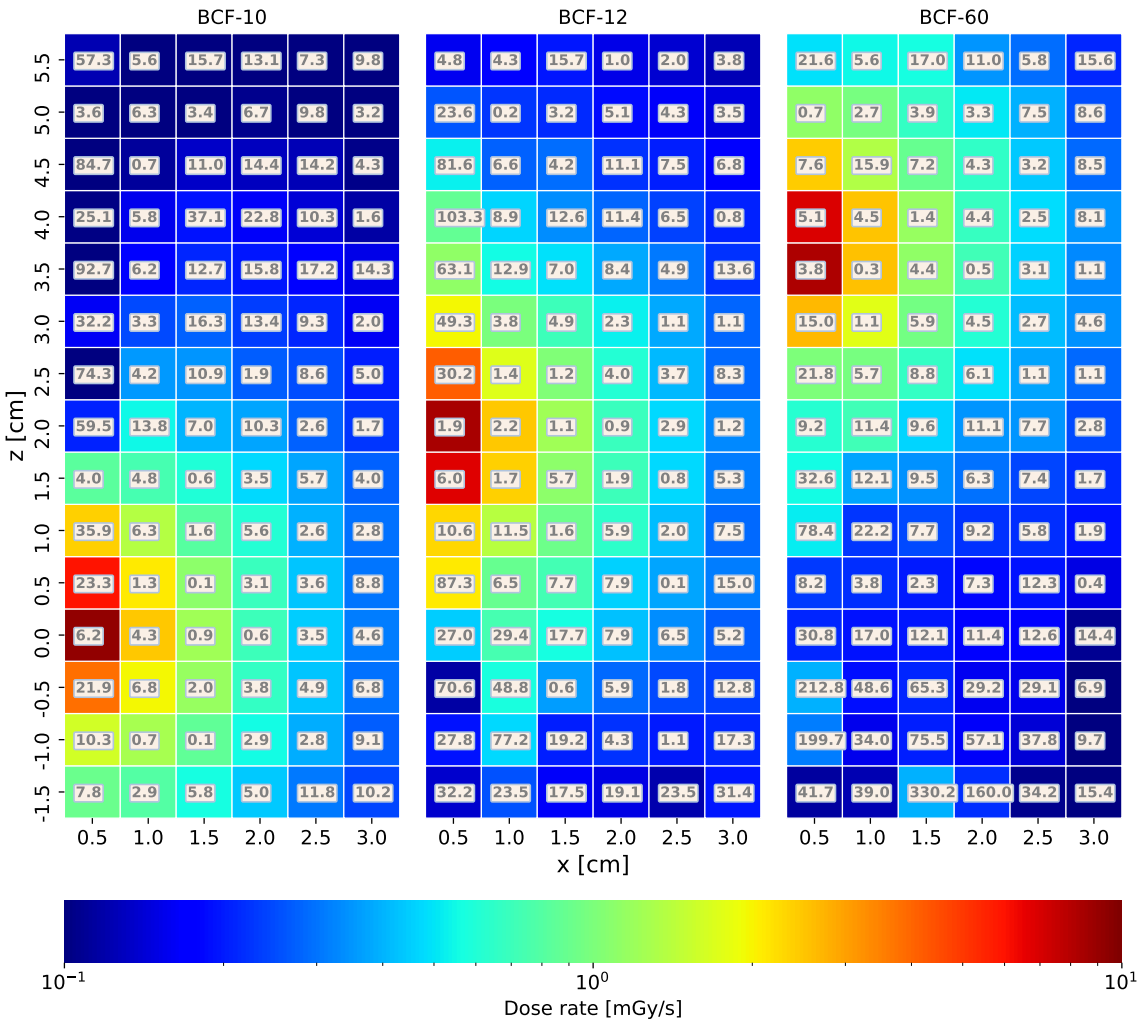

Figure A.8 – Along-away measurements of the dose rate from the bare ^{169}Yb source in a water tank (TG-43U1 conditions) using the mPSD. Relative deviations (%) from calculated along-away data indicated in boxes.

12 and 2.2% (0.3%-4.4%) for BCF-60. However, these differences were generally within their combined uncertainties. The measurement uncertainty (k=1), including the statistical uncertainty as well as the uncertainty associated to all the components in the optical chain, increased with distance and varied between 2.9%-4.5%, 1.8%-3.5% and 1.1%-3.7% for BCF-10, BCF-12 and BCF-60, respectively. The signal-to-noise ratio (SNR) fell below 5 at a radial distance of 3.2 cm, 3.8 cm and 3.0 cm, respectively. Since the dwell position shift formalism corrected for positioning uncertainties, these were not included here.

The impact of the shield on the dose distribution is shown in Figure A.10. The trend from the MC-calculated curve was well reproduced by the measurements. The dose rate at a radial distance of about 1 cm, measured by BCF-10, was reduced by up to 88.8%±1.2%, compared to the MC-calculated dose rate reduction of 83.5%±0.5%. The deviations in the maximum dose rate reduction were 5.3%, 7.0% and 1.4% (global relative to $\phi = 0°$) in Figure A.10a, A.10b and A.10c, respectively.

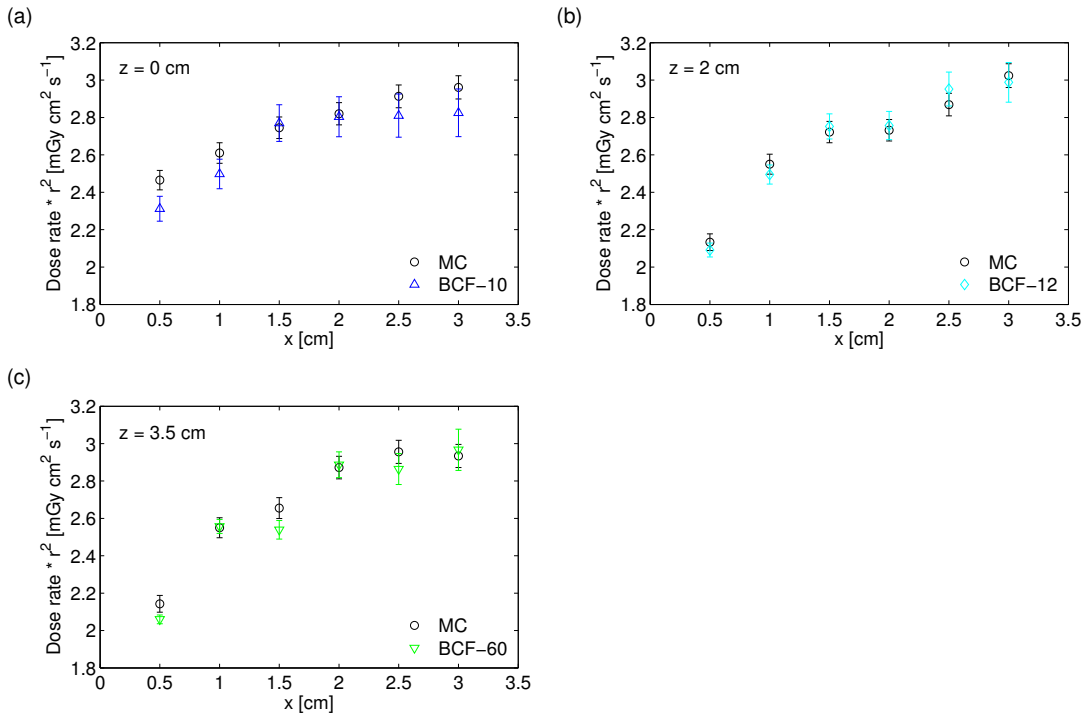

Figure A.9 – Comparison of the dose rate multiplied by radial distance squared r^2 measured by mPSD and calculated using MC along (a) $z = 0$ cm for BCF-10, (b) $z = 2$ cm for BCF-12, and (c) $z = 3.5$ cm for BCF-60. The distances to the source are relative to each scintillator's effective center. Error bars represent standard deviations.

Table A.5 – Total relative standard uncertainty budget (in %) for measurements of dose rate by mPSD at four different angles ϕ around the shielded ^{169}Yb source.

Source of uncertainty	Type	$\phi = 0°$	$\phi = 90°$	$\phi = 180°$	$\phi = 270°$
Measurement (BCF-10/BCF-12/BCF-60)	A	3.1/2.0/1.4	3.3/2.2/1.6	4.1/3.1/2.9	3.3/2.2/1.6
Source-to-detector distance (±0.2 mm)	B	4.0	4.0	4.0	4.0
Shield orientation (±5°)	B	0	6.0	1.0	6.0
Shield thickness (±0.025 mm)	B	0	0	5.5	0
Combined standard uncertainty (k=1)		**5.1/4.5/4.2**	**7.9/7.5/7.4**	**8.0/7.5/7.5**	**7.9/7.5/7.4**
Expanded uncertainty (k=2)		**10.2/9.0/8.4**	**15.8/15.0/14.8**	**16.0/15.0/15.0**	**15.8/15.0/14.8**

The total uncertainty budget for the dose rate measurements is described in Table A.5. In addition to type A uncertainties, uncertainties due to source-to-detector positioning, shield orientation and shield thickness were included in the budget. The dosimetric uncertainty due to source-to-detector positioning was based on the inverse square law effect for a ±0.2 mm shift. The dosimetric impact due to shield orientation uncertainty of ±5° was estimated using the gradient of the MC-calculated curve. The uncertainty due to shield thickness was based on the exponential attenuation expected from a ±0.025 mm variation in shield thickness. The uncertainties in the normalized dose rate were calculated as the quadrature sum of the total uncertainties for each measurement.

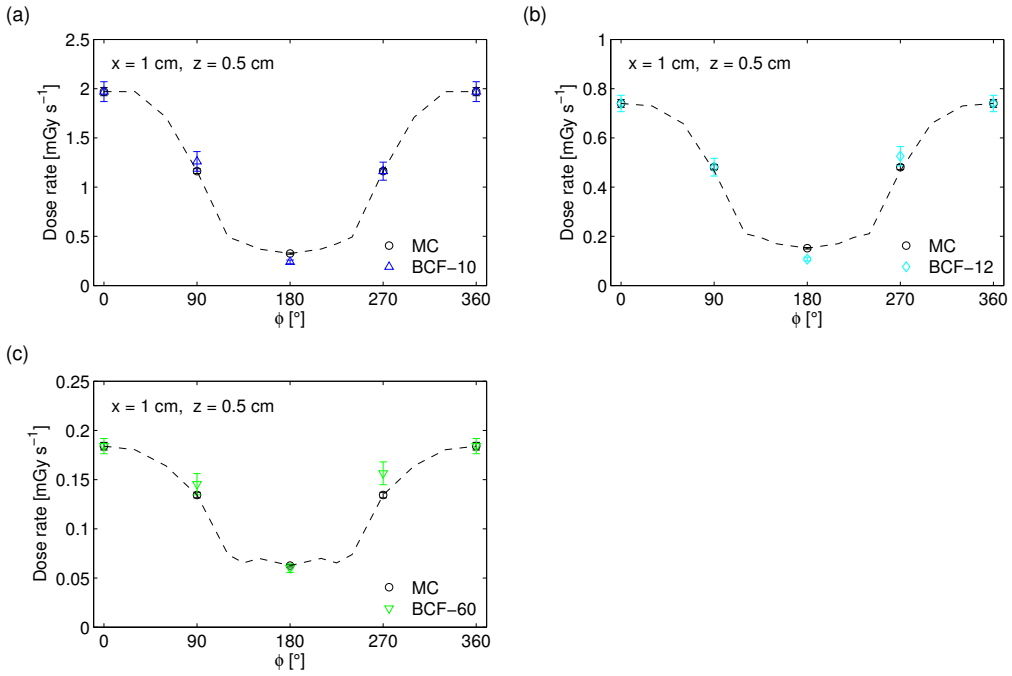

Figure A.10 – Comparison of the dose rate around the shielded ^{169}Yb source measured by (a) BCF-10, (b) BCF-12 and (c) BCF-60 and calculated with MC. Measurements were performed at $x = 1$ cm and $z = 0.5$ cm with a variable azimuthal angle ϕ. Error bars represent standard deviations.

A.6 Discussion

The TG-43U1 parameters were calculated using MC methods for the source model. The S_K/A was found comparable to other published values for ^{169}Yb source models: 1.33±0.04 U mCi^{-1} [143], 1.10±0.03 U mCi^{-1} [122], 1.08±0.03 U mCi^{-1} [123], 1.37±0.03 U mCi^{-1} [124], 1.15±0.03 U mCi^{-1} [140]. Deviations between source models were mostly attributed to the diameter of the active core and encapsulation. The Λ was in reasonable agreement with other reported values in the literature: 1.21±0.03 cGy h^{-1} U^{-1} [143], 1.204±0.004 cGy h^{-1} U^{-1} [141], 1.191±0.007 cGy h^{-1} U^{-1} [142], 1.17±0.01 cGy h^{-1} U^{-1} [142], 1.19±0.03 cGy h^{-1} U^{-1} [122], 1.12±0.04 cGy h^{-1} U^{-1} [123], 1.22±0.03 cGy h^{-1} U^{-1} [124], 1.19±0.03 cGy h^{-1} U^{-1} [140]. While the radial dose function $g_L(r)$ was in close agreement (<2% difference) with other HDR source models [122, 123] with larger diameter and length, the source model investigated in this study exhibited lower anisotropy closer to the longitudinal axis of the source, primarily due to the decreased attenuation within the active core volume and the encapsulation at the proximal and distal ends of the source. The increased contribution from scattered photons to dose deposition at depth (first mean free path of 3.0 cm) resulted in a dose falloff that is ideal for HDR brachytherapy in the therapeutic range.

The experimental verification of the dose distribution from the bare source was performed using the mPSD. Good agreement was achieved along the transverse axis for each scintillator, with deviations generally within their combined standard uncertainties. In the comparison of the along-away dose

data, deviations were largest for a detector-to-catheter distance of 0.5 cm, which was expected due to the relatively high positioning uncertainties that tend to dominate the total uncertainties at these short distances [8]. While the source-to-detector position was corrected according to the formalism published by Johansen *et al.* [10], the diameter of the source was thin (0.6 mm) compared to the inner diameter of the catheter (1.6 mm), which may have led to source displacements in the x-direction of ± 0.5 mm (uniform distribution). These random source position fluctuations were more difficult to identify than the longitudinal offsets. Even if this effect could be observed at all the distances explored, the dosimetric impact was more significant at short distances. In addition, reliable measurements were not possible for distances greater than 3 cm (dose rate <0.3 mGy s^{-1}) due to the low SNR measured by the mPSD. Relative deviations generally increased as the radial distance r from each scintillator's center increased, likely due to the decreased SNR in this low dose rate range. Overall, the SNR was greater than 5 for values of radial distance r below 3 cm. According to the Rose criterion, proper detection of an object strongly depends on SNR, only becoming possible when SNR exceeds 5; detection performance degrades as SNR approaches zero [30, 94]. In the regions where both positioning uncertainties and SNR were acceptable ($x \geq 1$ cm, $r \leq 3$ cm), differences between measured and calculated dose rates were generally within 5%.

The dose rate measurements for the bare source had several limitations. First, the low activity source (0.64 Ci) impacted both the validation range over which reliable measurements could be performed and the level of agreement in the regions where the SNR was appropriate. Measurement uncertainties are directly affected by the air kerma strength of brachytherapy sources. As the distance to the source is directly related to the dose rate, a decrease in the dose rate leads to an increase in the measurement uncertainty, especially at long distances from the source. Thus, it is expected that additional dose verification over an extended distance range can be performed with a higher activity source. Second, the positioning uncertainties put a lower limit on the range of distances that could be evaluated. The thin diameter of the source and guidewire relative to the catheter diameter resulted in positioning uncertainties in both the radial and longitudinal directions that were relatively higher than for sources and guidewires with larger diameter commonly used in HDR brachytherapy. While the custom afterloader typically has a positional accuracy (k=2) of ± 1 mm for larger diameter sources and guidewires, the positioning was less accurate (± 2 mm) for this experimental setup due to the increased bending and torsion of the cable. A commercial afterloader with a thin catheter may be able to ensure source positioning with better reproducibility for this source model, and eliminate the need to estimate the source path and correct for source-to-detector positioning errors. Despite the limitations in the dose rate measurements, the experimental verification with a multipoint dosimeter was useful for the purpose of this study. Three synchronized, independent sets of measurements were obtained for each dwell position explored, which allowed for real-time source localization. Source localization would have been difficult to achieve using independent single point dosimeters without the influence of additional sources of uncertainty.

The overall trend of the MC-calculated azimuthal anisotropy curve for the shielded source was reproduced by the measurements performed at four locations. MC calculations and mPSD measurements showed that the dose distribution around the shielded source is highly anisotropic. For the case where SNR was most reliable for all measurement locations (BCF-10), there was strong agreement at 0°, 90° and 270°, with differences within their combined uncertainties, while the difference in the maximum dose rate reduction was just above 5%. Discrepancies between measurements and calculations were

likely due to greater than expected positioning errors due to the non-uniformity or deformation of the shield and limitations in SNR for low dose rate regions. While this study demonstrated a proof of concept of the shielding capabilities of the partial platinum shield, the next step is to perform a full verification of the dose distribution over a larger range of distances using a high-activity ^{169}Yb source developed in collaboration with a medical device manufacturer and integrated into a commercial afterloader.

A.7 Conclusion

Due to the low activity of the ^{169}Yb source and SNR limitations, the measurements using the mPSD system were limited to a short spatial range. However, within this range, the agreement between measurements and MC calculations was within their combined uncertainties. Furthermore, we have demonstrated that the ^{169}Yb source coupled with the partial-shielding system is an effective technique to deliver IMBT. Additional verification at further distances would be required before a reference data set is established for this source model.

Acknowledgements

The authors would like to acknowledge Doug Leonardi for machining work and general aid with the experimental setup. This work was supported by the Natural Sciences and Engineering Research Council (grant numbers 241018, 484144-15 and RGPIN-2019-05038), Collaborative Health Research Projects (grant number 523394-18) and Canadian Foundation for Innovation (CFI) JR Evans Leader Funds grant number 35633. G.F. would like to acknowledge support by the NSERC Alexander Graham Bell Canada Graduate Scholarship. H.M.L.R. further acknowledges support from Fonds de Recherche du Quebec - Nature et Technologies (FRQNT).

Appendix B

Detection of positioning errors with the mPSD

Following the method proposed in Chapter 4, section 4.4.5, we derived the ROC curves to extract the metrics allowing the classification of deviations into possible errors based only on the mPSD source tracking accuracy. The method recommended in Chapter 4 to built the ROC curve is based on the knowledge of the measured and expected source coordinates along each axis (x, y and z). Since for a single dwell position, the mPSD source location prediction leads to a annular region around it (degeneracy in the ϕ direction), as mentioned in Chapter 3 and 4 it is not possible to distinguish in 3D space the x and the y coordinates of the source (assuming a coordinate system where x and y represent the radial direction, and z the depth). Thus, to build the ROC curve, we used the z coordinate as predicted by the mPSD, but in the xy direction, we selected the closest point to the planned source position. For this experiment, we used the same database of measurements as to in Chapter 4, section 4.4.5. Overall we used the information from 3741 dwell positions in plans number 3, 4, and 10 in table 4.1. The needle offsets were corrected according to the Dynamic Time Warping (DTW) methodology presented in section 4.4.4.

Figure B.1 summarises the key results obtained when quantifying the error detection probability as a function of the distance to the source. Figure B.1(a) shows the ROC curves obtained for the different ranges of distances to the source. For visualization purposes, only the curves for 0.5, 1.0, 2.0 and 3.0 mm error are illustrated. Figure B.1(b) displays the AUC, for three ranges of distance to the source, as a function of the introduced errors to the expected location from the plan.

The increase of the detector-to-source distance, reduces the mPSD capacity to detect errors [8]. This is due to an increase of the measurement uncertainty in combination with reduced accuracy of the dose prediction models in those measurement conditions [108]. This effect can be readily seen in figure B.1, as one move from the 5-25 mm to the 50-75 mm range. At short distances, there is a high probability of detecting positioning errors with a relatively lower incidence of false alarms. The analysis performed evidenced a detection probability that, in most cases, is far from the random detection threshold (dashed line in figure B.1a). The detection of small, 0.5 mm errors is barely possible (AUC of 0.64) at short distances and impossible in the other two distance ranges (AUC around 0.5). Based on these results, the mPSD can detect with good confidence error of 1 mm or more up to 25 mm from the

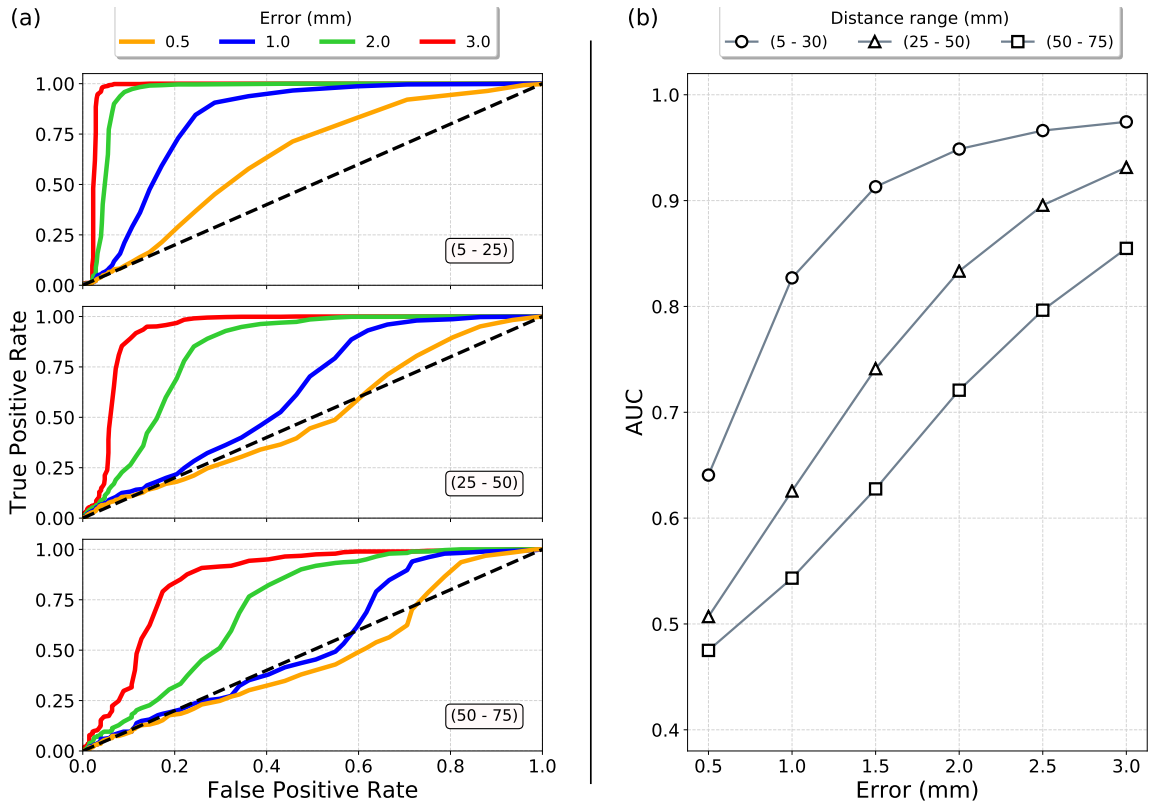

Figure B.1 – mPSD error detection probability as a function of the distance to the source. (a) ROC analysis. (b) AUC. The dashed line in (a) shows the limit for random detection probability.

source, and errors of larger than 2-3 mm at larger distances.

The use of the mPSD combined with another detector is advantageous, as demonstrated in Chapter 4, not only because it can eliminate the mPSD's degeneracy in the radial direction, but also because it reduces the incidence of the false alarms during the error detection process. The ROC curves obtained based only on the mPSD are closer to the diagonal line compared to the stepper curves obtained for the mPSD-ISD combined (see Chapter 4). For distances to the source up to 50 mm, the false positive rates for the optimal points on the ROC curves are smaller when using the mPSD-ISD than the mPSD alone. Although, this behaviour is not observed at distances beyond 50 mm, since the current ISD energy response correction factors are not optimal. It turn, this translates to less accurate combined source location extraction then simply using only the mPSD for source tracking.

Appendix C

IViST technical considerations

C.1 The software

IViST GUI was created using Qt 5.12.0, 64 bit for MAC. The software's engine runs under Python 3.7. The following lines contain requirements/specifications to run the software.

Requirements:

- NiDAQmx 19.0+ drivers
- Windows 8+: The current version is only supported on Windows OS, since the need for NiDAQmx drivers.

Engine packages:

- NI-DAQmx Python API
- PyQt5
- Numpy
- SciPy
- PyQtgraph
- Scikit-learn
- Keras 2.2.4+

C.2 Box manufacturing

IViST's light detection system was enclosed into a custom-made box to preserve the optical chain stability and easy manipulation. However, arriving at the box manufacturing required technical aspects as to their characteristics and physical requirements. The left panel in figure C.2 shows a picture of the system's first demo. Based on it, a 3D model for each component (figure C.1 right panel) was created in Autocad version P.47.M.5 and submited for a quotation request for manufacturing at Pronto Prototypes (Quebec, Canada). The items presented in the following were requirements and features also presented to the box manufacturer. Any user willing to construct a similar system should also take into account these items.

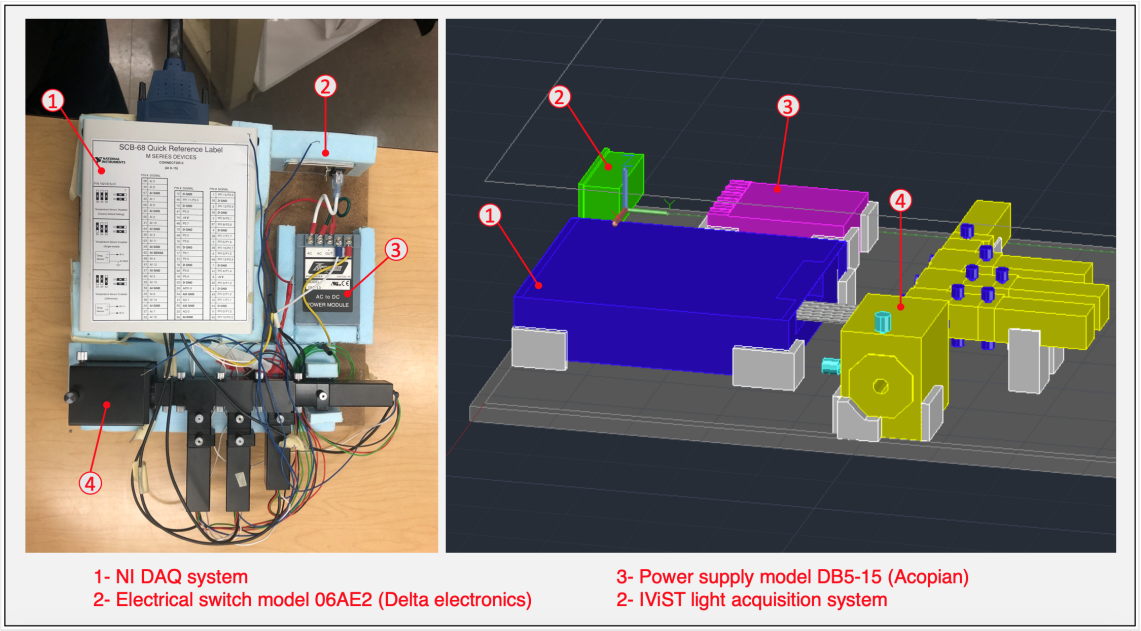

Figure C.1 – Demo (left panel) and 3D model (right panel) of IViST light detection system.

- **Manufacturing material:** The construction material should be an electrical isolator (plastic, acrylic, etc.). It reduces electrical risks and simplifies the system's electronics.
- **Temperature dissipation:** The box faces should account for heat dissipation windows. Long periods of measurements increase the temperature generated by the system's components, which increases the background signal of the PMTs. Thus, the measurements could change with time. This effect can be solved by using, for example, a heat dissipation fan. However, we decided not to include this component since it can produce random changes in the PMT's response. Instead, we went with natural dissipation through ventilation windows.
- **Fixation supports:** As part of the system's components, we designed several supports to avoid the movement of the components in X, Y, Z during transportation. The fixation should allow for easy assembly and access.
- **Wires connection:** Since there is a voltage generated by the system, the wires connection should be protected. Our design includes an isolated false floor only devoted to wiring. The power supply terminals are covered, and a fuse was included in the electrical circuit entrance to protect from over-current.

Figure C.2 shows the final drawing of IViST's box in 2D that corresponds to the system showed in figure 6.1, Chapter 6. The dosimetry system here presented was inspected by the biomedical engineering team at CHU de Québec - Université Laval (Québec, Canada). The verifications were done according to a series of technical standards for the safety and essential performance of medical electrical equipment, published by the International Electrotechnical Commission (IEC) 60601. IEC 60601 is a widely accepted benchmark that has become a requirement for the commercialization of electrical medical equipment in many countries. The system passed all the tests. No electrical leaks were found, and the requested parameters were within the tolerances.

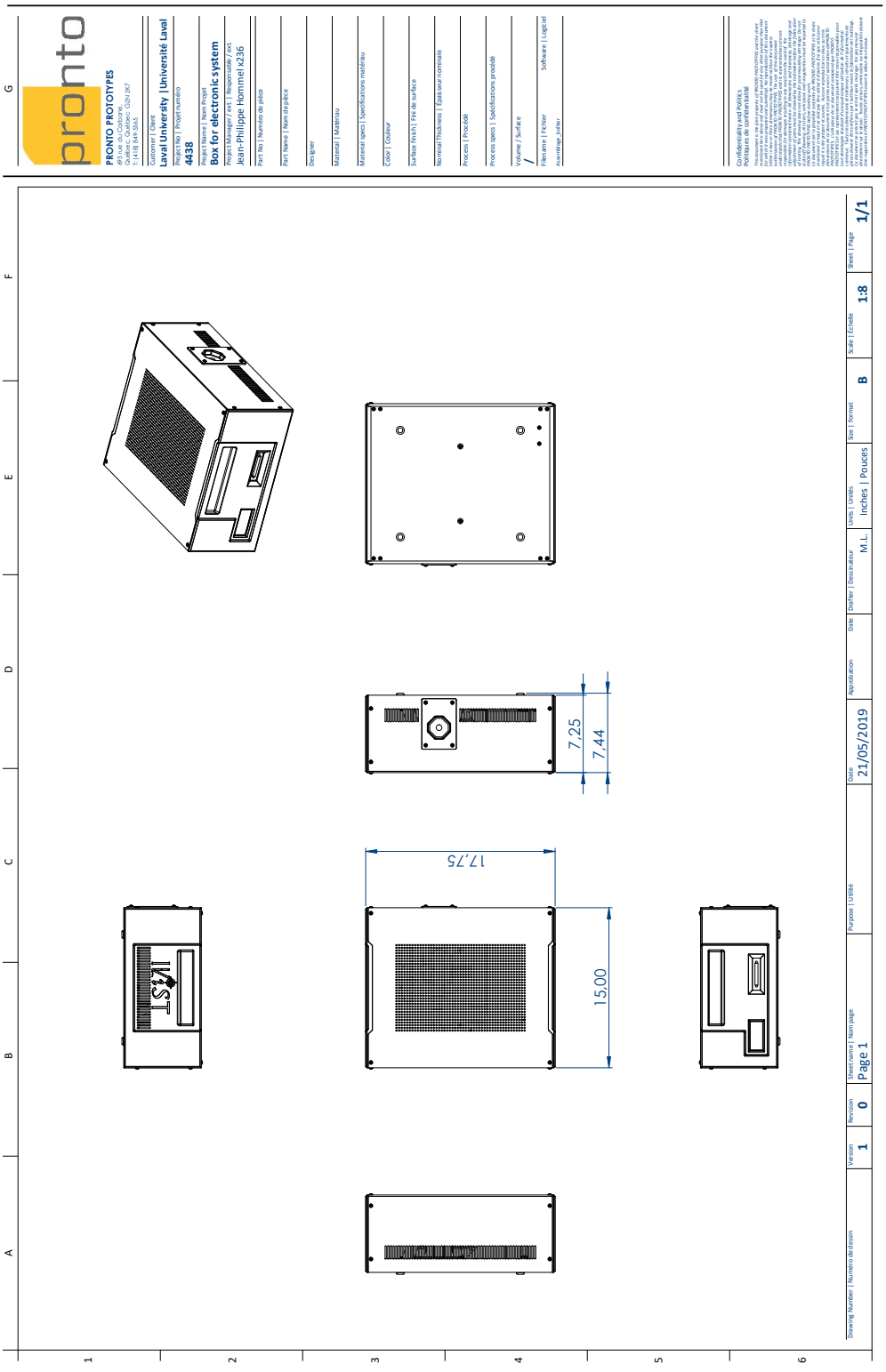

Figure C.2 – 2D drawing of IViST's box.

Bibliography

[1] Eduardo Rosenblatt and Eduardo Zubizarreta. *Radiotherapy in cancer care: facing the global challenge*. International Atomic Energy Agency Vienna, 2017.

[2] William R. Hendee and X. Allen Li. *Adaptive Radiation Therapy.*, volume 38. CRC Press, Taylor and Francis Group, 2011.

[3] Faiz M. Khan. *The Physics of Radiation Therapy*. LIPPINCOTT WILLIAMS and WILKINS, 5 edition, 2014. ISBN: 978-1-4511-8245-3.

[4] Martin J Murphy. *Adaptive motion compensation in radiotherapy*. CRC Press, 2011.

[5] Jack L. M. Venselaar, Dimos Baltas, Ali S. Meigooni, and Peter J. Hoskin, editors. *Comprehensive brachytherapy : physical and clinical aspects*. Imaging in medical diagnosis and therapy. CRC Press, Boca Raton, FL, 2013. ISBN: 978-1-439844-991.

[6] Christian Kirisits, Mark J Rivard, Dimos Baltas, Facundo Ballester, Marisol De Brabandere, Rob van der Laarse, Yury Niatsetski, Panagiotis Papagiannis, Taran Paulsen Hellebust, Jose Perez-Calatayud, et al. Review of clinical brachytherapy uncertainties: analysis guidelines of gec-estro and the aapm. *Radiotherapy and oncology*, 110(1):199–212, 2014.

[7] Kari Tanderup, Sam Beddar, Claus E. Andersen, Gustavo Kertzscher, and Joanna E. Cygler. In vivo dosimetry in brachytherapy. *Medical Physics*, 40(7):070902, 2013.

[8] Claus E. Andersen, Søren Kynde Nielsen, Jacob Christian Lindegaard, and Kari Tanderup. Time-resolved in vivo luminescence dosimetry for online error detection in pulsed dose-rate brachytherapy. *Medical Physics*, 36(11):5033–5043, 2009.

[9] Francois Therriault-Proulx, Sam Beddar, and Luc Beaulieu. On the use of a single-fiber multipoint plastic scintillation detector for ^{192}Ir high-dose-rate brachytherapy. *Medical Physics*, 40(6):062101, 2013.

[10] Jacob Graversen Johansen, Susanne Rylander, Simon Buus, Lise Bentzen, Steffen Bjerre Hokland, Christian Skou Søndergaard, Anders Karl Mikael With, Gustavo Kertzscher, and Kari Tanderup. Time-resolved in vivo dosimetry for source tracking in brachytherapy. *Brachytherapy*, 17(1):122–132, February 2018.

[11] Ryan L. Smith, Annette Haworth, Vanessa Panettieri, Jeremy L. Millar, and Rick D. Franich. A method for verification of treatment delivery in hdr prostate brachytherapy using a flat panel detector for both imaging and source tracking. *Medical Physics*, 43(5):2435–2442, 2016.

[12] P. Guiral, J. Ribouton, P. Jalade, R. Wang, J.-M. Galvan, G.-N. Lu, P. Pittet, A. Rivoire, and L. Gindraux. Design and testing of a phantom and instrumented gynecological applicator based on gan dosimeter for use in high dose rate brachytherapy quality assurance. *Medical Physics*, 43(9):5240–5251, 2016.

[13] T Nakano, N Suchowerska, D R McKenzie, and M M Bilek. Real-time verification of hdr brachytherapy source location: implementation of detector redundancy. *Physics in Medicine and Biology*, 50(2):319, 2005.

[14] Gabriel P Fonseca, Mark Podesta, Murillo Bellezzo, Michiel R Van den Bosch, Ludy Lutgens, Ben G L Vanneste, Robert Voncken, Evert J Van Limbergen, Brigitte Reniers, and Frank Verhaegen. Online pretreatment verification of high-dose rate brachytherapy using an imaging panel. *Physics in Medicine and Biology*, 62(13):5440, 2017.

[15] A. S. Beddar, T. R. Mackie, and F. H. Attix. Cerenkov light generated in optical fibres and other light pipes irradiated by electron beams. *Physics in Medicine and Biology*, 37(4):925–935, 1992.

[16] A. S. Beddar, T. R. Mackie, and F. H. Attix. Water-equivalent plastic scintillation detectors for high-energy beam dosimetry: I. Physical characteristics and theoretical considerations. *Physics in Medicine and Biology*, 37(10):1883–1900, 1992.

[17] A. S. Beddar, T. R. Mackie, and F. H. Attix. Water-equivalent plastic scintillation detectors for high-energy beam dosimetry: II. Properties and measurements. *Physics in Medicine and Biology*, 37(10):1901, 1992.

[18] J. Lambert, D. R. McKenzie, S. Law, J. Elsey, and N. Suchowerska. A plastic scintillation dosimeter for high dose rate brachytherapy. *Physics in Medicine and Biology*, 51(21):5505, 2006.

[19] Louis Archambault, A. Sam Beddar, Luc Gingras, René Roy, and Luc Beaulieu. Measurement accuracy and cerenkov removal for high performance, high spatial resolution scintillation dosimetry. *Medical Physics*, 33(1):128–135, 2006.

[20] J Lambert, Y Yin, D R McKenzie, S Law, and N Suchowerska. Cerenkov-free scintillation dosimetry in external beam radiotherapy with an air core light guide. *Physics in Medicine and Biology*, 53(11):3071, 2008.

[21] M Guillot, L Gingras, L Archambault, S Beddar, and L Beaulieu. Toward 3d dosimetry of intensity modulated radiation therapy treatments with plastic scintillation detectors. *Journal of Physics: Conference Series*, 250(1):012006, 2010.

[22] Francois Therriault-Proulx, Sam Beddar, Tina M. Briere, Louis Archambault, and Luc Beaulieu. Technical note: Removing the stem effect when performing Ir-192 HDR brachytherapy in vivo dosimetry using plastic scintillation detectors: A relevant and necessary step. *Medical Physics*, 38(4):2176–2179, 2011.

[23] Francois Therriault-Proulx, Tina M. Briere, Firas Mourtada, Sylviane Aubin, Sam Beddar, and Luc Beaulieu. A phantom study of an in vivo dosimetry system using plastic scintillation detectors for real-time verification of ^{192}Ir HDR brachytherapy. *Medical Physics*, 38(5):2542–2551, 2011.

[24] Paul Z. Y. Liu, Natalka Suchowerska, Peter Abolfathi, and David R. McKenzie. Real-time scintillation array dosimetry for radiotherapy: The advantages of photomultiplier detectors. *Medical Physics*, 39(4):1688–1695, 2012.

[25] L Beaulieu, M Goulet, L Archambault, and S Beddar. Current status of scintillation dosimetry for megavoltage beams. *Journal of Physics: Conference Series*, 444(1):012013, 2013.

[26] Landon Wootton and Sam Beddar. Temperature dependence of bcf plastic scintillation detectors. *Physics in Medicine and Biology*, 58(9):2955, 2013.

[27] Francois Therriault-Proulx, Landon Wootton, and Sam Beddar. A method to correct for temperature dependence and measure simultaneously dose and temperature using a plastic scintillation detector. *Physics in Medicine and Biology*, 60(20):7927, 2015.

[28] Jonathan Boivin, Sam Beddar, Chris Bonde, Daniel Schmidt, Wesley Culberson, Maxime Guillemette, and Luc Beaulieu. A systematic characterization of the low-energy photon response of plastic scintillation detectors. *Physics in Medicine and Biology*, 61(15):5569, 2016.

[29] François Therriault-Proulx, Luc Beaulieu, and Sam Beddar. Validation of plastic scintillation detectors for applications in low-dose-rate brachytherapy. *Brachytherapy*, 16(4):903–909, 2017.

[30] Haydee M. Linares Rosales, Patricia Duguay-Drouin, Louis Archambault, Sam Beddar, and Luc Beaulieu. Optimization of a multipoint plastic scintillator dosimeter for high dose rate brachytherapy. *Medical Physics*, 46(5):2412–2421, 2019.

[31] François Therriault-Proulx, Louis Archambault, Luc Beaulieu, and Sam Beddar. Development of a novel multi-point plastic scintillation detector with a single optical transmission line for radiation dose measurement. *Physics in Medicine and Biology*, 57(21):7147, 2012.

[32] Louis Archambault, François Therriault-Proulx, Sam Beddar, and Luc Beaulieu. A mathematical formalism for hyperspectral, multipoint plastic scintillation detectors. *Physics in Medicine and Biology*, 57(21):7133, 2012.

[33] Patricia Duguay-Druin. Caractérisation et optimisation d'un détecteur à scintillation à 2 points. Master's thesis, Université Laval, 2016.

[34] Sam Beddar. On possible temperature dependence of plastic scintillator response. *Medical Physics*, 39(10):6522–6522, 2012.

[35] S F de Boer, A S Beddar, and J A Rawlinson. Optical filtering and spectral measurements of radiation-induced light in plastic scintillation dosimetry. *Physics in Medicine and Biology*, 38(7):945, 1993.

[36] J. M. Fontbonne, G. Iltis, G. Ban, A. Battala, J. C. Vernhes, J. Tillier, N. Bellaize, C. Le Brun, B. Tamain, K. Mercier, and J. C. Motin. Scintillating fiber dosimeter for radiation therapy accelerator. *IEEE Transactions on Nuclear Science*, 49(5):2223–2227, 2002.

[37] M A Clift, P N Johnston, and D V Webb. A temporal method of avoiding the cerenkov radiation generated in organic scintillator dosimeters by pulsed mega-voltage electron and photon beams. *Physics in Medicine amd Biology*, 47(8):1421, 2002.

[38] William Y Song, Kari Tanderup, and Bradley Pieters. *Emerging Technologies in Brachytherapy*. CRC Press, 2017.

[39] V Chambrette, S Hardy, and JC Nenot. Irradiation accidents. establishment of a data base "accirad" at the ipsn. *Radioprotection*, 36:477–510, 2001.

[40] Jack Valentin. Icrp publication 97: Prevention of high-dose-rate brachytherapy accidents. *Annals of the ICRP*, 35:1–51, 02 2005.

[41] Ola Holmberg, Jim Malone, Madan Rehani, Donald McLean, and Renate Czarwinski. Current issues and actions in radiation protection of patients. *European journal of radiology*, 76(1):15–19, 2010.

[42] International Commission on Radiological Protection. Prevention of accidental exposures to patients undergoing radiation therapy: Icrp publication 86. *Ann. ICRP*, 30:7–70, 2000.

[43] International Atomic Energy Agency. *Lessons learned from accidental exposures in radiotherapy*. Internat. Atomic Energy Agency, 2000.

[44] Gustavo Kertzscher, A Rosenfeld, Sam Beddar, K Tanderup, and JE Cygler. In vivo dosimetry: trends and prospects for brachytherapy. *The British journal of radiology*, 87(1041):20140206, 2014.

[45] J Venselaar and J Pérez-Calatayud. A practical guide to quality control of brachytherapy equipment, estro booklet no. 8. *Brussels: European Society for Therapeutic Radiology and Oncology*, 2004.

[46] Mark J. Rivard, Bert M. Coursey, Larry A. DeWerd, William F. Hanson, Huq M. Saiful, Geoffrey S. Ibbott, Michael G. Mitch, Ravinder Nath, and Jeffrey F. Williamson. Update of aapm task group no. 43 report: A revised aapm protocol for brachytherapy dose calculations. *Medical Physics*, 31(3):633–674, 2004.

[47] Claus E. Andersen, Søren Kynde Nielsen, Steffen Greilich, Jakob Helt-Hansen, Jacob Christian Lindegaard, and Kari Tanderup. Characterization of a fiber-coupled Al2o3:C luminescence dosimetry system for online in vivo dose verification during I192r brachytherapy. *Medical Physics*, 36(3):708–718, March 2009.

[48] L. E. Cartwright, N. Suchowerska, Y. Yin, J. Lambert, M. Haque, and D. R. McKenzie. Dose mapping of the rectal wall during brachytherapy with an array of scintillation dosimeters. *Medical Physics*, 37(5):2247–2255, May 2010.

[49] Nicholas Hardcastle, Dean L. Cutajar, Peter E. Metcalfe, Michael L. F. Lerch, Vladimir L. Perevertaylo, Wolfgang A. Tomé, and Anatoly B. Rosenfeld. In vivo real-time rectal wall dosimetry for prostate radiotherapy. *Physics in Medicine and Biology*, 55(13):3859, 2010.

[50] Gustavo Kertzscher, Claus E. Andersen, Frank-André Siebert, Søren Kynde Nielsen, Jacob C. Lindegaard, and Kari Tanderup. Identifying afterloading PDR and HDR brachytherapy errors using real-time fiber-coupled Al2o3:C dosimetry and a novel statistical error decision criterion. *Radiotherapy and Oncology*, 100(3):456–462, September 2011.

[51] Erin L. Seymour, Simon J. Downes, Gerald B. Fogarty, Michael A. Izard, and Peter Metcalfe. In vivo real-time dosimetric verification in high dose rate prostate brachytherapy. *Medical Physics*, 38(8):4785–4794, August 2011.

[52] Gustavo Kertzscher, Claus E. Andersen, and Kari Tanderup. Adaptive error detection for HDR/PDR brachytherapy: guidance for decision making during real-time in vivo point dosimetry. *Medical Physics*, 41(5):052102, May 2014.

[53] Rajni Sethi, Yueh Chun Kuo, Babak Edraki, Dimitry Lerner, Daniel Paik, and William Bice. Real-time doppler ultrasound to identify vessels and guide needle placement for gynecologic interstitial brachytherapy. *Brachytherapy*, 17:S114–S115, 07 2018.

[54] Ben Mijnheer, Sam Beddar, Joanna Izewska, and Chester Reft. In vivo dosimetry in external beam radiotherapy. *Medical Physics*, 40(7), July 2013.

[55] Ben Mijnheer. State of the art of in vivo dosimetry. *Radiation Protection Dosimetry*, 131(1):117–122, August 2008.

[56] D.W. O. Rogers and Joanna E. Cygler, editors. *Clinical Dosimetry Measurements in Radiotherapy*. Medical Physics Publishing, Madison,Wisconsin, 2009. ISBN: 978-1-888340-84-6.

[57] Jamil Lambert, Tatsuya Nakano, Sue Law, Justin Elsey, David R. McKenzie, and Natalka Suchowerska. In vivo dosimeters for HDR brachytherapy: A comparison of a diamond detector, MOSFET, TLD, and scintillation detector. *Medical Physics*, 34(5):1759–1765, May 2007.

[58] P. Karaiskos, A. Angelopoulos, L. Sakelliou, P. Sandilos, C. Antypas, L. Vlachos, and E. Koutsouveli. Monte Carlo and TLD dosimetry of an 192ir high dose-rate brachytherapy source. *Medical Physics*, 25(10):1975–1984, October 1998.

[59] G. Anagnostopoulos, D. Baltas, A. Geretschlaeger, T. Martin, P. Papagiannis, N. Tselis, and N. Zamboglou. In vivo thermoluminescence dosimetry dose verification of transperineal 192ir high-dose-rate brachytherapy using CT-based planning for the treatment of prostate cancer. *International Journal of Radiation Oncology Biology Physics*, 57(4):1183–1191, November 2003.

[60] R. Das, W. Toye, T. Kron, S. Williams, and G. Duchesne. Thermoluminescence dosimetry for in-vivo verification of high dose rate brachytherapy for prostate cancer. *Australasian Physics and Engineering Sciences in Medicine*, 30(3):178, 2007.

[61] A. S. Meigooni, J. A. Meli, and R. Nath. Influence of the variation of energy spectra with depth in the dosimetry of 192 Ir using LiF TLD. *Physics in Medicine and Biology*, 33(10):1159, 1988.

[62] K. Mugabe A. Haughey, G. Coalter. Evaluation of linear array mosfet detectors for in vivo dosimetry to measure rectal dose in hdr brachytherapy. *Australas Phys Eng Sci Med*, 34:361–366, 2011.

[63] Rajesh A. Kinhikar, Pramod K. Sharma, Chandrashekhar M. Tambe, and Deepak D. Deshpande. Dosimetric evaluation of a new OneDose MOSFET for Ir-192 energy. *Physics in Medicine and Biology*, 51(5):1261, 2006.

[64] Zhen-Yu Qi, Xiao-Wu Deng, Shao-Min Huang, Jie Lu, Michael Lerch, Dean Cutajar, and Anatoly Rosenfeld. Verification of the plan dosimetry for high dose rate brachytherapy using metal–oxide–semiconductor field effect transistor detectors. *Medical Physics*, 34(6):2007–2013, June 2007.

[65] Valéry Olivier Zilio, Om Parkash Joneja, Youri Popowski, Anatoly Rosenfeld, and Rakesh Chawla. Absolute depth-dose-rate measurements for an Ir192 HDR brachytherapy source in water using MOSFET detectors. *Medical Physics*, 33(6):1532–1539, June 2006.

[66] Marie-Claude Lavallée, Luc Gingras, and Luc Beaulieu. Energy and integrated dose dependence of mosfet dosimeter sensitivity for irradiation energies between and. *Medical physics*, 33(10):3683–3689, 2006.

[67] Esther J Bloemen-van Gurp, Lars HP Murrer, Björk KC Haanstra, Francis CJM Van Gils, Andre LAJ Dekker, Ben J Mijnheer, and Philippe Lambin. In vivo dosimetry using a linear mosfet-array dosimeter to determine the urethra dose in 125i permanent prostate implants. *International Journal of Radiation Oncology* Biology* Physics*, 73(1):314–321, 2009.

[68] Esther J Bloemen-van Gurp, Björk KC Haanstra, Lars HP Murrer, Francis CJM van Gils, Andre LAJ Dekker, Ben J Mijnheer, and Philippe Lambin. In vivo dosimetry with a linear mosfet array to evaluate the urethra dose during permanent implant brachytherapy using iodine-125. *International Journal of Radiation Oncology* Biology* Physics*, 75(4):1266–1272, 2009.

[69] Christopher Jason Tien, Robert III Ebeling, Jessica R. Hiatt, Bruce Curran, and Edward Sternick. Optically Stimulated Luminescent Dosimetry for High Dose Rate Brachytherapy. *Frontiers in Oncology*, 2, 2012.

[70] Ravinder Nath, Lowell L. Anderson, Gary Luxton, Keith A. Weaver, Jeffrey F. Williamson, and Ali S. Meigooni. Dosimetry of interstitial brachytherapy sources: Recommendations of the AAPM Radiation Therapy Committee Task Group No. 43. *Medical Physics*, 22(2):209–234, February 1995.

[71] E.B. Podgorsak, editor. *Radiation Oncology Physics: A Handbook for teachers and students*. International Atomic Energy Agency, Vienna, 2005. ISBN: 92–0–107304–6.

[72] J.B. Birks. *The Theory and Practice of Scintillations Counting*. Pergamon Press LTD., 1964.

[73] Glenn F. Knoll. *Radiation Detection and Measurement*, volume 4. John Wiley and Sons, Inc., 2010. ISBN:978-0-470-13148-0.

[74] Sam Beddar and Luc Beaulieu, editors. *Scintillation Dosimetry*. CRC Press, 2016. ISBN: 978-1-4822-0900-6.

[75] Luc Beaulieu and Sam Beddar. Review of plastic and liquid scintillation dosimetry for photon, electron, and proton therapy. *Physics in Medicine and Biology*, 61(20):R305, 2016.

[76] Frank Herbert Attix. *Introduction to Radiological Physics and Radiation Dosimetry*. Wiley VCH, 2004. ISBN-10: 0-471-01 146-0.

[77] A. Sam Beddar, Tina Marie Briere, Firas A. Mourtada, Oleg N. Vassiliev, H. Helen Liu, and Radhe Mohan. Monte Carlo calculations of the absorbed dose and energy dependence of plastic scintillators. *Medical Physics*, 32(5):1265–1269, May 2005.

[78] A. S. Beddar. A new scintillator detector system for the quality assurance of ^{60}Co and high-energy therapy machines. *Physics in Medicine and Biology*, 39(2):253, 1994.

[79] Indra J. Das, Michael J. Gazda, and A. S. Beddar. Characteristics of a scintillator based daily quality assurance device for radiation oncology beams. *Medical Physics*, 23(12):2061–2067, December 1996.

[80] P. Carrasco, N. Jornet, O. Jordi, M. Lizondo, A. Latorre-Musoll, T. Eudaldo, A. Ruiz, and M. Ribas. Characterization of the Exradin W1 scintillator for use in radiotherapy. *Medical Physics*, 42(1):297–304, January 2015.

[81] Louis Archambault, A. Sam Beddar, Luc Gingras, Fréderic Lacroix, René Roy, and Luc Beaulieu. Water-equivalent dosimeter array for small-field external beam radiotherapy. *Medical Physics*, 34(5):1583–1592, May 2007.

[82] Frédéric Lacroix, Luc Beaulieu, Louis Archambault, and A Sam Beddar. Simulation of the precision limits of plastic scintillation detectors using optimal component selection. *Medical physics*, 37(2):412–418, 2010.

[83] Luis Peralta. Temperature dependence of plastic scintillators. *Nuclear Instruments and Methods in Physics Research Section A: Accelerators, Spectrometers, Detectors and Associated Equipment*, 883:20–23, 2018.

[84] S. Buranurak, C.E. Andersen, A.R. Beierholm, and L.R. Lindvold. Temperature variations as a source of uncertainty in medical fiber-coupled organic plastic scintillator dosimetry. *Radiation Measurements*, 56:307–311, 2013.

[85] François Therriault-Proulx, Luc Beaulieu, Louis Archambault, and Sam Beddar. On the nature of the light produced within pmma optical light guides in scintillation fiber-optic dosimetry. *Physics in Medicine and Biology*, 58(7):2073, 2013.

[86] G Kertzscher and S Beddar. Inorganic scintillator detectors for real-time verification during brachytherapy. *Journal of Physics: Conference Series*, 847:012036, may 2017.

[87] Gustavo Kertzscher and Sam Beddar. Inorganic scintillation detectors for 192ir brachytherapy. *Physics in Medicine and Biology*, 64(22):225018, 2019.

[88] Guylaine Ayotte, Louis Archambault, Luc Gingras, Frédéric Lacroix, A. Sam Beddar, and Luc Beaulieu. Surface preparation and coupling in plastic scintillator dosimetry. *Medical Physics*, 33(9):3519–3525, 2006.

[89] Hamamatsu Photonics. Hamamatsu PMT H10722 Series, October 2016. https://www.hamamatsu.com/resources/pdf/etd/H10722_TPMO1063E.pdf.

[90] National Instruments Corporation. National Instruments Multifunction Data Acquisition Device, October 2016. http://sine.ni.com/nips/cds/view/p/lang/en/nid/209154.

[91] Jonathan Boivin, Sam Beddar, Maxime Guillemette, and Luc Beaulieu. Systematic evaluation of photodetector performance for plastic scintillation dosimetry. *Medical Physics*, 42(11):6211–6220, 2015.

[92] A Sam Beddar, Susan Law, Natalka Suchowerska, and T Rockwell Mackie. Plastic scintillation dosimetry: optimization of light collection efficiency. *Physics in Medicine and Biology*, 48(9):1141, 2003.

[93] Frédéric Lacroix, A. Sam Beddar, Mathieu Guillot, Luc Beaulieu, and Luc Gingras. A design methodology using signal-to-noise ratio for plastic scintillation detectors design and performance optimization. *Medical Physics*, 36(11):5214–5220, 2009.

[94] Jerrold T. Bushberg, J. Anthony Sibert, Edwin M. Leidholdt, and John M. Boone. *The Essential Physics of Medical Imaging*. LIPPINCOTT WILLIAMS and WILKINS, a WOLTERS KLUWER, Philadelphia, PA, 3rd edition, 2012.

[95] R. Das, W. Toye, T. Kron, S. Williams, and G. Duchesne. Thermoluminescence dosimetry for in-vivo verification of high dose rate brachytherapy for prostate cancer. *Australasian Physics and Engineering Sciences in Medicine*, 30(3):178, September 2007.

[96] Warren Toye, Ram Das, Tomas Kron, Rick Franich, Peter Johnston, and Gillian Duchesne. An in vivo investigative protocol for HDR prostate brachytherapy using urethral and rectal thermoluminescence dosimetry. *Radiotherapy and Oncology*, 91(2):243–248, May 2009.

[97] G Anagnostopoulos, D Baltas, A Geretschlaeger, T Martin, P Papagiannis, N Tselis, and N Zamboglou. In vivo thermoluminescence dosimetry dose verification of transperineal 192ir high-dose-rate brachytherapy using CT-based planning for the treatment of prostate cancer. *International Journal of Radiation Oncology*Biology*Physics*, 57(4):1183–1191, November 2003.

[98] Gustavo Kertzscher and Sam Beddar. Ruby-based inorganic scintillation detectors for192ir brachytherapy. *Physics in Medicine and Biology*, 61(21):7744–7764, oct 2016.

[99] Jose Perez-Calatayud, Facundo Ballester, Rupak K. Das, Larry A. DeWerd, Geoffrey S. Ibbott, Ali S. Meigooni, Zoubir Ouhib, Mark J. Rivard, Ron S. Sloboda, and Jeffrey F. Williamson. Dose calculation for photon-emitting brachytherapy sources with average energy higher than 50 kev: Report of the aapm and estro. *Medical Physics*, 39(5):2904–2929, 2012.

[100] Jerry L. Hintze and Ray D. Nelson. Violin plots: A box plot-density trace synergism. *The American Statistician*, 52(2):181–184, 1998.

[101] T Nakano, N Suchowerska, M M Bilek, D R McKenzie, N Ng, and T Kron. High dose-rate brachytherapy source localization: positional resolution using a diamond detector. *Physics in Medicine and Biology*, 48(14):2133–2146, jul 2003.

[102] Larry A. DeWerd, Geoffrey S. Ibbott, Ali S. Meigooni, Michael G. Mitch, Mark J. Rivard, Kurt E. Stump, Bruce R. Thomadsen, and Jack L. M. Venselaar. A dosimetric uncertainty analysis for photon-emitting brachytherapy sources: Report of aapm task group no. 138 and gec-estro. *Medical Physics*, 38(2):782–801, 2011.

[103] Lilie L. W. Wang, David Klein, and A. Sam Beddar. Monte Carlo study of the energy and angular dependence of the response of plastic scintillation detectors in photon beams. *Medical Physics*, 37(10):5279–5286, October 2010.

[104] Lilie L. W. Wang and Sam Beddar. Study of the response of plastic scintillation detectors in small-field 6 MV photon beams by Monte Carlo simulations. *Medical Physics*, 38(3):1596–1599, March 2011.

[105] Jean-Christophe Gagnon, Dany Thériault, Mathieu Guillot, Louis Archambault, Sam Beddar, Luc Gingras, and Luc Beaulieu. Dosimetric performance and array assessment of plastic scintillation detectors for stereotactic radiosurgery quality assurance. *Medical Physics*, 39(1):429–436, January 2012.

[106] Jeppe Brage Christensen and Claus E Andersen. Relating ionization quenching in organic plastic scintillators to basic material properties by modelling excitation density transport and amorphous track structure during proton irradiation. *Physics in Medicine and Biology*, 63(19):195010, 2018.

[107] Jeffrey F Williamson. Brachytherapy technology and physics practice since 1950: a half-century of progress. *Physics in Medicine and Biology*, 51(13):R303–R325, jun 2006.

[108] Haydee M. Linares Rosales, L Archambault, S Beddar, and L Beaulieu. Dosimetric performance of a multi-point plastic scintillator dosimeter as a tool for real-time source tracking in high dose rate 192 ir brachytherapy. *Medical Physics*, 2020.

[109] L. RABINER. Fundamentals of speech recognition. *Fundamentals of speech recognition*, 1993.

[110] R. L. Smith, M. L. Taylor, L. N. McDermott, A. Haworth, J. L. Millar, and R. D. Franich. Source position verification and dosimetry in HDR brachytherapy using an EPID. *Medical Physics*, 40(11):111706, November 2013.

[111] Jun Duan, Daniel J Macey, Prem N Pareek, and Ivan A Brezovich. Real-time monitoring and verification of in vivo high dose rate brachytherapy using a pinhole camera. *Medical physics*, 28(2):167–173, 2001.

[112] M Batič, J Burger, V Cindro, G Kramberger, I Mandič, M Mikuž, A Studen, and M Zavrtanik. Verification of high dose rate 192ir source position during brachytherapy treatment. *Nuclear Instruments and Methods in Physics Research Section A: Accelerators, Spectrometers, Detectors and Associated Equipment*, 617(1-3):206–208, 2010.

[113] Mitra Safavi-Naeini, Zhangbo Han, Sarah Alnaghy, D Cutajar, Marco Petasecca, Michael LF Lerch, Daniel R Franklin, J Bucci, M Carrara, Marco Zaider, et al. Brachyview, a novel in-body imaging system for hdr prostate brachytherapy: Experimental evaluation. *Medical physics*, 42(12):7098–7107, 2015.

[114] Yusuke Watanabe, Hiroshi Muraishi, Hideyuki Takei, Hidetake Hara, Tsuyoshi Terazaki, Nobuaki Shuto, Takahiro Shimo, Marika Nozawa, Hiromichi Ishiyama, Kazushige Hayakawa, et al. Automated source tracking with a pinhole imaging system during high-dose-rate brachytherapy treatment. *Physics in Medicine and Biology*, 63(14):145002, 2018.

[115] Gabriel Fonseca, Jacob G. Johansen, Ryan L Smith, Luc Beaulieu, Sam Beddar, Gustavo Kertzscher, Frank Verhaegen, and Kari Tanderup. In vivo dosimetry in brachytherapy: requirements and future directions for research, development, and clinical practice. *Accepted for publication at Physics and Imaging in Radiation Oncology*, 2020.

[116] A. Criminisi, D. Robertson, E. Konukoglu, J. Shotton, S. Pathak, S. White, and K. Siddiqui. Regression forests for efficient anatomy detection and localization in computed tomography scans. *Medical Image Analysis*, 17(8):1293 – 1303, 2013.

[117] Scikit-learn. Scikit-learn machine learning in python, April 2019. https://scikit-learn.org/stable/about.html#citing-scikit-learn.

[118] François Chollet et al. Keras. https://keras.io, 2015.

[119] James Bergstra and Yoshua Bengio. Random search for hyper-parameter optimization. *Journal of Machine Learning Research*, 13(Feb):281–305, 2012.

[120] Louis Archambault, Jean Arsenault, Luc Gingras, A. Sam Beddar, René Roy, and Luc Beaulieu. Plastic scintillation dosimetry: Optimal selection of scintillating fibers and scintillators. *Medical Physics*, 32(7):2271–2278, July 2005.

[121] D L Mason, J J Battista, R B Barnett, and A T Porter. Ytterbium-169: calculated physical properties of a new radiation source for brachytherapy. *Med Phys*, 19(3):695–703, 1992.

[122] D C Medich, M A Tries, and J J Munro III. Monte Carlo characterization of an ytterbium-169 high dose rate brachytherapy source with analysis of statistical uncertainty. *Med Phys*, 33(1):163–72, 2006.

[123] M J Cazeca, D C Medich, and J J Munro III. Monte Carlo characterization of a new Yb-169 high dose rate source for brachytherapy application. *Med Phys*, 37(3):1129–1136, 2010.

[124] B Currier, J J Munro III, and D C Medich. Dosimetric characterization of the GammaClip^{TM} ^{169}Yb low dose rate permanent implant brachytherapy source for the treatment of nonsmall cell lung cancer postwedge resection. *Med Phys*, 40(8):080701, 2013.

[125] R T Flynn, Q E Adams, K M Hopfensperger, X Wu, W Xu, and Y Kim. Efficient ^{169}Yb high-dose-rate brachytherapy source production using reactivation. *Med Phys*, 46:2935–2943, 2019.

[126] C M Callaghan, Q E Adams, R T Flynn, X Wu, W Xu, and Y Kim. Systematic review of intensity-modulated brachytherapy (IMBT): static and dynamic techniques. *Med Phys*, 105(1):206–221, 2019.

[127] G Famulari, M Duclos, and S A Enger. A novel ^{169}Yb-based dynamic-shield intensity modulated brachytherapy delivery system for prostate cancer. *Med Phys*, 47(3):859–868, 2020.

[128] L Beaulieu, A Carlsson Tedgren, J-F Carrier, S D Davis, F Mourtada, M J Rivard, R M Thomson, F Verhaegen, T A Wareing, and J F Williamson. Report of the Task Group 186 on model-based dose calculation methods in brachytherapy beyond the TG-43 formalism: Current status and recommendations for clinical implementation. *Med Phys*, 39(10):6208–6236, 2012.

[129] G Famulari, M Renaud, C M Poole, M D C Evans, J Seuntjens, and S A Enger. RapidBrachyMCTPS: a Monte Carlo-based treatment planning system for brachytherapy applications. *Phys Med Biol*, 63(17):175007, 2018.

[130] S Agostinelli, J Allison, K Amako, J Apostolakis, H Araujo, P Arce, M Asai, D Axen, S Banerjee, and G Barrand. Geant4 - a simulation toolkit. *Nucl Inst and Meth in Phys Research*, 506(3):250–303, 2003.

[131] J Allison, K Amako, J Apostolakis, H Araujo, P Arce Dubois, M Asai, G Barrand, R Capra, S Chauvie, R Chytracek, G A P Cirrone, G Cooperman, G Cosmo, G Cuttone, G G Daquino, M Donszelmann, M Dressel, G Folger, F Foppiano, J Generowicz, V Grichine, S Guatelli, P Gumplinger, A Heikkinen, I Hrivnacova, A Howard, S Incerti, V Ivanchenko, T Johnson, F Jones, T Koi, R Kokoulin, M Kossov, H Kurashige, V Lara, S Larsson, F Lei, O Link, F Longo, M Maire, A Mantero, B Mascialino, I McLaren, P Mendez Lorenzo, K Minamimoto, K Murakami, P Nieminen, L Pandola, S Parlati, L Peralta, J Perl, A Pfeiffer, M G Pia, A Ribon, P Rodrigues, G Russo, S Sadilov, G Santin, T Sasaki, D Smith, N Starkov, S Tanaka, E Tcherniaev, B Tomé, A Trindade, P Truscott, L Urban, M Verderi, A Walkden, J P Wellisch, D C Williams, D Wright, and H Yoshida. Geant4 developments and applications. *IEEE Trans Nucl Sci*, 53(1):270–278, 2006.

[132] J K Tuli. Evaluated nuclear structure data file, a manual for preparation of data sets. Technical report, Lawrence Berkeley National Laboratory, Berkeley, CA, 1987.

[133] D E Cullen, J H Hubbell, and L Kissel. EPDL97: the evaluated photo data library '97 version. Technical report, Lawrence Livermore National Laboratory, Livermore, CA, 1997.

[134] S T Perkins, D E Cullen, and M N Seltzer. Tables and graphs of electron-interaction cross sections derived from the LLNL Evaluated Electron Data Library (EEDL), Z = 1-100. Technical report, Lawrence Livermore National Laboratory, Livermore, CA, 1997.

[135] J F Williamson. Monte Carlo evaluation of kerma at a point for photon transport problems. *Med Phys*, 14:567–576, 1987.

[136] R E P Taylor and D W O Rogers. EGSnrc Monte Carlo calculated dosimetry parameters for ^{192}Ir and ^{169}Yb brachytherapy sources. *Med Phys*, 35(11):4933–4944, 2008.

[137] D Mann-Krzisnik, F Verhaegen, and S A Enger. The influence of tissue composition uncertainty on dose distributions in brachytherapy. *Radiother Oncol*, 126:394–410, 2018.

[138] K R Russell, A Ahnesjö, and Å K Carlsson. Derivation of dosimetry data for brachytherapy sources using Monte Carlo for primary and scatter dose separation. In W Schlegel and T Bortfeld, editors, *The Use of Computers in Radiation Therapy*, pages 495–497. Springer, Berlin, Heidelberg, 2000.

[139] K R Russell, A Ahnesjö, and Å K Carlsson. Brachytherapy source characterization for improved dose calculations using primary and scatter dose separation. *Med Phys*, 32:2739–2752, 2005.

[140] F J Reynoso, J J Munro III, and S H Cho. Technical Note: Monte Carlo calculations of the AAPM TG-43 brachytherapy dosimetry parameters for a new titanium-encapsulated Yb-169 source. *J Appl Clin Med Phys*, 18(4):193–199, 2017.

[141] R K Das, A S Meigooni, V Misha, M A Langton, and J F Williamson. Dosimetric characterstics of the Type 8 ytterbium-169 interstitial brachytherapy source. *J Brachytherapy Int*, 13:219–234, 1997.

[142] E Mainegra, R Capote, and E Lopez. Dose-rate-constants for ^{125}I, ^{103}Pd, ^{192}Ir and ^{169}Yb brachytherapy sources. *Phys Med Biol*, 43:1557–1566, 1998.

[143] A Piermattei, L Azario, G Rossi, A Soriano, G Arcovito, R Ragona, M Galelli, and G Taccini. Dosimetry of ^{169}Yb seed model X1267. *Phys Med Biol*, 40:1317–1330, 1995.

[144] A Ali, B Spencer, M R McEwen, and D W O Rogers. Towards a quantitative, measurement-based estimate of the uncertainty in photon mass attenuation coefficients at radiation therapy energies. *Phys Med Biol*, 60:1641–1645, 2016.

[145] M J Rivard, D Granero, J Perez-Calatayud, and F Ballester. Brachytherapy dosimetry parameters calculated for a ^{131}Cs source. *Med Phys*, 34(2):754–762, 2007.

[146] P Andreo, D T Burns, and F Salvat. On the uncertainties of photon mass energy-absorption coefficients and their ratios for radiation dosimetry. *Phys Med Biol*, 57:2117–2136, 2012.

[147] M J Rivard, D Granero, J Perez-Calatayud, and F Ballester. Influence of photon energy spectra from brachytherapy sources on Monte Carlo simulations of kerma and dose rates in water and air. *Med Phys*, 37(2):869–876, 2005.